SJSU SAN JOSÉ STATE UNIVERSITY
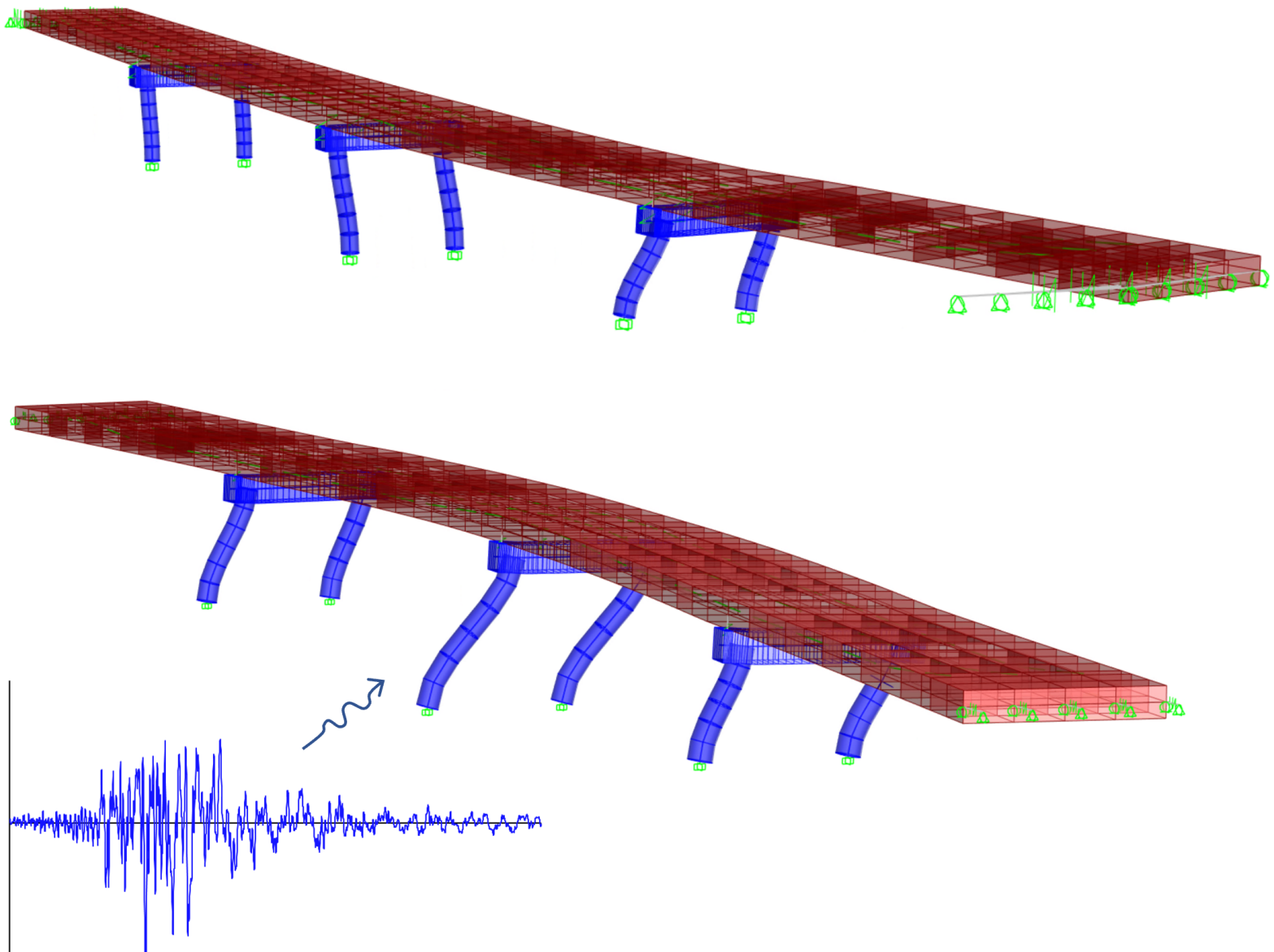
MTI MINETA TRANSPORTATION INSTITUTE

Damage Detection and Damage Localization in Bridges with Low-Density Instrumentations Using the Wave-Method: Application to a Shake-Table Tested Bridge

Mehran Rahmani, Ph.D., P.E.   Xintong Ji, M.S. CE   Sovann Reach Kiet, M.S. CE

CSUTC California State University Transportation Consortium

CALIFORNIA STATE UNIVERSITY LONG BEACH

Mineta Transportation Institute

Founded in 1991, the Mineta Transportation Institute (MTI), an organized research and training unit in partnership with the Lucas College and Graduate School of Business at San José State University (SJSU), increases mobility for all by improving the safety, efficiency, accessibility, and convenience of our nation's transportation system. Through research, education, workforce development, and technology transfer, we help create a connected world. MTI leads the Mineta Consortium for Transportation Mobility (MCTM) funded by the U.S. Department of Transportation and the California State University Transportation Consortium (CSUTC) funded by the State of California through Senate Bill 1. MTI focuses on three primary responsibilities:

Research

MTI conducts multi-disciplinary research focused on surface transportation that contributes to effective decision making. Research areas include: active transportation; planning and policy; security and counterterrorism; sustainable transportation and land use; transit and passenger rail; transportation engineering; transportation finance; transportation technology; and workforce and labor. MTI research publications undergo expert peer review to ensure the quality of the research.

Education and Workforce

To ensure the efficient movement of people and products, we must prepare a new cohort of transportation professionals who are ready to lead a more diverse, inclusive, and equitable transportation industry. To help achieve this, MTI sponsors a suite of workforce development and education opportunities. The Institute supports educational programs offered by the Lucas Graduate School of Business: a Master of Science in Transportation Management, plus graduate certificates that include High-Speed and Intercity Rail Management and Transportation Security Management. These flexible programs offer live online classes so that working transportation professionals can pursue an advanced degree regardless of their location.

Information and Technology Transfer

MTI utilizes a diverse array of dissemination methods and media to ensure research results reach those responsible for managing change. These methods include publication, seminars, workshops, websites, social media, webinars, and other technology transfer mechanisms. Additionally, MTI promotes the availability of completed research to professional organizations and works to integrate the research findings into the graduate education program. MTI's extensive collection of transportation-related publications is integrated into San José State University's world-class Martin Luther King, Jr. Library.

_____

Damage Detection and Damage Localization in Bridges with Low-Density Instrumentations Using the Wave Method: Application to a Shake-Table Tested Bridge

Mehran Rahmani, Ph.D., P.E.

Xintong Ji, M.S. CE

Sovann Reach Kiet, M.S. CE

September 2022

TECHNICAL REPORT DOCUMENTATION PAGE

1. Report No. 22-37	2. Government Accession No.	3. Recipient's Catalog No.		
4. Title and Subtitle Damage Detection and Damage Localization in Bridges with Low-Density Instrumentations Using the Wave-Method: Application to a Shake-Table Tested Bridge		**5. Report Date** September 2022		
		6. Performing Organization Code		
7. Authors Mehran Rahmani, Ph.D., P.E. Xintong Ji, MS. CE Sovann Reach Kiet, MS. CE		**8. Performing Organization Report**		
9. Performing Organization Name and Address Mineta Transportation Institute College of Business San José State University San José, CA 95192-0219		**10. Work Unit No.**		
		11. Contract or Grant No. ZSB12017-SJAUX		
12. Sponsoring Agency Name and Address State of California SB1 2017/2018 Trustees of the California State University Sponsored Programs Administration 401 Golden Shore, 5th Long Beach, CA 90802		**13. Type of Report and Period Covered**		
		14. Sponsoring Agency Code		
15. Supplemental Notes				

16. Abstract

This study presents a major development to the wave method, a methodology used for structural identification and monitoring. The research team tested the method for use in structural damage detection and damage localization in bridges, the latter being a challenging task. The main goal was to assess capability of the improved method by applying it to a shake-table-tested prototype bridge with sparse instrumentation. The bridge was a 4-span reinforced concrete structure comprising two columns at each bent (6 columns total) and a flat slab. It was tested to failure using seven biaxial excitations at its base. Availability of a robust and verified method, which can work with sparse recording stations, can be valuable for detecting damage in bridges soon after an earthquake. The proposed method in this study includes estimating the shear (c_S) and the longitudinal (c_L) wave velocities by fitting an equivalent uniform Timoshenko beam model in impulse response functions of the recorded acceleration response. The identification algorithm is enhanced by adding the model's damping ratio to the unknown parameters, as well as performing the identification for a range of initial values to avoid early convergence to a local minimum. Finally, the research team detect damage in the bridge columns by monitoring trends in the identified shear wave velocities from one damaging event to another. A comprehensive comparison between the reductions in shear wave velocities and the actual observed damages in the bridge columns is presented. The results revealed that the reduction of c_S is generally consistent with the observed distribution and severity of damage during each biaxial motion. At bents 1 and 3, c_S is consistently reduced with the progression of damage. The trends correctly detected the onset of damage at bent 1 during biaxial 3, and damage in bent 3 during biaxial 4. The most significant reduction was caused by the last two biaxial motions in bents 1 and 3, also consistent with the surveyed damage. In bent 2 (middle bent), the reduction trend in c_S was relatively minor, correctly showing minor damage at this bent. Based on these findings, the team concluded that the enhanced wave method presented in this study was capable of detecting damage in the bridge and identifying the location of the most severe damage. The proposed methodology is a fast and inexpensive tool for real-time or near real-time damage detection and localization in similar bridges, especially those with sparsely deployed accelerometers.

17. Key Words Structural Health Monitoring, Bridge, Accelerometer, Earthquakes, Damage	**18. Distribution Statement** No restrictions. This document is available to the public through The National Technical Information Service, Springfield, VA 22161.		
19. Security Classif. (of this report) Unclassified	**20. Security Classif. (of this page)** Unclassified	**21. No. of Pages** 122	**22. Price**

Form DOT F 1700.7 (8-72)

ACKNOWLEDGMENTS

CONTENTS

LIST OF FIGURES

LIST OF TABLES

Executive Summary

This study presents a major development to the wave method and its use in structural damage detection and damage localization in bridges. The main goal was to assess the method's ability to detect the extent and location of damage soon after a destructive event (e.g., an earthquake). Detecting damage in a bridge structure is a challenging task, especially for those structures with a limited number of deployed accelerometers. It is further challenging to find the location of damage in a bridge with sparse instrumentation and with a recorded response that has a short frequency bandwidth (e.g., 0–10 Hz). In the past three decades, researchers have proposed several methodologies to address these challenges. However, there has not been a method that is fast (i.e., computationally inexpensive) and robust in detecting and localizing damage in full-scale bridges with a limited number of sensors. Specifically, localizing damage is a major challenge. The wave method was shown to be robust when applied to real structures and large amplitude responses in buildings. In a companion study, its first application to bridges used a shear beam model, which showed that the method is viable for damage detection in bridges. However, the shear beam model was shown to be too simple for localizing damage (i.e., locating columns with maximum degradation), which would require a more sophisticated beam model as well as improvements to the method's identification algorithm. In this study, we used a uniform Timoshenko beam (TB) model for our identification. One main advantage of the TB compared to the shear beam is its ability to account for column flexural deformation. This is particularly important because the bending motion can cause significant wave dispersion (i.e., waves travel with different speeds at different frequencies) which is not captured by a shear beam model. The identification process in this study includes estimating the shear (c_S) and the longitudinal (c_L) wave velocities by fitting an equivalent uniform TB model in the impulse response functions of the recorded acceleration response. The identification algorithm using the TB model is enhanced by adding the model's damping ratio to the list of unknown parameters (i.e., three unknows in total). We further improved our algorithm by performing the identification for a range of initial values to avoid early convergence to a local minimum. Finally, damage was detected by monitoring changes in the identified wave velocities from one damaging event to another. This was performed using accelerometers at different segments of the bridge helping to localize major damage.

In this study, the acceleration responses from a shake-table-tested bridge were used to assess the capability of the method. The bridge was a 4-span reinforced concrete structure comprising two columns at each bent (6 columns total) and a post-tensioned flat slab deck. The case-study bridge was tested using seven biaxial excitations which progressively damaged the bridge to failure. A summary of damage observed at the actual bridge was collected after each shaking intensity, which helped in our assessment of the wave method. Bridge responses can be complex given their multidirectional movement and the presence of coupled translation-torsional modes of vibration. To better understand the dynamic characteristics of the bridge, we created an auxiliary nonlinear finite element model (FEM) for the tested bridge for further analysis. We used our wave method to perform damage detection for this updated FEM with known behavior.

A comprehensive comparison between the reductions in shear wave velocities and the actual observed damages (i.e., via visual inspection) in the case-study bridge's columns is presented. The results reveal that the reduction of c_S is generally consistent with the observed distribution and severity of damage during each biaxial motion. At bent 1 and bent 3, c_S is consistently reduced with the progression of damage. The trend in reduction of c_S correctly detects the onset of damage at bent 1 during biaxial 3, while the trend shows the onset of damage in bent 3 during biaxial 4, both consistent with surveyed damage in the tested bridge. The most significant reduction was caused by the last two biaxial motions in bents 1 and 3, also consistent with the surveyed damage. In bent 2 (middle bent), the reduction trend in c_S was relatively minor, correctly showing minor damage at this bent.

We conclude that the enhanced wave method presented in this study was capable of detecting the progression of damage in the tested bridge and identifying the location of the most severe damage. The proposed methodology is a fast and inexpensive tool for real-time or near-real-time damage detection and localization in similar types of bridges, especially those with only a few accelerometers deployed on the deck and foundation level. Such instrumentation layouts are common for bridges and overpasses instrumented by the California Geological Survey (CGS); therefore, the proposed method could be used as a supplementary damage indicator for emergency responders and bridge inspectors in the state of California.

1. Introduction

1.1 Problem Statement

Public infrastructure in the U.S. is aged, and the need for monitoring and maintenance has increased recently. Among these critical infrastructure elements are bridges and overpasses, which may fail due to fatigue caused by service loads or due to excessive loads induced by natural or human-caused events, such as earthquakes. Frequent monitoring and condition assessments of bridges are required to ensure their health and to identify repair needs. Given the large number of existing bridges and overpasses in the state of California, conventional visual inspection of all bridges affected by a moderate or large amplitude earthquake can take several weeks. Moreover, some damage spots or element failures may not be visible to inspectors. Alternatively, monitoring the integrity of a structure (e.g., a bridge) using sensory data and detecting structural damage during or soon after an earthquake or another human-caused event may significantly reduce injuries and loss of life caused by the potential collapse of a weakened structure during shaking from aftershocks or from service loads (e.g., traffic loads). Such a monitoring approach for bridges and overpasses could facilitate emergency response in large cities by providing early warnings for unsafe routes soon after an event. Likewise, it would help prevent or reduce monetary loss by avoiding unnecessary closures of safe bridges, helping build smarter and more resilient cities.

Figure 1.1 shows the main elements of a structural health monitoring (SHM) system, which consists of an array of sensors and data acquisition, data processing, and decision-making tools. This study aims to develop an algorithm that converts the recorded response from a low-density recording sensor array (e.g., horizontal acceleration of bridge deck from a few widely spaced accelerometers) to useful information on the extent of damage to a bridge's piers and the location of the most severe damage.

Ever-growing sensing technologies and hardware components (e.g., smaller sensors, cheaper devices, more sensitive instruments, broadband wireless data transfer, etc.) provide unique opportunities to stakeholders and researchers to monitor infrastructure elements during and immediately after a destructive event. Some commercial applications of the sensory data include a dense array of instrumentation that can monitor almost every component of a bridge when placed at numerous locations. Such approaches are expensive due to the number of deployed sensors. In addition, significant volumes of data generated by these dense instrumentation schemes require additional costs for post-processing data as well as for the maintenance of the sensors. Therefore, relatively few bridges in California are densely instrumented. Typical bridge instrumentation schemes in the state rely on low-density arrays. For example, the California Geological Survey (CGS) has instrumented more than 80 highway bridges. These sensors include only a few accelerometers that are sparsely placed on the bridge deck. While these instruments have recorded valuable strong motions in the past decades, the use of recorded data is limited due to the lack of a tested methodology which is robust and applicable to low-density arrays on instrumented full-scale bridges subject to earthquake shakings. Hence, the need for developing a bridge health

monitoring methodology for such set-ups and calibrating it using real data is growing. The proposed method in this study could potentially utilize data from currently instrumented bridges by CGS and provide supplementary damage information for emergency responders and bridge inspectors in California.
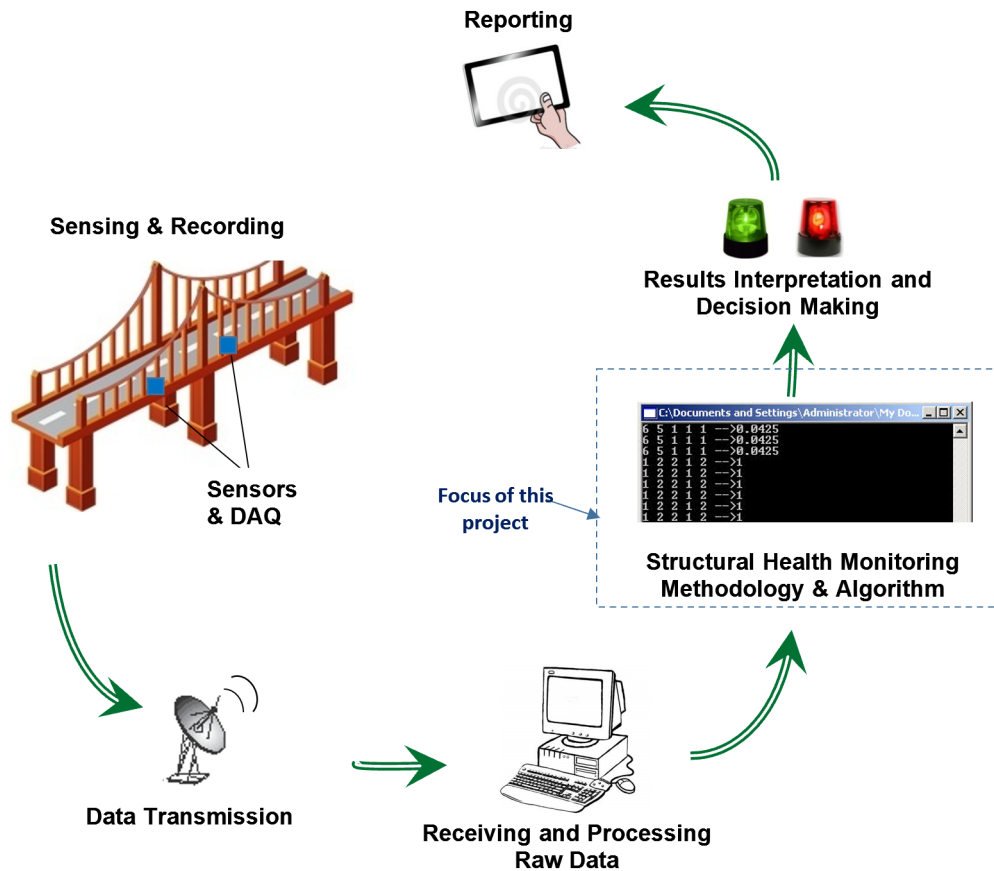
Source: Drawn by Mehran Rahmani, author.

Figure 1.1. Main Elements of Structural Health Monitoring (SHM) for Bridges

In the past five decades, researchers around the globe have developed several methodologies for identifying and detecting damage in small laboratory-scale or full-scale bridges using sensory data. Their focus was to improve the accuracy and practicality of data-based structural health monitoring (SHM) techniques as well as reducing analysis time. Most of the proposed SHM methods require an array of sensors to collect real-time or post-event data, as shown in Figure 1.1. Here, we briefly review some of the methods and work presented by researchers on this topic. Seo et al. (2015) summarized past work on damage detection, bridge capacities evaluation, and remaining life estimation. They concluded that a vibration- and strain-based SHM system could efficiently capture change in dynamic characteristics over time. These two SHM systems have been part of several methodologies developed for bridge damage detection in the past four decades.

Ntotsios et al. (2008) applied vibration-based SHM on the full-scale Polymylos bridge (Greece) and a small-scale laboratory bridge section made of steel. They used a modal identification algorithm and graphical user interface (GUI) to compare the difference in dynamic structural parameters (i.e., mode shapes and modal frequencies) before and after damage and to identify the damage quantity. They compared the value of elemental stiffness and measured reductions to detect damaged locations. Their results were presented for two damaged cases where they found that the accuracy of the method for detecting minor damage was not good. It is noteworthy that the modal frequencies of vibration are global characteristics of a structure by which localizing damage in the structure is not feasible.

Another vibration-based damage detection (VBDD) method was introduced by Zhou et al. (2007). The method used the change in mode shape curvature, a uniform flexibility curvature, and the change in a structure's flexibility. The authors evaluated their method's ability to detect and localize damage using five variants of their methods. Their results showed that accuracy is highly dependent on the number of sensors and their location, with a low-density sensor array resulting in poor damage detection.

In summary, vibration-based SHM methodologies have been based on choosing a set of critical structural characteristics parameters and then comparing their changes before and after damage is induced. Soyoz et al. (2009) introduced a parameter identification study applied to a three-bent concrete bridge model tested on a large-scale shake table. One set of structural parameters was generated based on nonlinear time history analysis by Monte Carlo simulation. In a second round of analysis, the structural parameters were updated in the Bayesian sense to estimate the reliability of the bridge's elements after a large shaking. Results showed that the residual reliability estimated for the damaged elements were smaller for the Bayesian-updated model compared with the non-updated one.

Based on a case study on the Luiz I bridge (Portugal), Costa et al. (2014) pointed out that the modal analysis method of SHM can evaluate the efficacy of a completed rehabilitation on the bridge by comparing the data from before and after a retrofit. The primary structural dynamic parameters they chose were mode shape, natural frequencies, and lateral stiffness. Hsieh et al. (2008) used, as their SHM approach, frequency response functions combined with ERA-OKID for modal parameter identification to optimize the stiffness matrix. They applied this method to a six-span highway bridge tested with varying excitations. The result showed that this SHM method is effective at detecting damage. Another study used experimental modal analysis to analyze damage conditions by testing a three-span steel-stringer bridge (Catbas and Aktan, 2000). The study concluded that useful information about the structure's condition can be obtained from an appropriately designed dynamic test.

Iranmanesh and Ansari (2014) proposed a damage assessment methodology based on energy dissipation and applied this approach to a reinforced concrete bridge column. The methodology aimed to quantify minor to moderate damage from seismic shaking that is difficult to visually

inspect. The experiment used a hybrid simulations program to analyze a scaled two-span reinforced concrete bridge with circular cross-sectional columns. By integrating the height of plastic hinge and average curvature, they could obtain energy dissipation in the column. Further, the structural damage level was computed by a dissipated energy index. They concluded that using their SHM method, the minor and moderate damage that is barely visible can be detected and quantified.

Some research has combined more than one method to improve the accuracy of the SHM system. In one of these studies, researchers combined statistical pattern recognition with vibration-based methods (Noman et al., 2013). Statistical pattern recognition is more tolerant of noisy data and environmental effects. Additionally, researchers have integrated non-destructive tests with a probabilistic framework to monitor bridge health conditions (Huang et al., 2011).

Regardless of what method is being used for structural health monitoring, an essential part of SHM is data collection from instruments and post-processing. Real-time, comprehensive, and sensitive data collection processes can improve the accuracy and calibration of any SHM methodology. Sensors are used for gathering information such as displacement or acceleration at different locations of a bridge. For example, to monitor seismic response on the Bill Emerson Memorial Bridge (located on the border of Missouri and Illinois, U.S.), a total of 84 channels of accelerometers formed a network on the bridge deck, pier foundations, surface, and downhole free-field arrays (Celebi, 2006). In addition to accelerometers, monitoring hardware, a data concentrator, and mass storage devices were also installed on the bridge. All of these sensors and devices formed a complete data collection system that is an essential part of any SHM system (Celebi, 2006). An effective SHM algorithm will help utilize these data and produce a robust result that accurately detects damage.

1.2 Project Objectives

This study's main goal is to assess the capability of the wave method for monitoring the structural integrity of bridges and detecting the extent of damage incurred soon after a destructive event (e.g., an earthquake). We also aim to localize damage in a bridge structure using the proposed method. While successful proof of concept study applications in buildings were presented by the authors, this study further evaluates the method's performance on a case-study bridge with a low-density sensor array. We identify challenges and enhance the method to be used as a robust damage assessment technique for bridges subjected to natural or human-caused disasters. Developing the proposed SHM algorithm for bridge structures will provide the opportunity for further development of a seismic alert system as well as for general condition monitoring in bridges.

The author, in collaboration with former research colleagues at the University of Southern California, has been developing the wave method for buildings over the past 15 years (Trifunac et al., 2003; Todorovska and Trifunac, 2008a, 2008b; Todorovska and Rahmani, 2012; Rahmani and Todorovska, 2014, 2015; Ebrahimian and Todorovska, 2014, 2015; Rahmani et al., 2015). This project's main objective is to further develop the wave method for use in damage detection and

damage localization on highway bridges with low-density sensor arrays. The capability of the method for bridge SHM is investigated using sensory data from a 4-span shake-table-tested reinforced concrete bridge. The case study was tested to failure at the University of Nevada, Reno (UNR) in 2007 (Nelson et al., 2007). Figure 1.2 shows a picture of the bridge. In the wave method, the bents of the bridge were modeled using a uniform Timoshenko beam (TB), where our damage-sensitive parameter is the shear wave velocity of the equivalent TB model. In the methodology section of this report, we discuss the wave method and the identification algorithm. Major milestones in the development of the method are described in the following sections.

Source: Nelson et al. (2007)

Figure 1.2. The 4-Span Prototype Reinforced Concrete Bridge

1.3 Wave Methods for Structural Health Monitoring

The seismic response of structures can alternatively be viewed as a wave propagation problem. The wave method used in this study aims to identify the velocity of propagating waves in the structure and use it as an indicator for structural health monitoring. The method has gained increasing interest in the past two decades owing to its advantages. Its simplicity (i.e., no need for detailed modeling of the structure) as well as its applicability to large amplitude data in mid- and high-rise buildings were presented in several extant studies (e.g., Todorovska and Trifunac, 2008a, 2008b; Todorovska and Rahmani, 2012; Rahmani and Todorovska, 2014, 2015; Ebrahimian and Todorovska, 2014, 2015). The method also showed much less sensitivity to the properties of the underlying soil and its variations (Todorovska, 2009). The changes in velocities of propagating waves through the structure, which depend on the structural stiffness, can be utilized to estimate the extent of damage and possibly its location. For the same case study bridge, Rahmani and

Naik (2020) first used the wave method to investigate the possibility of detecting damage in the structure. They utilized a uniform shear beam model, fitted in the actual response of the bridge, for their identification algorithm, by which the velocities of vertically propagating waves in each bent of the bridge were identified. The damage is detected through the change of velocities of waves spreading between two sensors located at the shake table and at the deck level. The results showed that the method was able to detect overall stiffness reduction in the structure, consistent with the change in the fundamental mode of vibration. However, Rahmani and Naik (2020) found that the observed trends in c_s did not provide a clear indication of the location of damage. This shortfall was attributed to (1) the complex response of the bridge, including various pure and coupled modes of vibrations (i.e., translational, torsional, and longitudinal modes); and (2) the use of an overly simple shear beam model which does not account for a columns' bending as well as the dispersive (i.e., frequency-dependent) nature of wave propagation in bridges.

In this study, we address the challenge associated with the complexity of the bridge's response by creating a detailed finite element model (FEM) of the bridge to better understand the modal frequencies and shapes of the bridge over the frequency band of interest (i.e., 0–10 Hz herein). The challenge of the shear beam model's simplicity was addressed by significantly improving our identification algorithm in which a Timoshenko beam (TB) model was utilized as described in the methodology section. The wave method was applied to the FEM response and actual recorded data for a comparison and assessment of our results.

This report is organized as follows. Section 2 introduces the wave method used in this project, which includes the use of waveform inversion algorithm and the Timoshenko beam model. Also, it presents the tested bridge's structural system. Section 3 focuses on the bridge's nonlinear finite element model (FEM) and its behavior during excitations at seven shaking intensities. Section 4 concentrates on wave method identification of the actual tested bridge as well as its FEM. It provides details on fitting the uniform Timoshenko beam model to actual bridge data and FEM data to identify the change of velocities during the seven shakings. The section includes a discussion of the obtained results. Section 5 summarizes our findings and provides conclusions on the strengths and limitations of the wave method for detecting damage in similar bridge structures.

2. Methodology

The wave method for structural system identification is a powerful method that has been further developed by the authors and others in the past two decades (Todorovska and Rahmani, 2012; Ebrahimian and Todorovska, 2014). Its application for structural health monitoring and damage detection in buildings has proven its robustness and benefits compared to other available methods (Todorovska, 2009). This section provides a summary of the method along with the authors' important improvements to its accuracy. In addition, we briefly describe the case study bridge and the data used for the project's analysis.

2.1 Wave Method and Waveform Inversion

In this project, the bridge is divided into three segments, each encompassing a pair of columns (i.e., one bent) as shown in Figure 2.1. We consider each segment of the bridge a *waveguide* through which seismic waves propagate from the shake table to the bridge deck. Each bent (i.e., waveguide), separately, is modeled as a uniform elastic Timoshenko beam (TB), which accounts for both shear and bending deformation in the columns. The TB is characterized by its height (H), length (L), and width (W); L and W are further used to calculate the layer's rotary inertia (I), shear modulus (G), and Young's modulus (E). E and G are related to *longitudinal* (c_L) and *shear* (c_S) wave velocities; the properties of the beam's material are given as $c_L = \sqrt{E/\rho}$ and $c_S = \sqrt{G/\rho}$. Figure 2.2 shows details of the uniform TB model used in this study. The model transfer functions (TFs) and impulse response functions (IRFs) at the deck level and the shake-table level were computed using the propagator matrix approach, as described in Ebrahimian and Todorovska (2014). Furthermore, the observed TFs and IRFs were computed from the recorded acceleration response at the bridge.
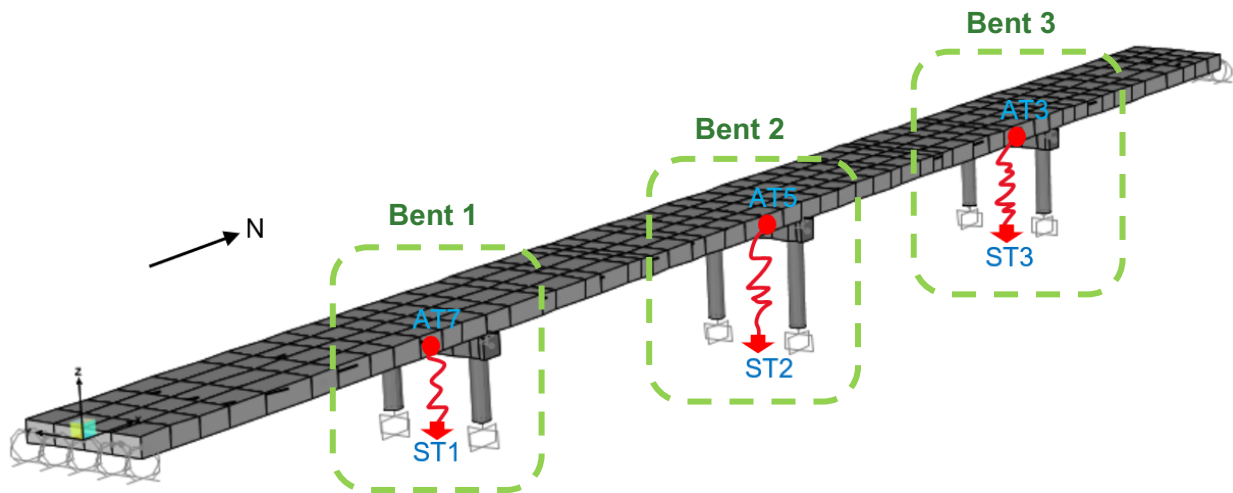
Figure 2.1. A Rendering of the Case-Study Bridge and its Three Segments (i.e., Bents) Used for Damage Identification

The *waveform inversion algorithm* (Rahmani and Todorovska, 2013) fits the model IRFs into the observed ones in the least-square sense. Figure 2.3 illustrates the fitted IRFs and the consequent TFs' agreement for a seven-story building that was modeled by a 4-layer TB (Rahmani et al, 2021). The IRFs are low-pass filtered before fitting, and a careful choice of the cut-off frequency, f_{max}, is very important because the cut-off frequency affects the width of the source pulse (at the roof) and consequently the shape of the causal and acausal propagating pulses in the IRFs. Also, it determines the number of modes included in our calculation. We chose to use f_{max}=10 Hz, such that the passband includes two transverse modes of vibration and at least one longitudinal and one torsional mode. Given our one-layer TB model, the fit is performed at one level only (the receiving station) since the IRFs are identical at the source, as shown in Figure 2.3 (i.e., at the source, the pulse is an inverse Fourier transform of a low-pass filtered boxcar function).

The method identifies the longitudinal (c_L) and shear (c_S) wave velocities of the TB model. The moduli ratio $R = G/E = c_s^2/c_L^2$, the ratio of shear to bending stiffness, indicates the nature of the beam. A very small value of R (e.g., less than 0.1) indicates a structure that is very stiff in flexure and deforms predominantly in shear. Therefore, in such structures, trends in c_S are more meaningfully related to the lateral stiffness and, consequently, will be considered as a damage-sensitive parameter (Rahmani and Todorovska, 2021).

The damping value assumed for the TB model is another important parameter: it can affect the causal and acausal pulse amplitude in the IRFs and, subsequently, the goodness of the fits. In addition, damping is expected to increase in a damaged structure relative to its undamaged state, making a reasonable choice of damping at each damage state important. In this project, the TB model's damping was accounted for by the Kelvin-Voigt damping approach, in which the Young's and shear moduli are converted to complex values as $E \leftarrow E(1-i\omega\mu)$ and $G \leftarrow G(1-i\omega\mu)$, where ω is the circular frequency. The damping parameter, μ, is the viscosity constant in units (seconds), and it is different from dimensionless viscous damping ratio, ζ, where approximately $\zeta \approx \omega\mu/2$ (Rahmani and Todorovska, 2021). In the present study, μ is assumed to be constant across the 0–10-Hz band, and optimal viscous constants, μ, were estimated by trials such that the selected damping results in the best match between the model and the observed IRFs. The trials were performed for each damage state separately.

We identified the shear (c_S) and longitudinal (c_L) wave velocities in the bridge using our fitted uniform TB model, which led to an estimation of two unknowns for each bent (i.e., segment) of the bridge. A waveform inversion algorithm was used to fit the best TB model into the recorded response at the tested bridge. The waveform inversion algorithm was originally proposed for fitting a layered shear beam model by Rahmani and Todorovska (2012). The algorithm was further developed to fit a Timoshenko beam (TB) model by Ebrahimian and Todorovska (2014). A brief review of the process is discussed here.

Figure 2.2 presents our analytical Timoshenko beam (TB) model. Fig. 2.2a shows a viscoelastic cantilever TB, while Fig. 2.2b shows a deformed element, where θ is rotation due to bending,

$\gamma(z;t)$ is additional rotation due to shear caused by uniform shear stress on the section, and $u(z,t)$ is horizontal displacement. Figure 2.2c shows a free-body diagram of a beam element, in which M and V are the internal bending moment and shear force, respectively. Computation of two key elements of the inversion, response transfer functions (TFs) and impulse response functions (IRFs), are described as follows:

The system function of a linear system, in the time domain, is the impulse response function $h(z, z_{ref};t)$ (IRF), which is the inverse Fourier transform of the system transfer function $\hat{h}(z, z_{ref};\omega)$ (TF), both defined by the transform pair

$$\hat{h}(z, z_{ref};\omega) = \frac{\hat{u}(z;\omega)}{\hat{u}(z_{ref};\omega)} \quad \Leftrightarrow \quad h(z, z_{ref};t) = FT^{-1}\left\{\hat{h}(z, z_{ref};\omega)\right\} \tag{1}$$

in which z is the coordinates of a level in the structure and z_{ref} is the coordinate of a reference point on the structure; ω is circular frequency, $\hat{u}(z;\omega)$ and $\hat{u}(z_{ref};\omega)$ are the Fourier transforms of the motion at z and z_{ref}, and $FT^{-1}\{\cdot\}$ denotes an inverse Fourier transform. Physically, $\hat{h}(z,z_{ref};\omega)$ represents the motion at z when the motion at z_{ref} is $e^{i\omega t}$, and $h(z,z_{ref};t)$ is the motion at z when the motion at z_{ref} is the Dirac delta function, the low-pass version of which is the sinc function. Hence, the motion at z_{ref} can be viewed as a virtual source pulse. Then, $\hat{h}(z,z_{ref};\omega)$ and $h(z,z_{ref};t)$ describe the relationship between the motions at z and z_{ref}. The TF can be computed as

$$\hat{h}(z, z_{ref};\omega) \approx \frac{\hat{u}(z;\omega)\overline{\hat{u}}(z_{ref};\omega)}{|\hat{u}(z_{ref};\omega)|^2 + \varepsilon} \tag{2}$$

in which ε is a regularization parameter and the bar indicates a complex conjugate (Snieder and Şafak, 2006). If the physical source of the structure's excitation is at z_{ref}, then at different coordinates z, the IRFs $h(z, z_{ref};t)$ will reveal the propagation of the virtual source pulse through the structure. Figure 2.3 illustrates the IRF and TF for the recorded ambient vibration response and our fitted TB in a seven-story building.
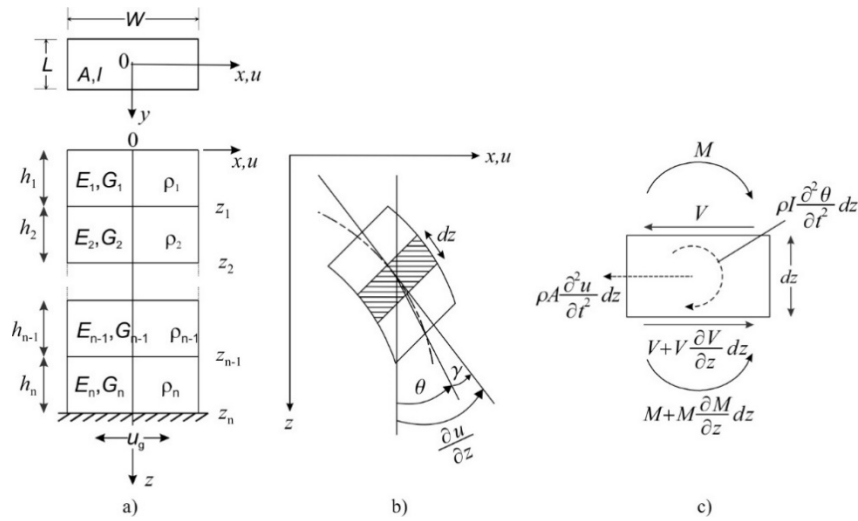
Source: Redrawn from Ebrahimian and Todorovska (2015)

Figure 2.2. (a) Cantilevered Layered Timoshenko Beam Model; (b) Deflected Element; (c) Free-Body Diagram of Element

The objective function for the least squares fit is defined as

$$S(c_L, c_S; \mu) = \left\| h_s^{obs} - h_s^{mod}(c_L, c_S; \mu) \right\|_{L_2}^2 \tag{3}$$

in which c_L and c_S are the unknown longitudinal and shear wave velocities of the beam, respectively. Then, the best value of the pair (c_L, c_S) is chosen by minimizing the L_2 norm of the objective function. Equation (3) defines a nonlinear estimation problem, which we solve by the trust-region algorithm, a popular and powerful optimization method available in several MATLAB toolboxes. A benefit of the algorithm is the opportunity for users to define a lower and an upper bound for the unknown parameters, making the search for the unknown parameters more efficient and relatively quick. The algorithm initiates its search from a spherical neighborhood of the initial values (trusted region) and works by either shrinking the trusted region or relocating it. Figure 2.3a shows the goodness of IRFs' fit because they are fitted over a specified interval, while TF agreement is plotted as a check and indicates if the TB model is appropriate for this structure.

Similar to several other algorithms, the trust-region algorithm is susceptible to convergence to a local minimum, depending on the values chosen as initial conditions. We enhanced the inversion algorithm by performing the identification over a wide range of initial values $((c_S)_{ini}$ and $(c_L)_{ini})$, revealing the number of local minima for each damage state and the variability in the identification results across the local minima and the global minimum. A higher variability in identification results for a specific damage state indicates a higher sensitivity to the initial conditions, and thus, a higher uncertainty in the identified value. This increases the likelihood of a false damage alert.

Bridge structures' structural response is complex when compared to those of other buildings. Over a range of passband frequency (e.g., 0–20 Hz), bridge response can include several modes of vibration such as longitudinal, transverse, vertical, torsional, and some coupled modes. A unique excitation at each support could add further complexity. For this study, we created a nonlinear finite element model (FEM) for the case-study bridge, updating the FEM based on undamaged and damaged structure recorded response. The FEM is useful to help us understand the bridge's vibrational response and carefully identify the frequency passband for this study. Chosen frequency band includes the first translational vibration mode and excludes coupled torsional-translational modes. For the updated FEM, we also performed wave-based identification on acceleration data from the FEM, comparing the results with those from recorded data in the tested bridge.

Localizing bridge damage with a few sensors on deck is challenging, yet this was the main objective. To do this, structural identification and damage detection was performed for each bridge bent separately using transverse acceleration recorded at the top of each bent or in proximity. Acceleration at the excitation source (i.e., foundation level) will be needed, ideally at each bent. Figure 2.1 shows the case study bridge and three pairs of accelerometers used to identify each bent. This approach identifies the wave velocities of an equivalent medium propagating between two sensors located at the shake table and deck level. We first analyzed the trends in the identified velocities and detect damage in each bent. Then, we compared the results across the three bents to identify: (1) the onset of first damage and its location, (2) the location of the most severe damage, and (3) the location of the second most damaged bent.
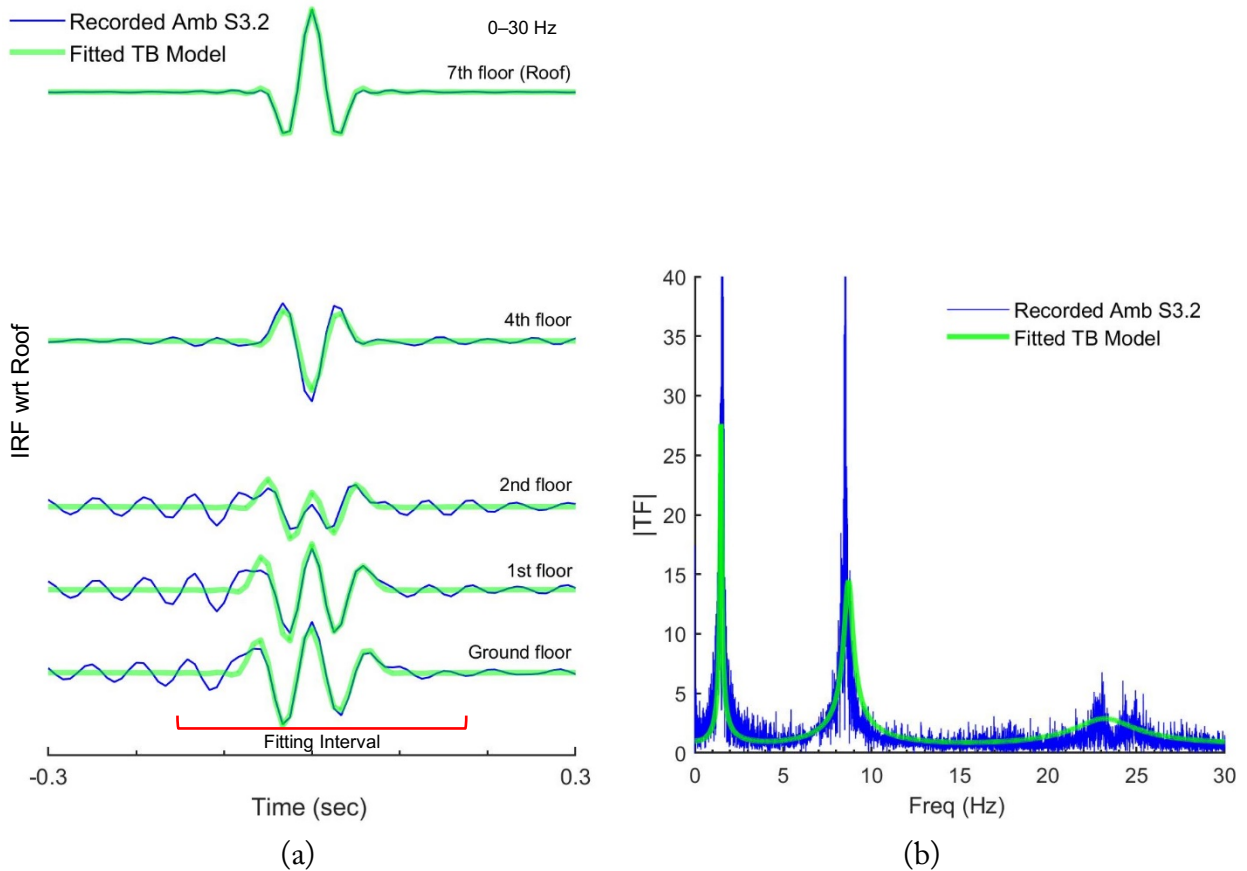
Figure 2.3 (a) Impulse Response Function for Recorded Ambient Vibration Data (Damage State S3.2) and Its Best Fitted Layered TB Model, and (b) Their Corresponding Transfer Function

2.2 A Note on the Effect of Damping, c_L, and Moduli Ratio R on IRFs' Shape in the TB Model

In this section, we briefly illustrate the extent of change in the amplitudes and time-shifts of causal and acausal pulses in the TB model's IRFs. We analyze a TB with varying values for a damping constant, c_L, and $R = c_S^2 / c_L^2$, and present the IRFs' plots for all values, which will also show IRFs' sensitivity and our fitted TB results to each of the unknown parameters noted above. In each set of trials, we kept one parameter constant and varied the other two. The TB model has the dimensions and density similar to the one used to model each bent of the bridge (see Figure 2.1).

Values of c_L varied from 15 to 35 m/s by a 5 m/s step, and values of R varied from 0.01 to 5 by a 0.05 step. Note that a small R value (say, less than 0.30) indicates a predominantly shear motion in the TB, and a large R value (say, larger than 1.20) indicates a mostly flexural deformation in the

TB. The results were compared for two separate TB damping values of 0.01 sec and 0.05 sec. Figures 2.4 to 2.6 are 2D plots of the IRFs for varying c_L and constant R for a damping value of 0.05. The graphs show that when the c_L value increases, the IRF plots shift toward positive time, and pulse amplitudes decrease. When c_L values are too small, the *R-value* and damping ratio significantly impact the IRF's pulse shifts and amplitudes. This is exacerbated for *R-value*s smaller than one. When c_L values become larger, the shifts in pulses are almost zero.

Figures 2.7 to 2.9 show IRF plots for 0.05 sec damping, a constant cL, and varying *R-value*s. Similarly, the IRF plots shift to the positive time direction when the R value increases and the amplitude of IRF plots decreases. When the *R-value* is smaller than one (i.e., shear deformation is pronounced), these changes are larger. Figure 2.10 shows the pattern of pulse shifts in IRFs for various cL and *R-values* and for both damping values. In comparison, 0.05 sec damping has shown less pulse shifts in the IRF plots relative to 0.01 sec damping. Comparing results for 0.01 sec and 0.05 sec damping reveals that the pulse amplitudes of IRFs are lager for the 0.05 sec damping. When R and c_L are constant, a higher damping value (0.05 sec) causes a larger shift in the pulses compared with the lower (0.01 sec) damping. Our waveform inversion, utilizing a nonlinear least-square algorithm, aims to find the optimal values for these three unknowns such that the IRFs of the TB model fits best the IRFs calculated from the observed response.
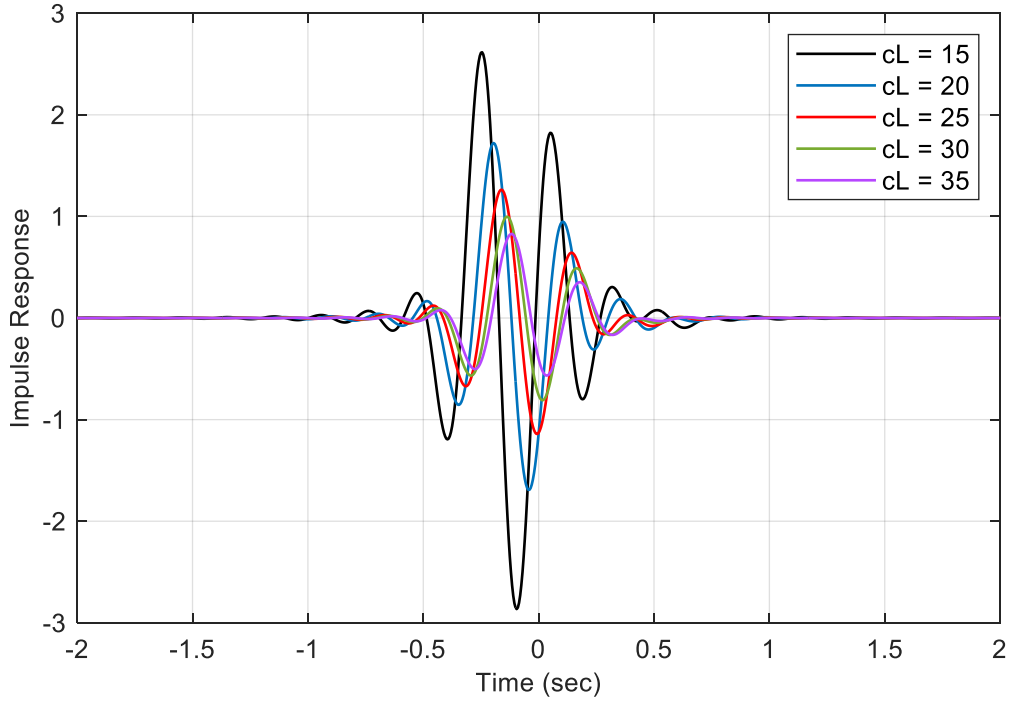
Figure 2.4. IRF Plots of a TB Model with 5% Damping, $R = 0.2$ and Varying c_L
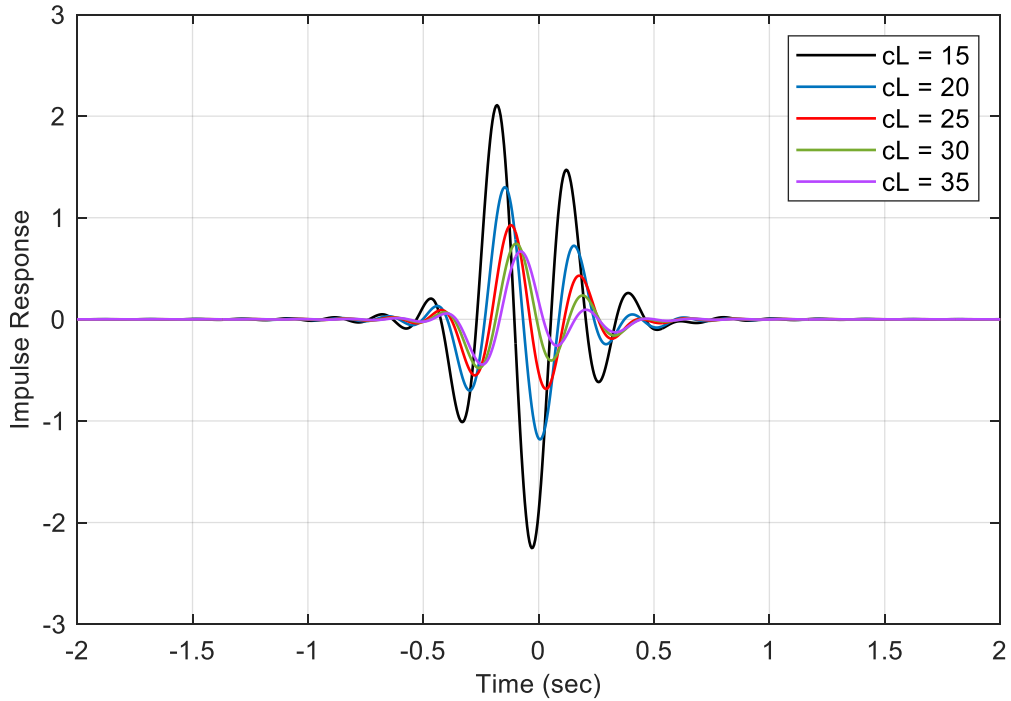
Figure 2.5. IRF Plots of a TB Model with 5% Damping, $R = 0.5$ and Varying c_L
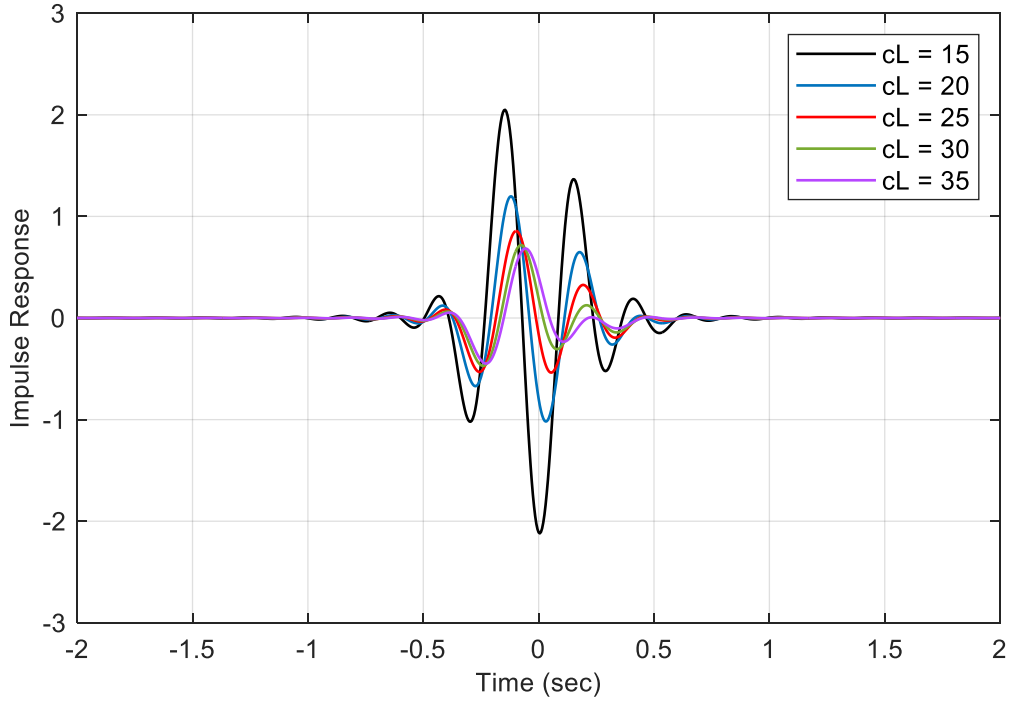
Figure 2.6. IRF Plots of a TB Model with 5% Damping, $R = 1$ and Varying c_L
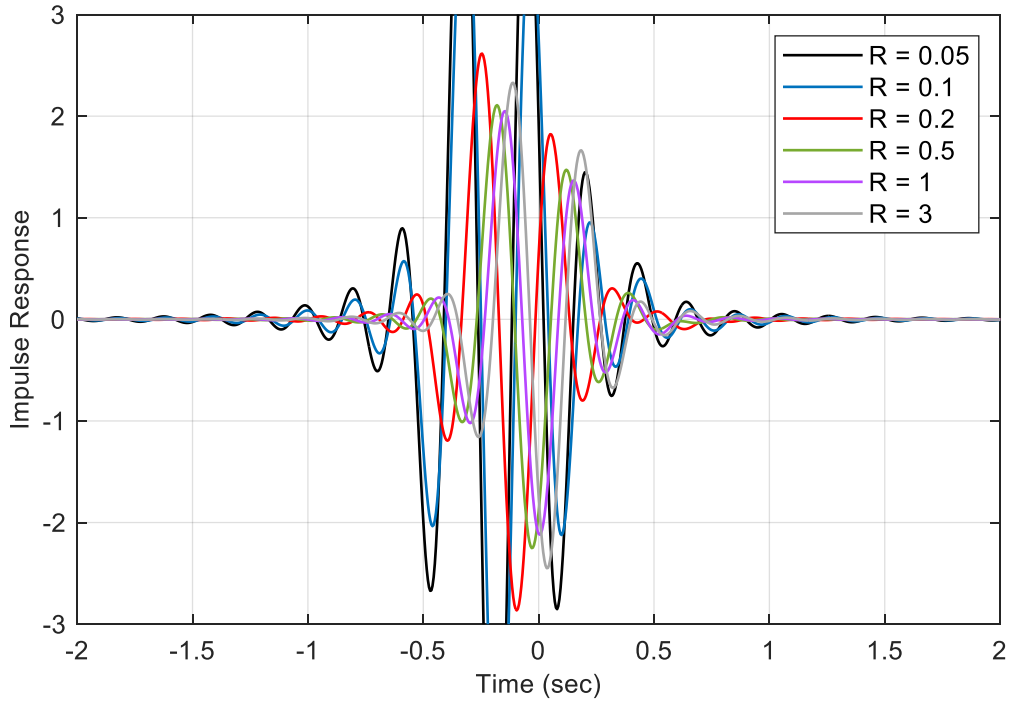
Figure 2.7. IRF Plots of a TB Model with 5% Damping, $c_L = 15$ and Varying R
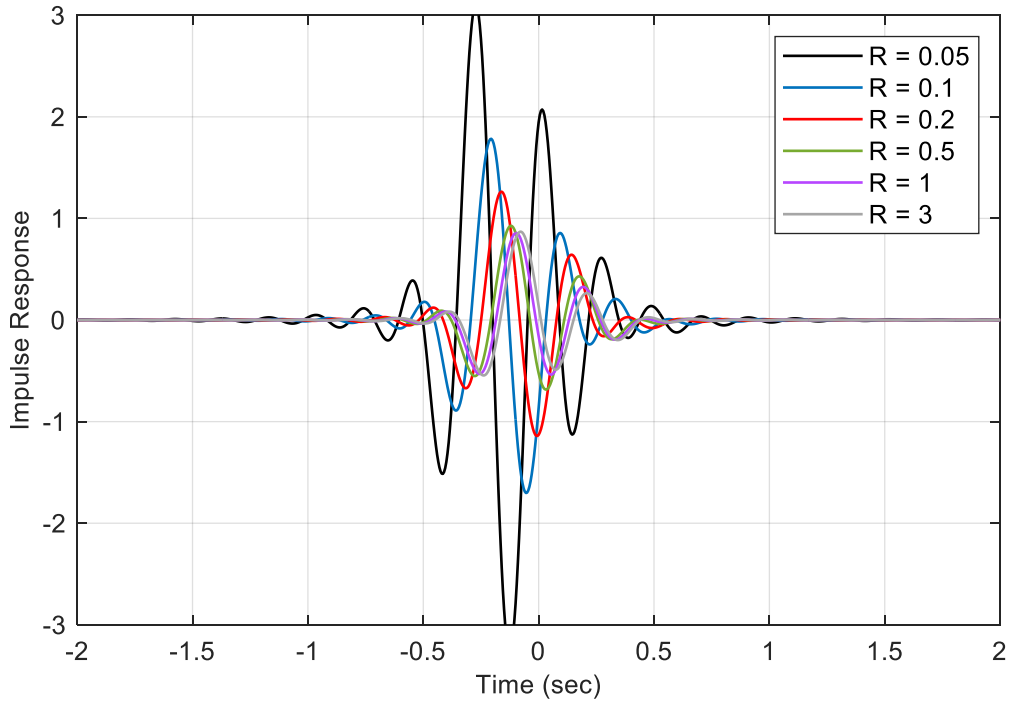
Figure 2.8. IRF Plots of a TB Model with 5% Damping, c_L = 25 and Varying R
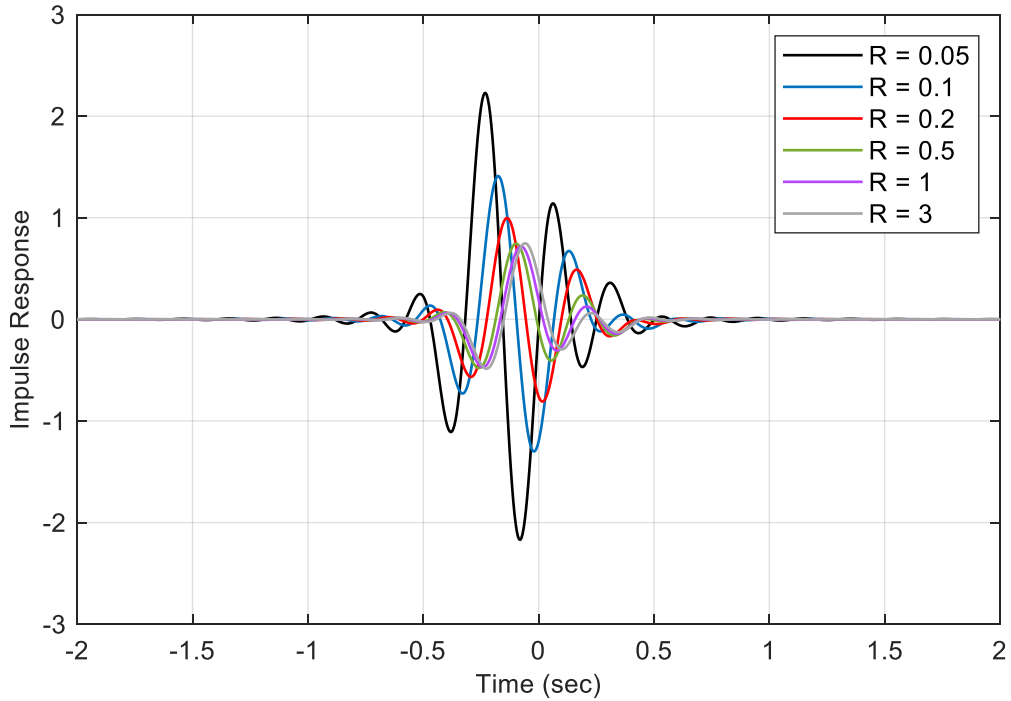
Figure 2.9. IRF Plots of a TB Model with 5% Damping, c_L = 30 and Varying R

Legend:
- 🟥 Large shifts
- 🟨 Small shifts
- 🟩 Not shifted
- **+** Marks positive shift in time
- **−** Marks negative shift in time

Damping=0.01 s

R \ $c_L \rightarrow$	15	20	25	30	35
0.01	−	−	−	−	−
0.05	−	−	−	−	−
0.1	−	−	−	−	−
0.15	−	−	−	−	
0.2	−	−	−		
0.25	−	−	−		
0.3	−	−	−		
0.4	−	−			
0.5	−	−			
0.7	−				+
1	−				+
3				+	+
5				+	+

Damping=0.05 s

R \ $c_L \rightarrow$	15	20	25	30	35
0.01	−	−	−	−	−
0.05	−	−	−	−	−
0.1	−	−	−		
0.15	−	−			
0.2	−	−			
0.25	−				+
0.3	−				+
0.4					+
0.5				+	+
0.7				+	+
1				+	+
3			+	+	+
5			+	+	+
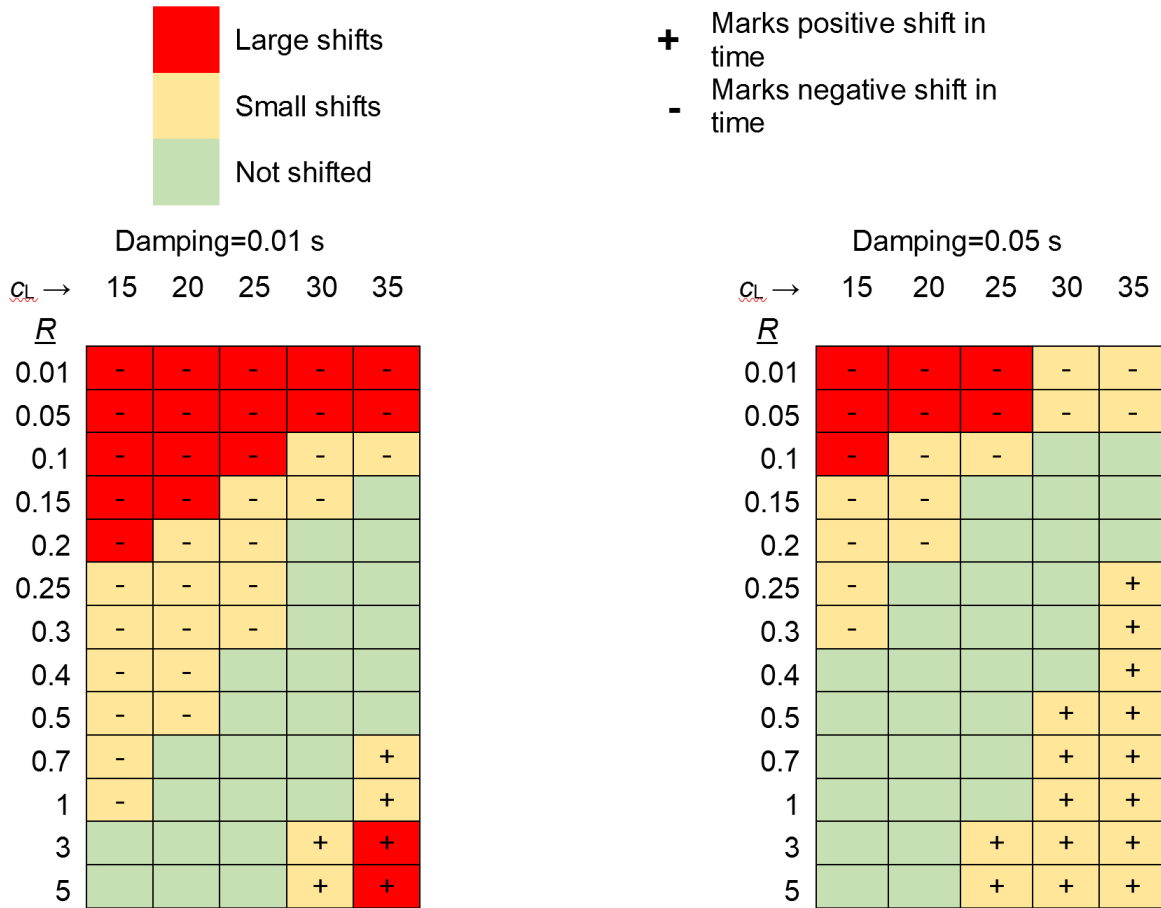
Figure 2.10 The Magnitude of Shift in the Main Pulses of the Impulse Response Functions for Various TB Model's c_L and R-*values*

2.3 The Case Study Bridge and Data

The prototype bridge analyzed in this report is one-quarter geometric scale of a real full-scale bridge. The tested prototype is a 4-span, 107-ft-long reinforced concrete bridge with a post-tensioned flat slab. The length of the two middle spans and the two end spans are 29 ft and 24.5 ft, respectively. The design drawing for the whole bridge is shown in Figure 2.11 per Nelson et al. (2007). The bridge has three bents, each consisting of two columns with a 12-inch diameter and a 15-inch depth cap beam on top of the columns. The bridge is situated along a reference north-south direction. The bents are numbered from south to north. Bent 1 (on the south side) is the shortest with a clear height of 5 feet. Bent 2 (at the middle) is the longest with a clear height of 7 feet. Finally, bent 3 (on the north side) has a clear height of 6 feet. Figure 2.12 illustrates an elevation view of the bents and their structural details.

The bridge comprises two special abutment seats with longitudinal induced movements. At each abutment seat, a horizontal dynamic actuator induces longitudinal movement in the seat to

replicate the abutment seats' interaction with the bridge structure, as well as the soil-abutment interaction. The deck is seated on the abutment with 0.5-inch gap on each end; hence, the abutment was expected to pound on the side of the deck during large amplitude motions. The bridge supports four pairs of 20-kip blocks (160 kips total) placed on four spans to provide a realistic superimposed load on the structure. Further, the bridge was supported at the bents by three isolated biaxial shake tables which excited the structure according to the testing sequence (Nelson et al, 2007). The shake table accelerations were scaled from records measured at the Century City Country Club station during the 1994 Northridge earthquake in California. The test sequence included seven horizontal orthogonal acceleration (referred here as *biaxial* motions) with increasing amplitude, except biaxial 6 and biaxial 7 motions, which were identical. Figure 2.13 shows the average target acceleration for all biaxial motion.

This model was built and tested at the University of Nevada, Reno (UNR) laboratory (Nelson et al., 2007). The UNR team used a nominal strength of 5,000 psi concrete and Grade 60 #3 and #6 reinforcing steel to construct the bridge columns and deck. Moreover, three longitudinal post-tensioning tendons, each with a tension force of 205 kips, were used in the slab.

A total of 22 accelerometers and 19 displacement transducers were deployed on the structure to collect vibrational data. These sensors were located at the top of three bents, the north and south end of the bridge deck, and the midpoint of each span. The array recorded the longitudinal, transverse and vertical acceleration, plus the transverse displacement of the bridge deck. Moreover, longitudinal displacements were measured only at the north and south ends. Figures 2.14 and 2.15 show the location of the sensors. The abbreviation "AT" denotes acceleration in the transverse direction and is followed by the channel number (e.g., AT3). We noticed that channels AT2 and AT4 were corrupted during the biaxial motions 1 through 3. However, these channels were not utilized in this study given our damage localization approach as discussed in Section 3.
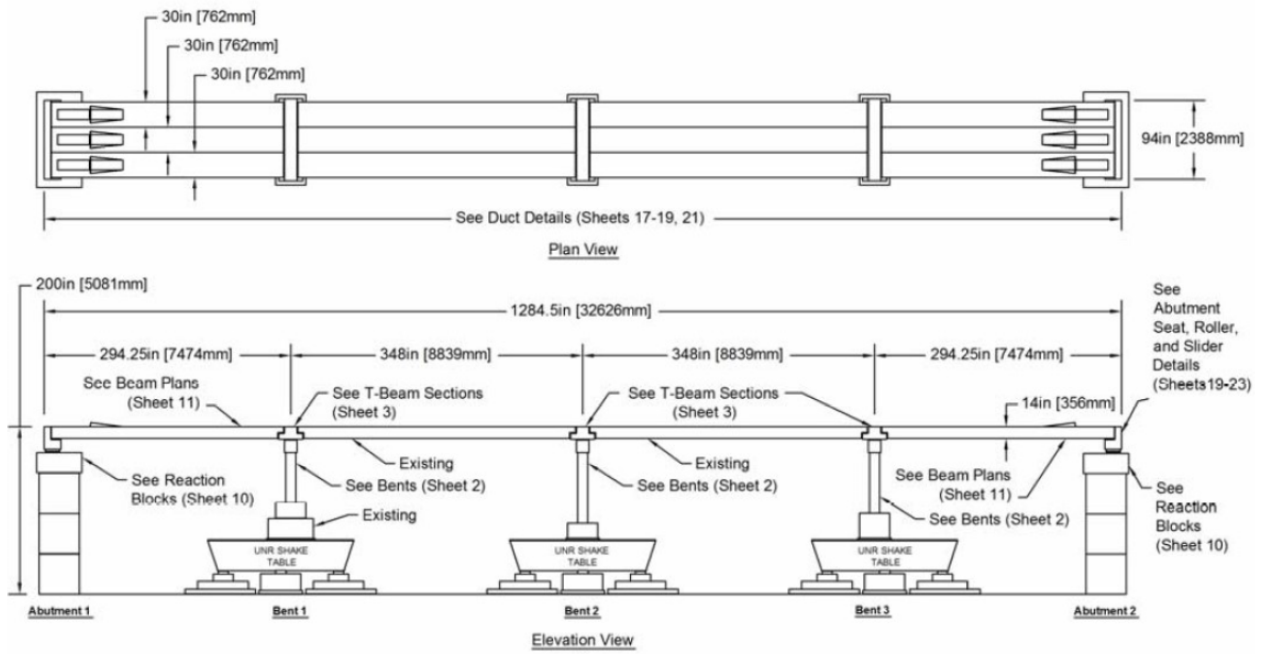
Source: Nelson et al. (2007)

Figure 2.11. Drawing of the Tested Bridge
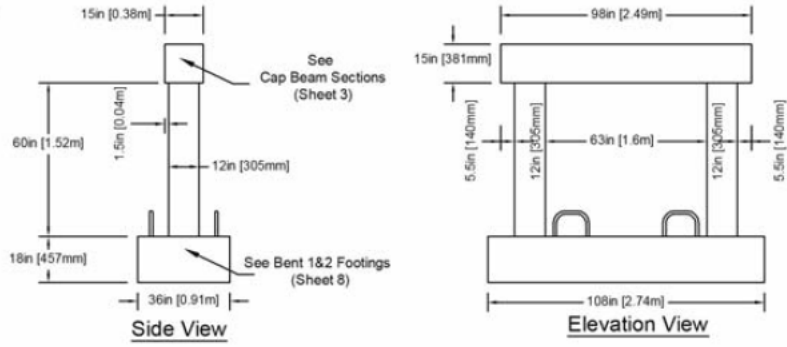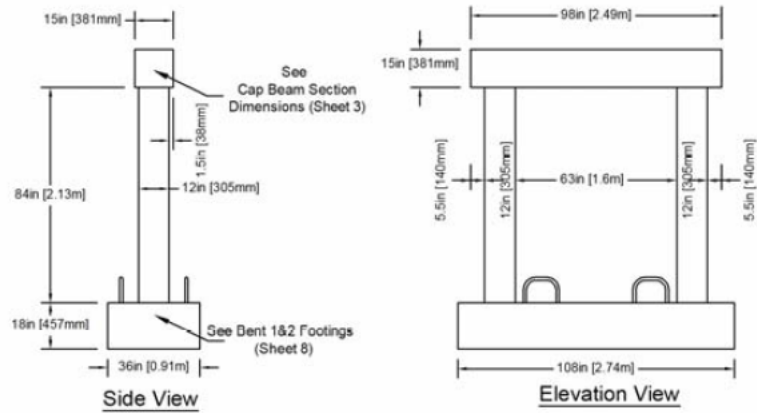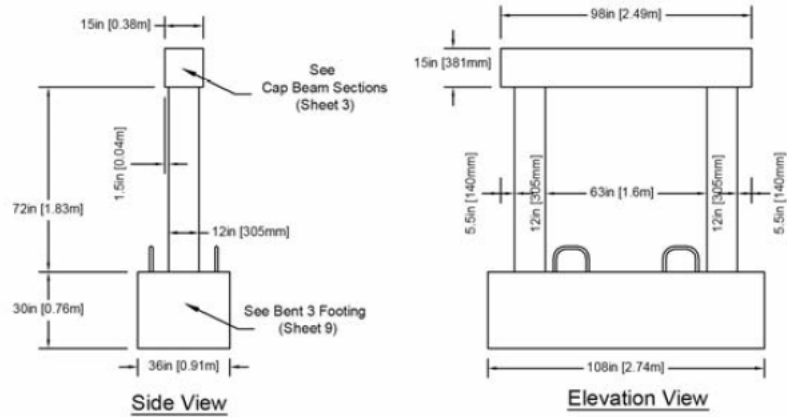
Source: Taken from Nelson et al. (2007)

Figure 2.12. Elevation View of the Three Bents
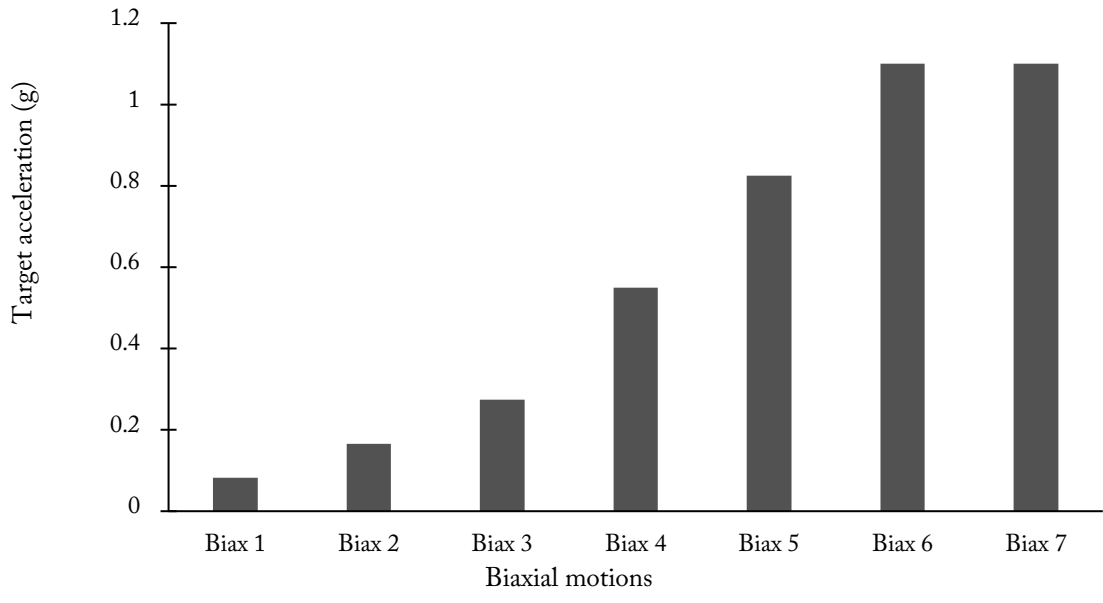
Figure 2.13. Average Target Acceleration at the Shake Tables During Actual
Bridge Test
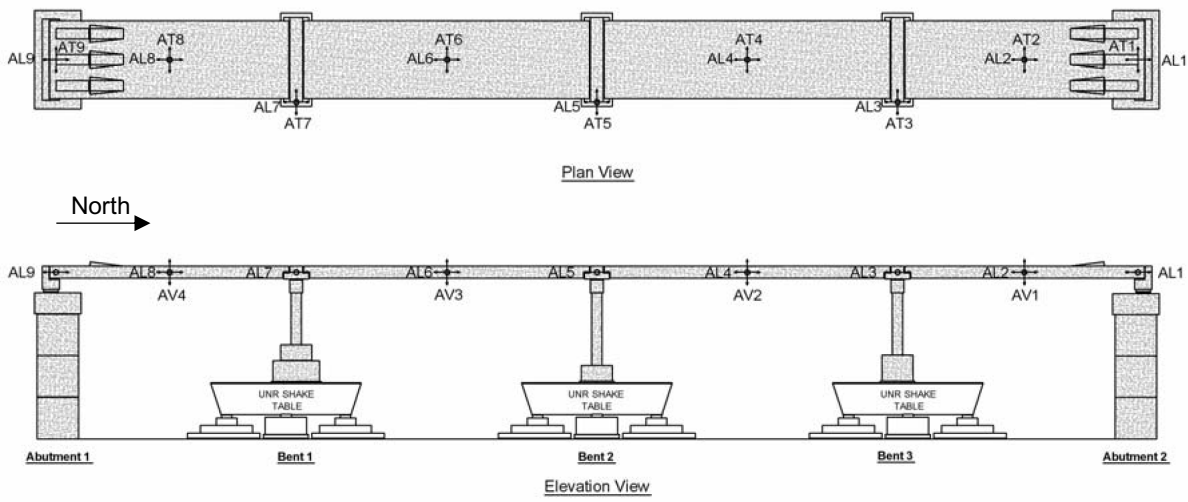
Source: Adapted from Nelson et al. (2007)

Figure 2.14. Locations of Accelerometers
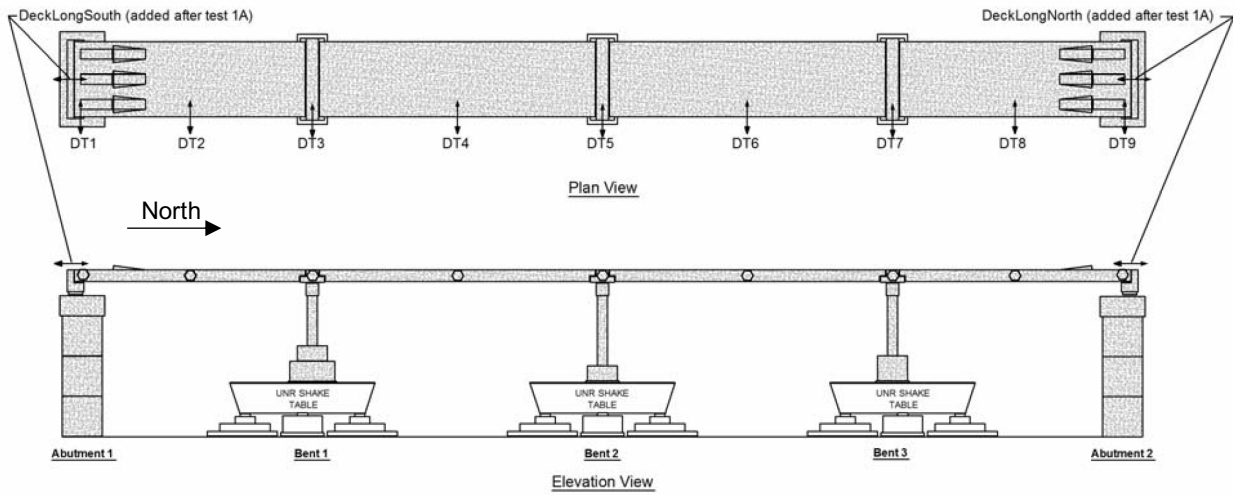
Source: Adapted from Nelson et al. (2007)

Figure 2.15. Locations of Displacement Sensors on the Deck Marked by DT#

3. Non-Linear Finite Element Model of the Bridge

As noted in Section 2, to better understand the sequence of modal frequencies and mode shapes of the tested case-study bridge, we created a nonlinear finite element model (FEM) for the bridge, and we updated the FEM based on recorded response for both the undamaged and damaged structure. Analyzing and assessing the FEM response is convenient and can provide valuable numerical and visual information about the bridge's vibrational response. The FEM also helped us identify an appropriate frequency passband ensuring to include at least the first translational mode of vibration while excluding high-frequency coupled torsional-translational modes. In this study, we performed our wave-based identification on acceleration data obtained from the FEM and compared the results with results from actual recorded data. The goal was to further assess the capability of our method in detecting damage and localizing in a computer model of the bridge with known degrees of damage. Updating the FEM was outside the scope of this study; hence, we updated the FEM by running several iterations. We created a model according to the structural drawing of the bridge. Next, we modified the cracked section properties for columns' concrete material, the location and length of nonlinear hinge zone at the columns, as well as the structure's damping ratios used for analysis. We performed several time-history analyses and compared the displacement and acceleration result obtained from the FEM with that of the actual bridge.

3.1 Structural Details of the Bridge FEM and Time History Analysis

We used SAP2000 software, a well-known structural analysis tool in the industry, to create a nonlinear FEM of the bridge. In this report, we call this computer model the FEM from this point on. Figure 3.1 shows the FEM's 3D view, and Figure 3.2 shows a zoomed-in view of the south abutment and bent 1 in detail. Superimposed dead loads (i.e., the blocks) and post-tensioning forces were applied in the model according to structural drawings and schedules. Table 3.1 presents material properties assigned in SAP2000 to model the tested bridge. A nonlinear time history analysis was carried out for each biaxial base excitation. The input base accelerations in our SAP2000 model were taken from recorded acceleration on top of the shake tables during each biaxial motion. A comparison of the accelerations recorded revealed that the three isolated tables were excited using the same input signal. Thus, our FEM analysis used the accelerations recorded at the middle table. We analyzed the model using each biaxial motion and extracted accelerations and displacements at nodes representing the actual sensors' locations in the tested bridge.

For our FEM, damping ratio was estimated from recorded data on the actual bridge. Damping affects the displacement response at the deck and its decay in time. A viscous Rayleigh damping was defined in SAP2000 such that it retuned a 3% damping ratio at a frequency of 1.2 Hz (i.e., slightly before the first observed mode of vibration) and a 5% damping ratio at 10 Hz (i.e., at the end of the analysis passband). The ratios were found by varying the damping between 1% to 8% by a 1% increment and picking the optimal damping ratios such that they resulted in the best match compared to the actual bridge displacement response.

As shown in Figure 2.5, the actual bridge was shaken by seven biaxial base motions, progressively damaging it to failure. The nonlinear FEM model, in SAP2000, was subjected to the same seven load cases, Biaxial 1 to the Biaxial 7, inducing similar degrees of damage in the model. The input motions are the longitudinal and transverse acceleration recorded on top of the bent 2 (the middle bent) shake table (ST2), and displacements recorded at the north and south abutment seats (i.e., reflecting the displacements induced by actuators at the abutments). Figures 3.3 through 3.6 show the input accelerations at the shake tables for biaxial 7. Raw acceleration data, at the shake tables and at the deck level, were extracted from NEESHub data repository for the original project (Nelson et al., 2007). The raw data showed shifted baselines (i.e., not starting from zero acceleration) which we further corrected using a MATLAB script. The baseline corrected signals were then used in our SAP2000 FEM (i.e., base excitation) and in our wave-based identification.

The nonlinear time history response analysis in SAP2000 includes a total of eight load cases as follows: The first load case involves a nonlinear static analysis that includes all gravity loads (self-weight and superimposed block loads) and the post-tensioning tendon forces. Figure 3.7 shows a screenshot of how the first load case is defined in SAP2000. Load cases 2 through 8 present the nonlinear time history motions during biaxials 1 through 7. The input signal's time step for biaxial 1 is 0.003906 seconds with a duration of 30 seconds total. The load case definition for biaxial 1 input motion in SAP2000 is shown in Figure 3.8. This load case includes a nonlinear time-history analysis starting after a state when the gravity and post-tensioning loads are fully in effect. The load cases for biaxial 2 to biaxial 7 were similarly defined, with the exception of their time step, which is 0.007812 seconds.
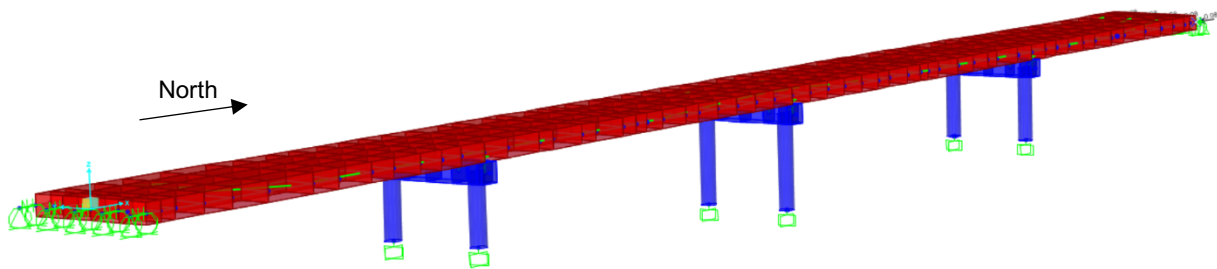
Figure 3.1. Bridge FEM 3D View from SAP2000, Concrete Deadload Blocks Not Shown

<center>(a)   (b)</center>
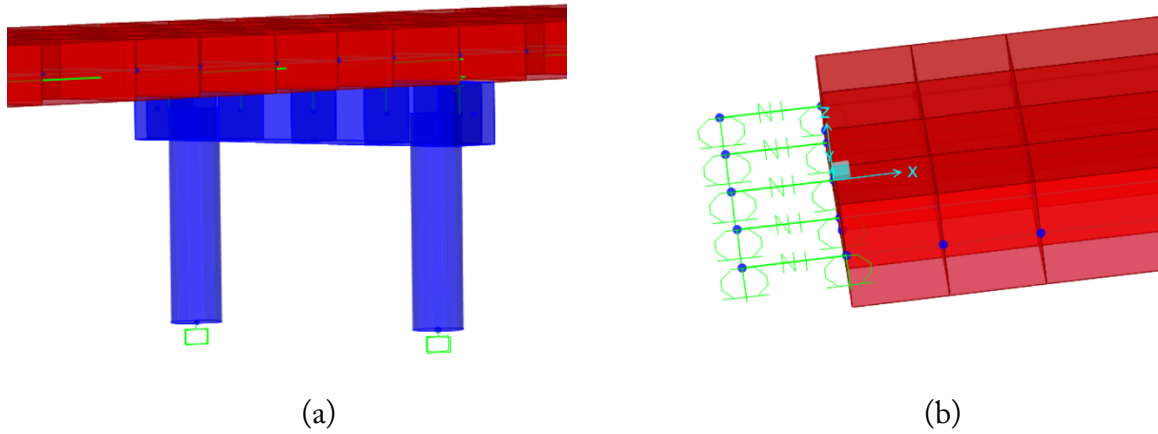
Figure 3.2. (a) Zoomed in for Bent 1 from SAP2000; (b) Zoomed in for South Abutment from SAP2000

Table 3.1. Defined Material Properties in SAP2000

Concrete			Steel rebar			
Compressive strength, f'c (ksi)	Modulus of elasticity, E (ksi)	Shear modulus, G (ksi)	Min. yield stress, Fy (ksi)	Min. tensile stress, Fu (ksi)	Expected yield stress, Fy (ksi)	Expected tensile stress, Fu (ksi)
5	4,030	1,679	60	90	66	99
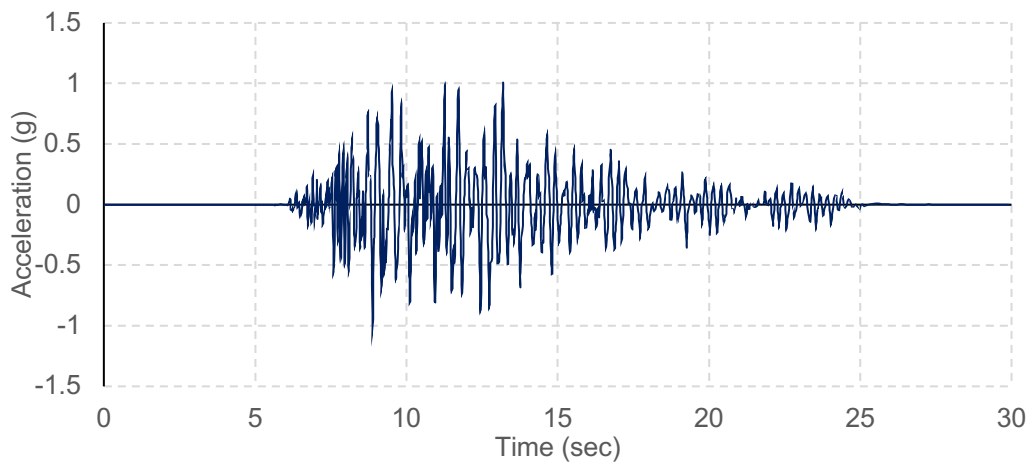
Figure 3.3. Transverse Acceleration input for Biaxial 7 at Shake Table 2 (ST2)
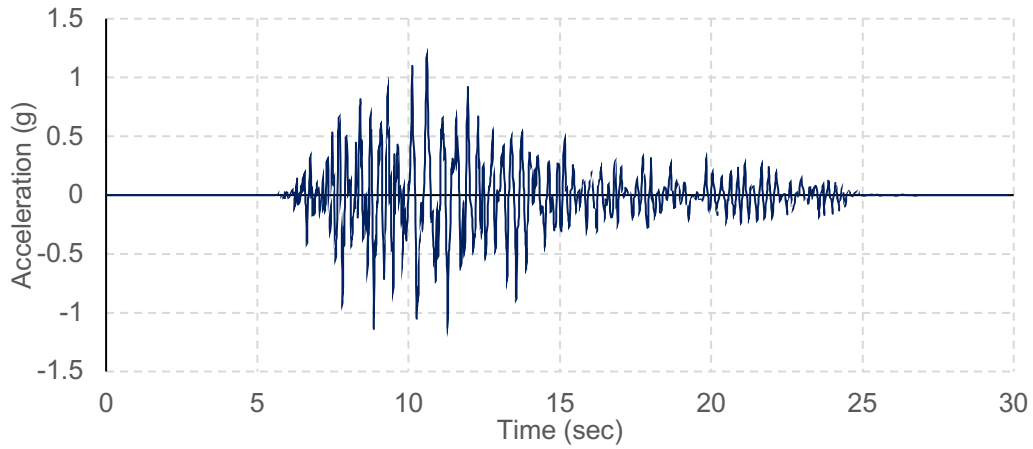
Figure 3.4. Longitudinal Acceleration input for Biaxial 7 ST2
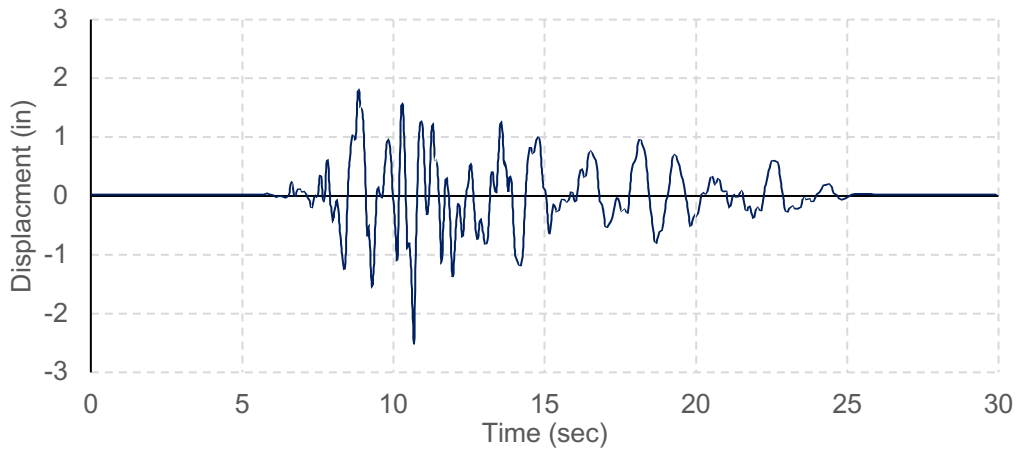
Figure 3.5. Longitudinal Displacement Input for Biaxial 7 at North Abutment Seat
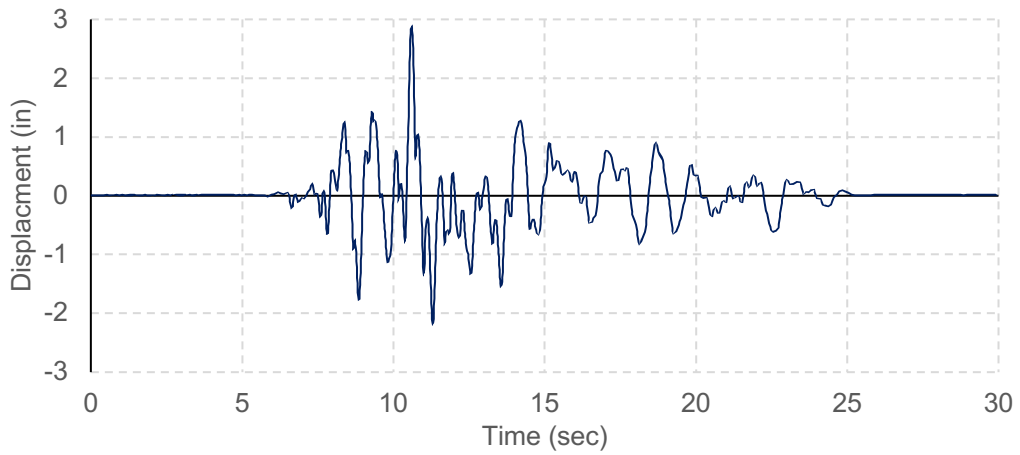
Figure 3.6. Longitudinal Displacement input for Biaxial 7 at South Abutment Seat
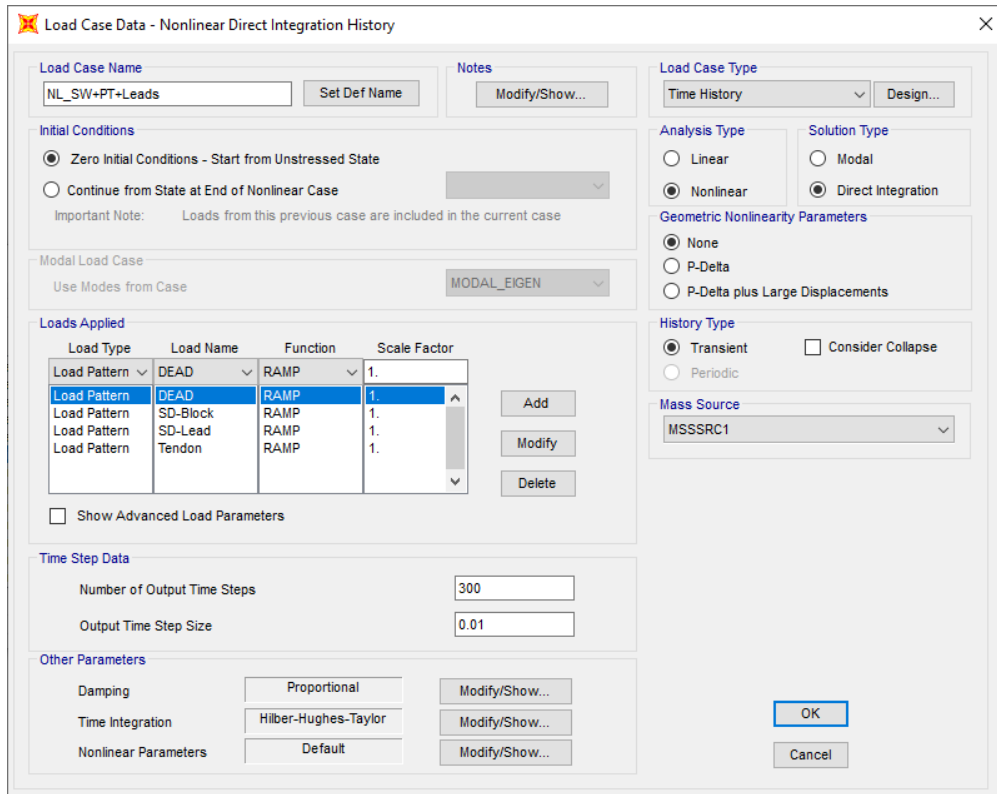
Figure 3.7 Gravity Load-Case Includes Dead Loads, Superimposed Load, and Tendon Forces
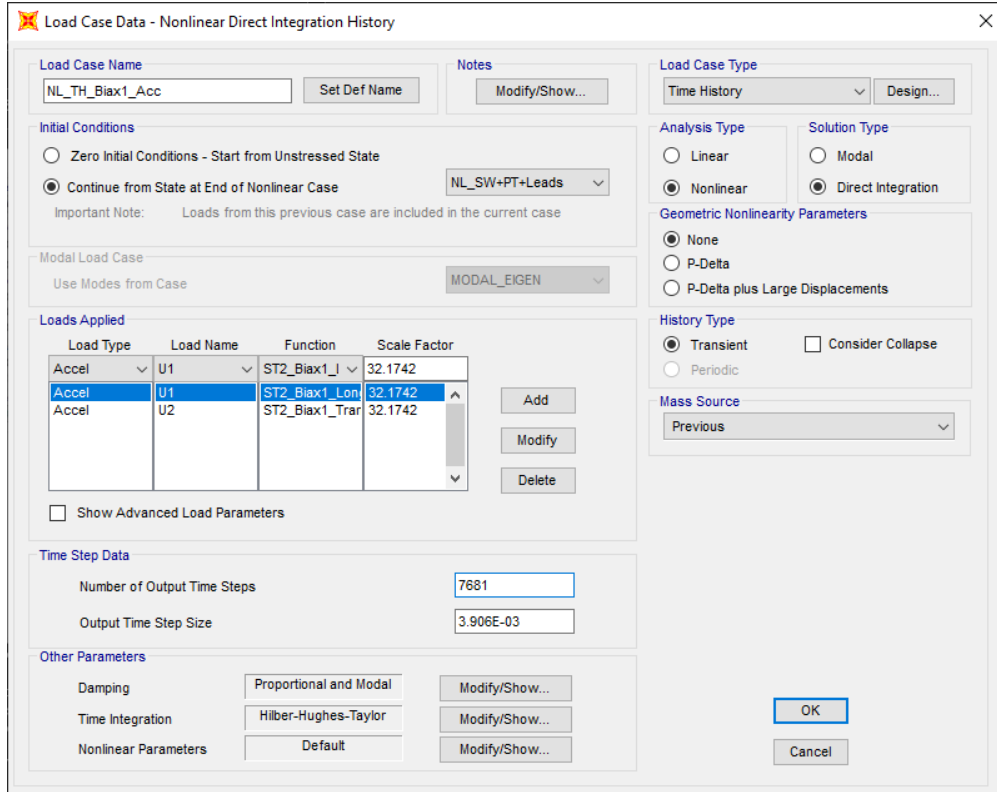
Figure 3.8. Nonlinear Time History Load-case Includes a Biaxial Motion in SAP2000

3.2 The Nonlinear Hinge Modeling for the Bridge

To accurately capture the nonlinear behavior of the actual bridge, definition of nonlinear hinges is crucial for the columns in the finite element bridge model. The columns incur the most nonlinear behavior in the bridge, especially when the biaxial motions' intensities are increased, and this is while the deck level is designed and expected to remain elastic throughout the test regime. In this study, we assigned two nonlinear hinges to each column: one is located 12 inches away from the top of the column, and the other is 12 inches away from the bottom of the column. The 12-inch distance from end-points is equal to the diameter of the columns, which is recommended by guidelines (NIST nonlinear modeling). The nonlinear hinges are defined using *fiber* hinge properties in SAP2000. The fiber hinges include longitudinal elements with different properties, known as fibers, representing nonlinear behavior of a designated material at a given location on the cross-section of a column. Herein, three types of fiber properties were defined and assigned to (1) unconfined concrete, (2) confined concrete, and (3) steel rebars. An example of hinge fibers' definition is shown in Figure 3.9. There is a total of 33 fibers per cross-section, including 8 fibers of unconfined concrete (a.k.a. cover concrete), 9 fibers of confined concrete (i.e., located at core), and 16 vertical steel rebars. The hysteresis behavior of concrete fibers was set to be of a *pinching* pattern (also known as a *pivot* model). For steel rebars' fibers, a *kinematic* hysteresis model was used in the SAP2000. Figure 3.10 illustrates the backbone curve and hysteresis behavior of an unconfined (i.e., covered) concrete fiber located at bents 1 and 2 during biaxials 3 and 5 excitations. The cover concrete fails at the biaxial 4 motion for bent 1 and at biaxial 5 for bent 2. Figure 3.11 shows an individual confined (i.e., core) concrete fiber in the same fiber hinge, and Figure 3.12 shows an individual rebar fiber during biaxials 3 and 6 motion. Note that rebars in the actual bridge significantly yielded during biaxial 6 motion at bent 1, consistent with this bent's hysteresis loops.

3.3 Acceleration and Displacement Response: FEM vs. Actual Bridge

The case study bridge has 22 accelerometers and 19 displacement transducers deployed on its deck, abutment, and shake tables. Reviewing these recorded data, especially the displacement response, and comparing them with our FEM response revealed that the bridge response in the longitudinal direction (north-south) is very complex due to its interaction with abutment seats. In larger motions (e.g., biaxial 2 motion and after), the bridge's longitudinal movement along with induced movements in the abutment seats caused deck and abutment pounding as reflected in the response. However, the bridge's transverse motion is not restricted by the abutments or shear keys. Only the columns provide lateral resistance in the transverse direction. Our comparison of the displacement response between the actual bridge and our FEM shows very good agreement, affirming less complexity in the transverse direction response compared to longitudinal direction. Hence, we used the bridge's transverse response for our identification and damage detection process.

The bridge had nine transverse accelerometers (AT) and displacement transducers (DT) in the transverse direction as seen in Figures 2.14 and 2.15. From our FEM, we extracted the acceleration and displacement response at nine nodes corresponding to where real sensors were located.

Table 3.2 shows the FEM node number and its corresponding AT. To show our FEM updating's goodness, we compared the extracted response with the bridge's actual recorded response.

Table 3.2 Node Number in the FEM Corresponding to Sensors in Actual Bridge

SAP2000 Node #	368	361	46	16	23	28	3	97	90
Sensors	AT1	AT2	AT3	AT4	AT5	AT6	AT7	AT8	AT9
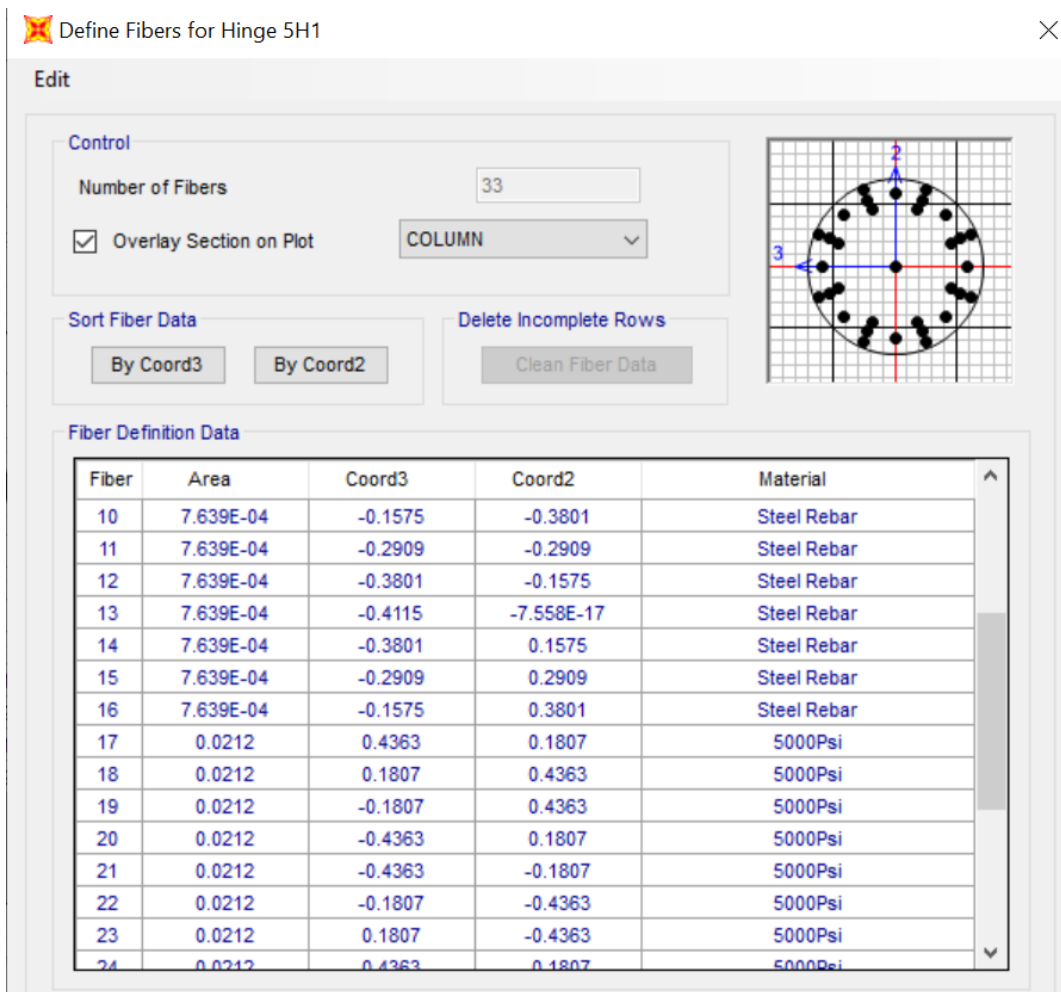
Figure 3.9. Nonlinear Hinge at the Bottom of a Column in Bent 1
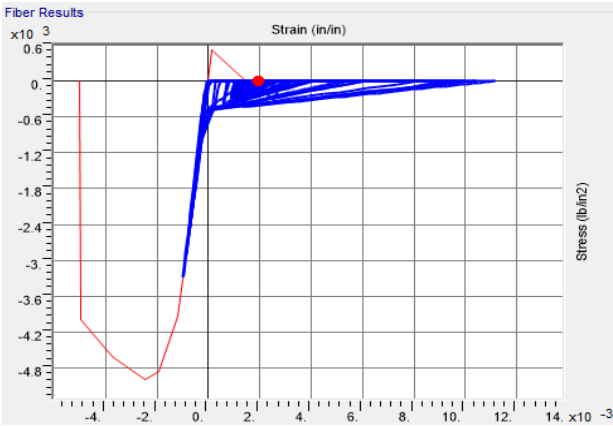
(a) Bent 1 during biaxial 3
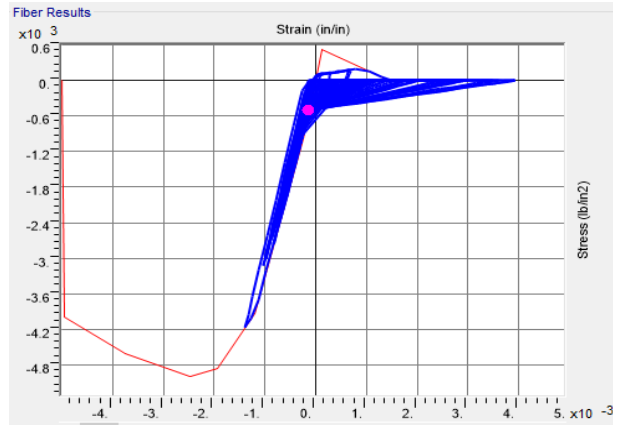
(b) Bent 2 during biaxial 3
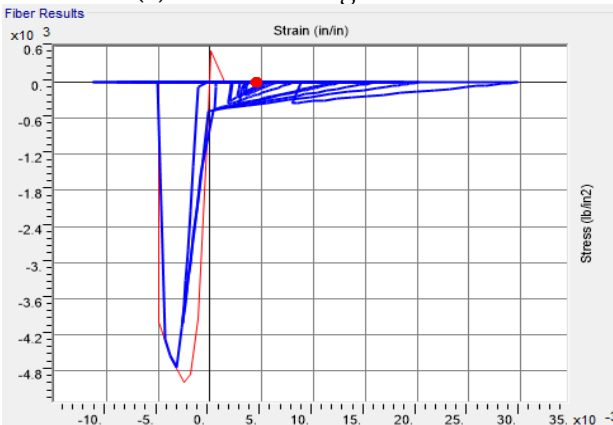
(c) Bent 1 during biaxial 5
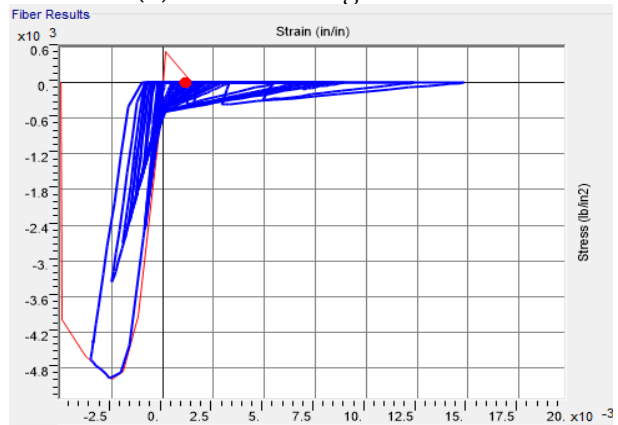
(d) Bent 2 during biaxial 5

Figure 3.10. Individual Fiber Response: The Cover Concrete (outer shell) Fiber's Nonlinear Behavior for Biaxials 3 and 5 Motions
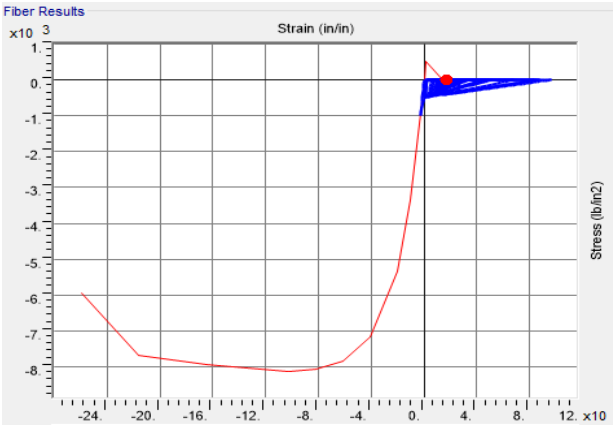
(a) Bent 1 during biaxial 3
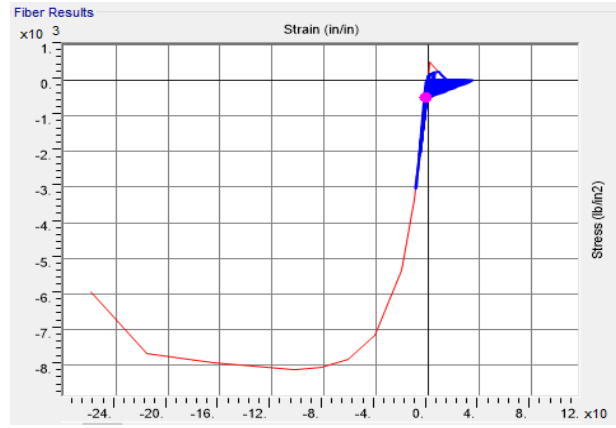
(b) Bent 2 during biaxial 3
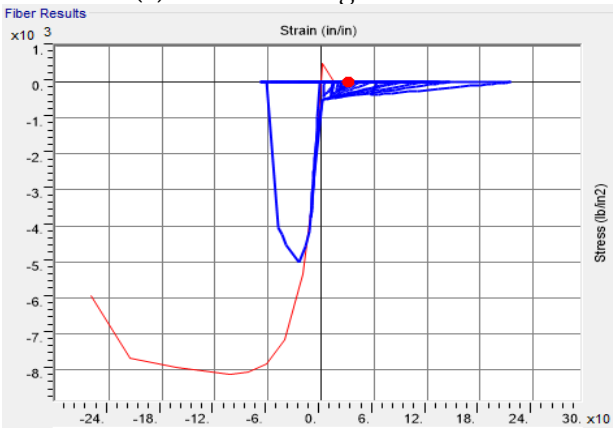
(c) Bent 1 during biaxial 5
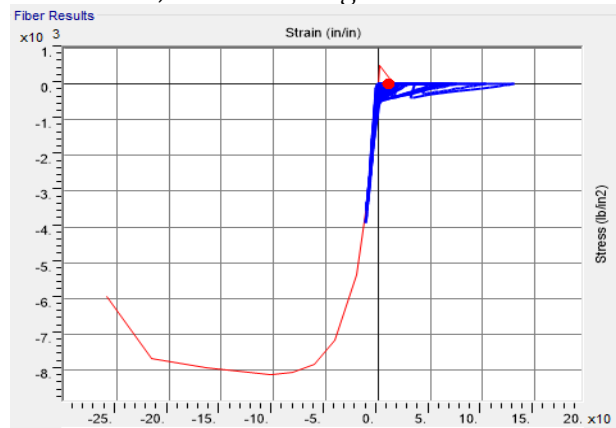
(d) Bent 2 during biaxial 5

Figure 3.11. Individual Fiber Response: Confined Concrete (i.e., core) Fiber's Nonlinear Behavior for Biaxial 3 and Biaxial 5 Motions

(a) Bent 1 during biaxial 3   (b) Bent 2 during biaxial 3

(c) Bent 1 during biaxial 6   (d) Bent 2 during biaxial 6
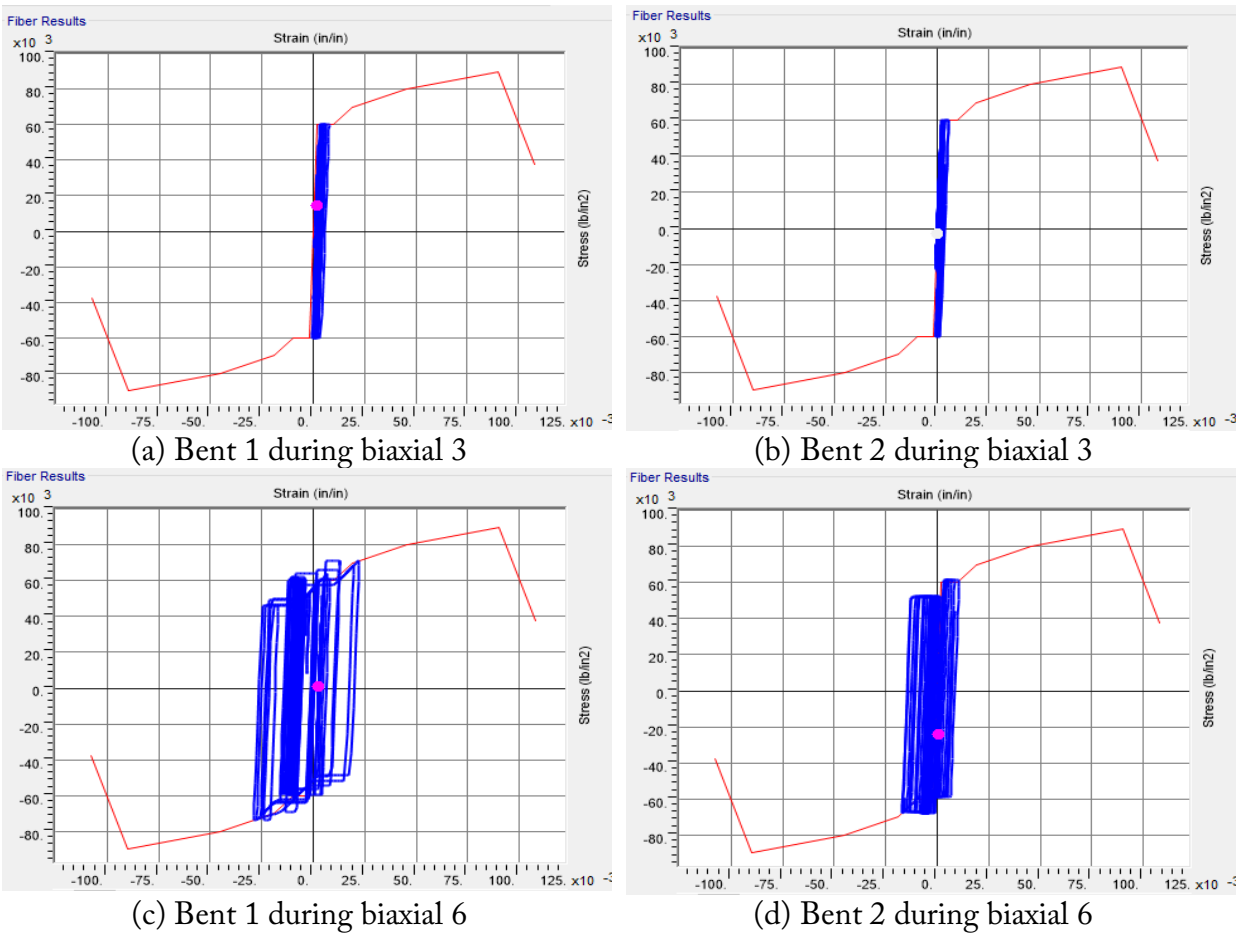
Figure 3.12. Individual Fiber Response: Steel Rebar Fiber's Nonlinear Behavior
for Biaxial 3 and Biaxial 6 Motions

For the FEM, the displacement time history response is calculated, in SAP2000, using a double integration of acceleration response. As a result, for nonlinear time history responses, often, the integration introduces constants or a higher-order degree of shift with time in the calculated displacement. Figure 3.13 shows one example of extracted displacement from the FEM for biaxial 3 motion at channel DT3. When compared to actual recorded data (also referred to as *observed* response), the calculated displacement has a shifted and inclined baseline (see Figure 3.13). This error is typical when displacement time history is being calculated in FEM software, which requires a baseline correction. For this purpose, authors wrote a MATLAB script which finds the baseline by fitting a polynomial function (varying order from 1 to 3) such that it results in a corrected time series with no vertical shift or with apparent symmetry around the horizontal axis. Figure 3.14 shows the same biaxial 3 channel DT3 response, with baseline correction on FEM data. The baseline correction works well for most displacements, except (1) it introduces an artificial wavy start and end to the signal when a significantly wavy baseline is being corrected, and (2) it corrects residual displacement observed at deck levels in a damaged bridge during large motions (e.g., biaxials 5 to 7). Therefore, the comparison between the actual response and the FEM should take into account these deficiencies. Figures 3.15 to 3.21 show comparisons

between the *observed* (i.e., recorded) displacement and the FEM displacement in the transverse direction for biaxial 7 motions (channels AT2 through AT8). Figure 3.22 shows similar plots for the longitudinal direction for the north end of the deck. The plots show that agreement between the FEM and the observed response is very good, verifying the goodness of our updated FEM. In addition to the errors introduced by baseline corrections, other modeling approximations, such as damping ratio assumption, nonlinear hinge properties, and gap modeling between the bridge deck and abutment can contribute to small differences between the FEM and observed response. In summary, our FEM is a reasonably good tool to help understand the actual bridge's vibrational response and to test our wave method's capability of localizing damage in it.

A comparison of the deck acceleration time history between FEM and recorded response presents reasonable agreement: specifically, there is a good match in the acceleration amplitudes. Importantly, the matching acceleration response, especially in the motion's high-frequency segments, is challenging due to fine detailing and bridge mechanisms not modeled in our FEM. The FEM's transverse acceleration plots and recorded response for biaxial 7 motions are illustrated in Figures 3.23 and 3.24. Note that biaxial 7 is the last and largest motion the bridge experienced which caused the most significant nonlinearity in the structure. While there is reasonable agreement between the FEM and recorded response, the differences observed can be attributed to our modeling approximations and assumptions (e.g., damping model in the SAP2000, etc.).
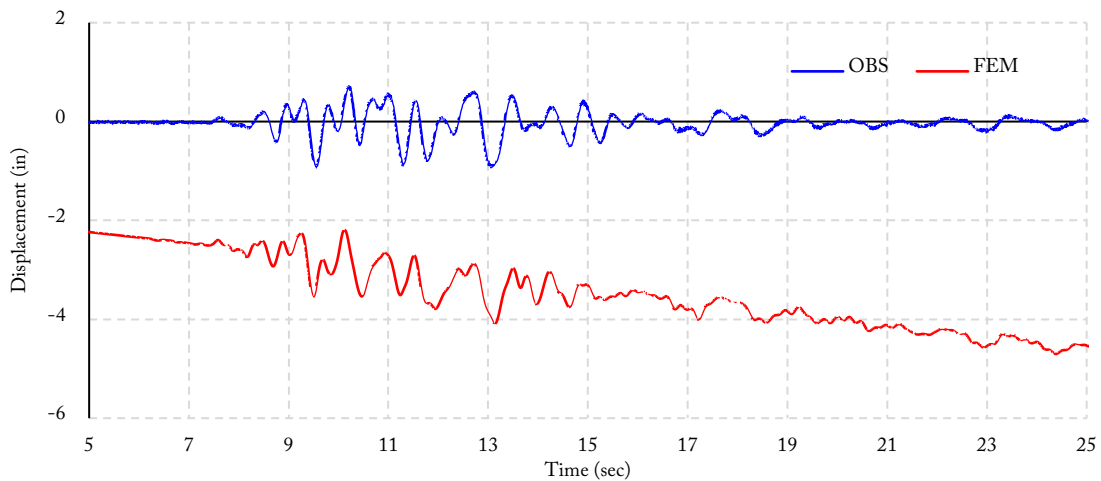
Figure 3.13. Displacement Agreement for Biaxial 3, Channel DT3, With Raw FEM Data
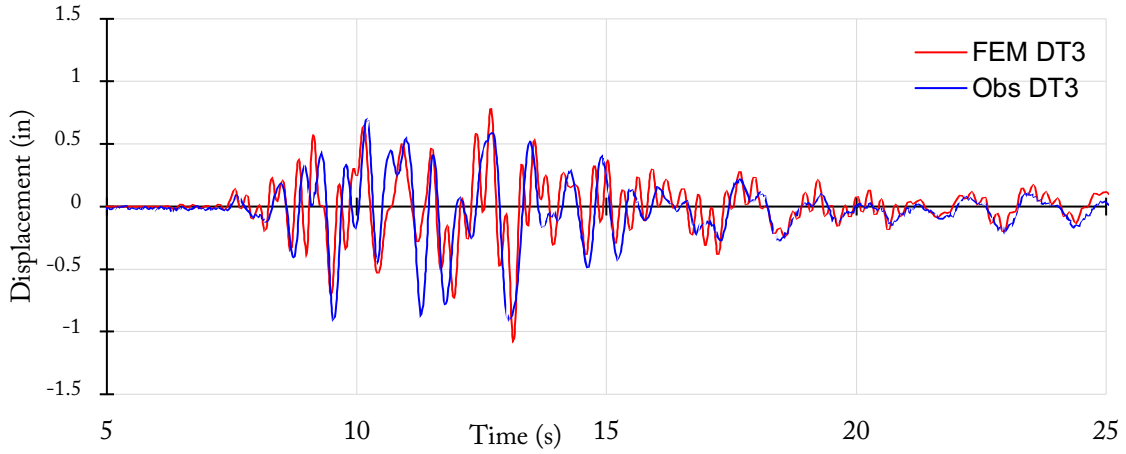
Figure 3.14. Displacement Agreement for Biaxial 3 DT3 Channel (Located on Top of Bent 1) with Baseline Correction FEM Data
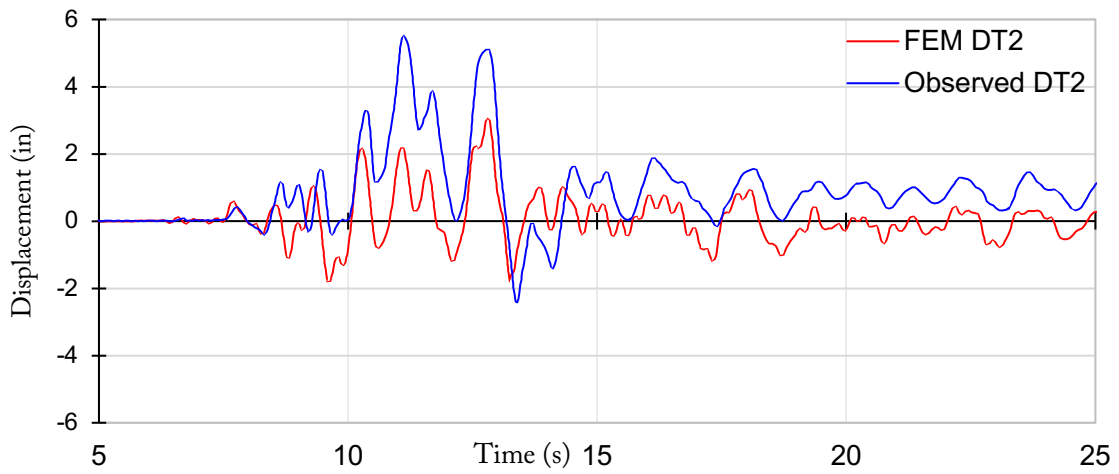
Figure 3.15. Transverse Displacement Agreement for Biaxial 7 DT2 with Baseline Correction FEM Data
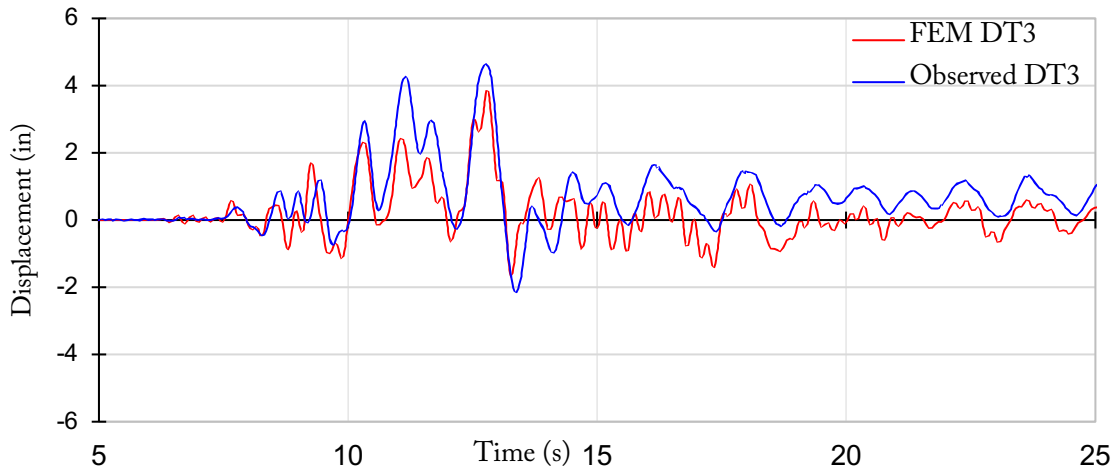
Figure 3.16. Transverse Displacement Agreement for Biaxial 7 DT3 with Baseline Correction FEM Data
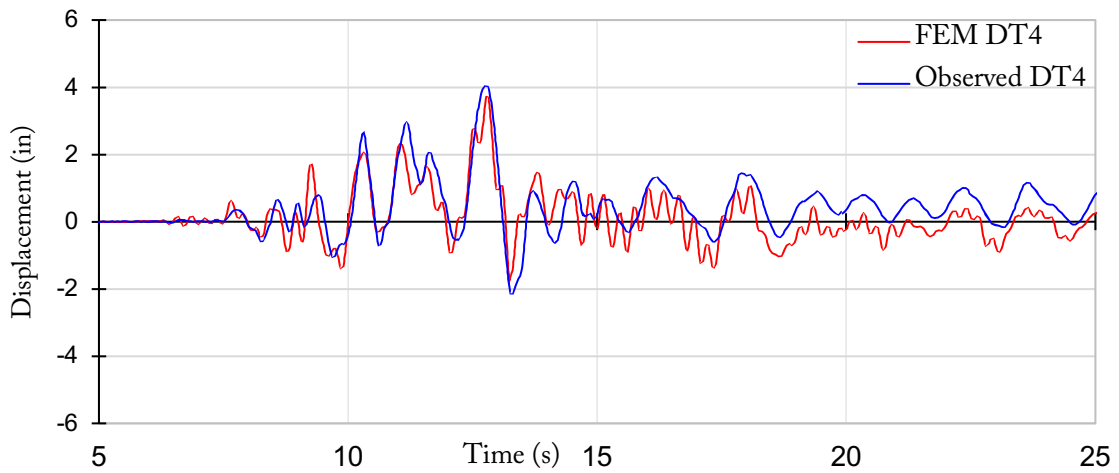
Figure 3.17. Transverse Displacement Agreement for Biaxial 7 DT4 with Baseline Correction FEM Data
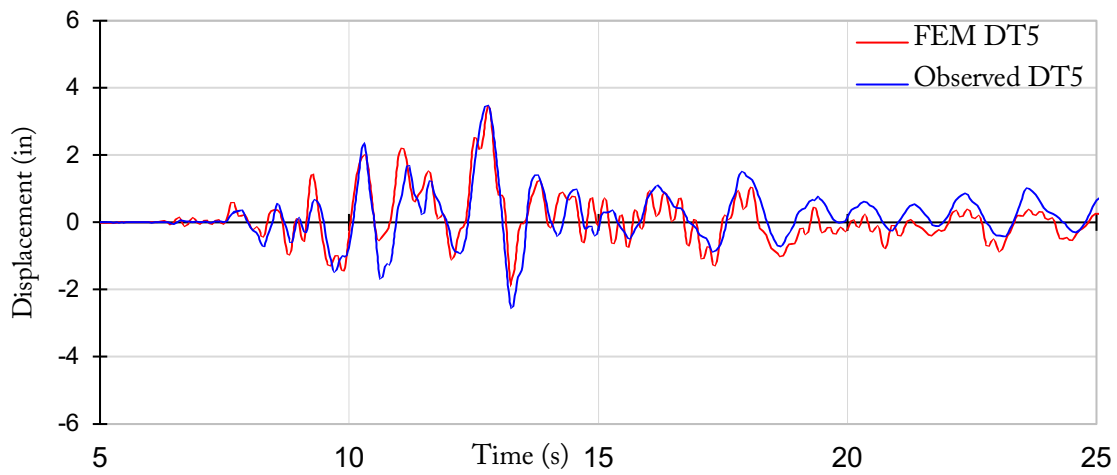
Figure 3.18. Transverse Displacement Agreement for Biaxial 7 DT5 with Baseline Correction FEM Data
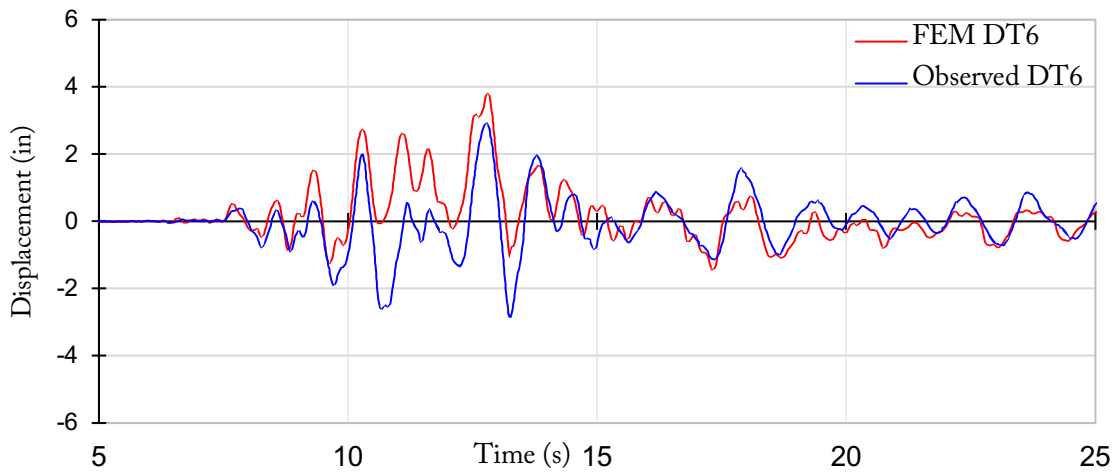
Figure 3.19. Transverse Displacement Agreement for Biaxial 7 DT6 With Baseline Correction FEM Data
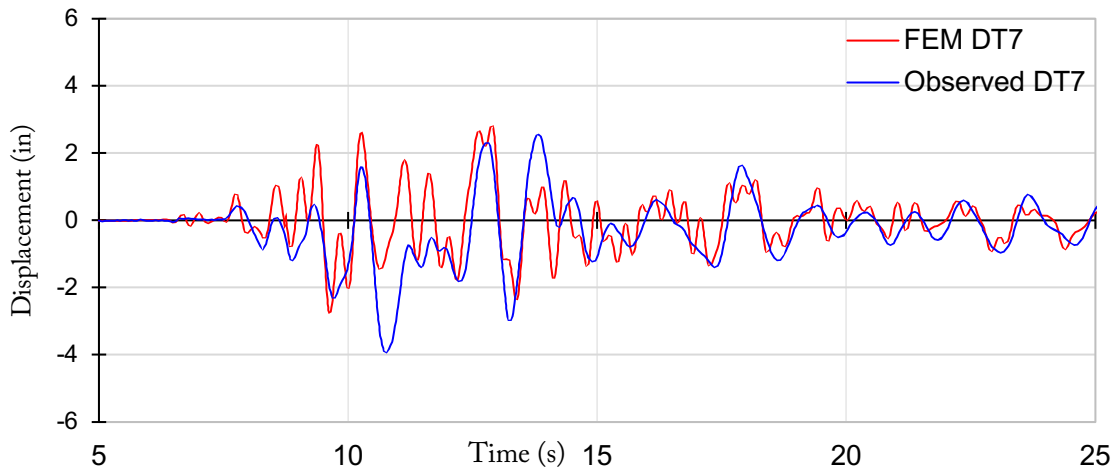
Figure 3.20. Transverse Displacement Agreement for Biaxial 7 DT7 With Baseline Correction FEM Data
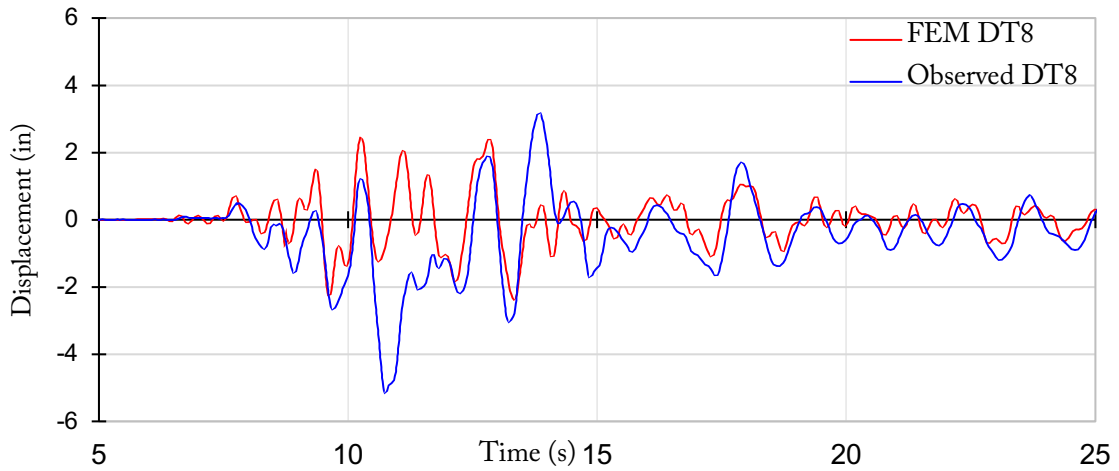
Figure 3.21. Transverse Displacement Agreement for Biaxial 7 DT8 With Baseline Correction FEM Data
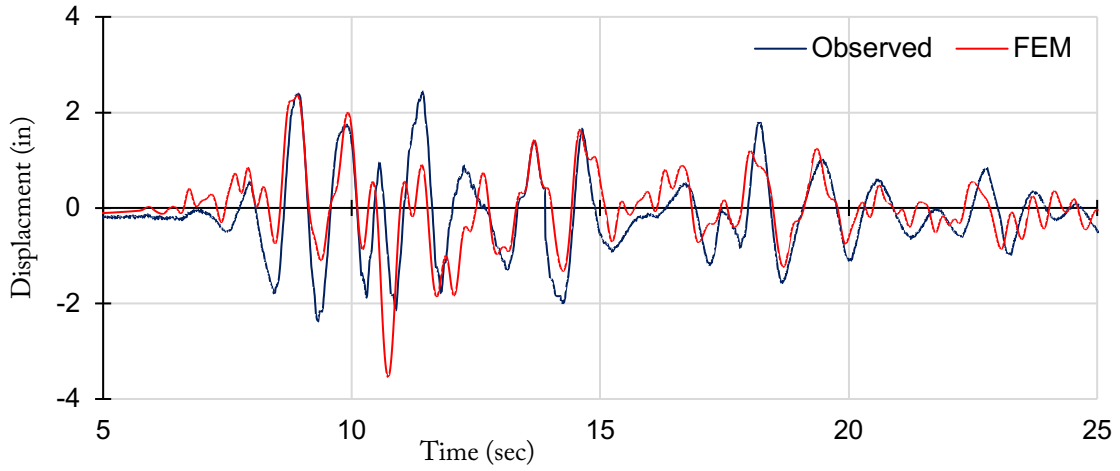
Figure 3.22. Longitudinal Displacement Agreement for Biaxial 7 at North End of the Deck
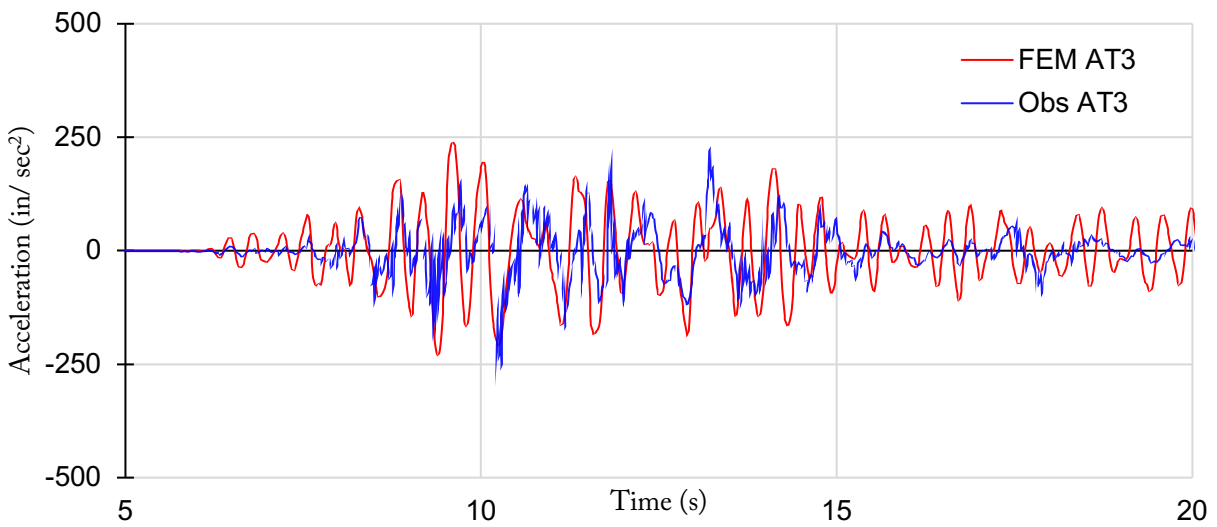
Figure 3.23. Transverse Acceleration Comparison for Biaxial 7 AT3 Between FEM and
Actual Bridge Data
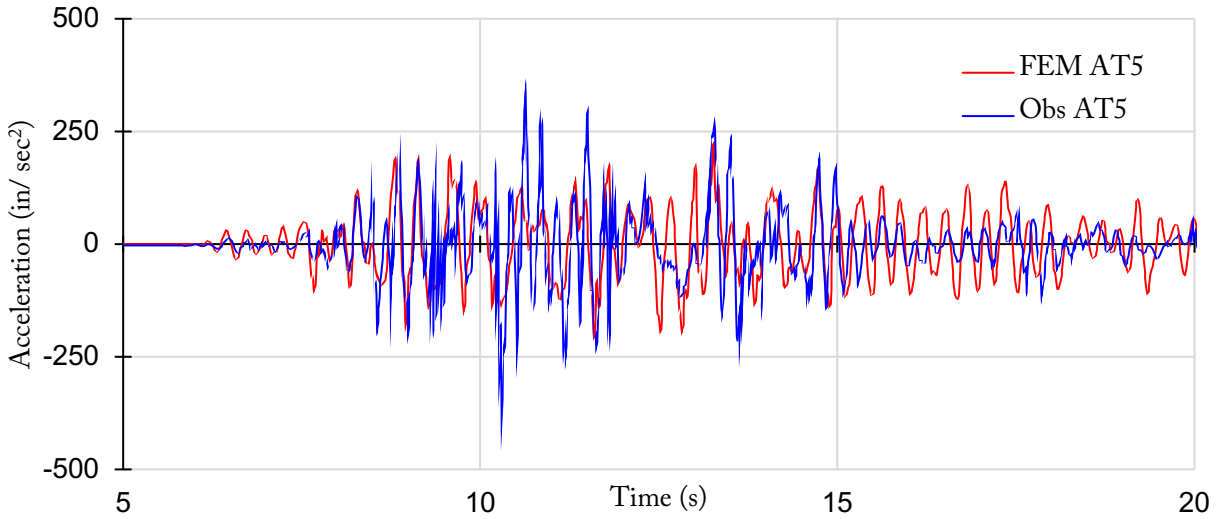
Figure 3.24. Transverse Acceleration Comparison for Biaxial 7 AT5 Between FEM and Actual Bridge Data

3.4 Nonlinear Hinge Response of the Bridge's FEM

Nonlinear time history analysis was carried out using our FEM for all seven biaxial motions. As discussed earlier in the report, nonlinear fiber hinges were defined at the base and top of the columns. Figure 3.25 shows examples of moment-rotation plots at the bottom of bent 1 (east column) during biaxial motions 1, 3, 5, and 7. The plots illustrate the overall hysteresis behavior of a group of fibers in a column. It shows that the FEM captures a more significant degree of nonlinearity in the base of columns from smaller shaking (biaxial 1) to larger-amplitude shaking (biaxial 7). The hysteresis loops suggest that bent 1 sustained severe damage, consistent with the surveyed damage in the actual bridge. This updated and verified FEM can serve as an alternative and convenient case study to apply our wave method to detect and localize damage.
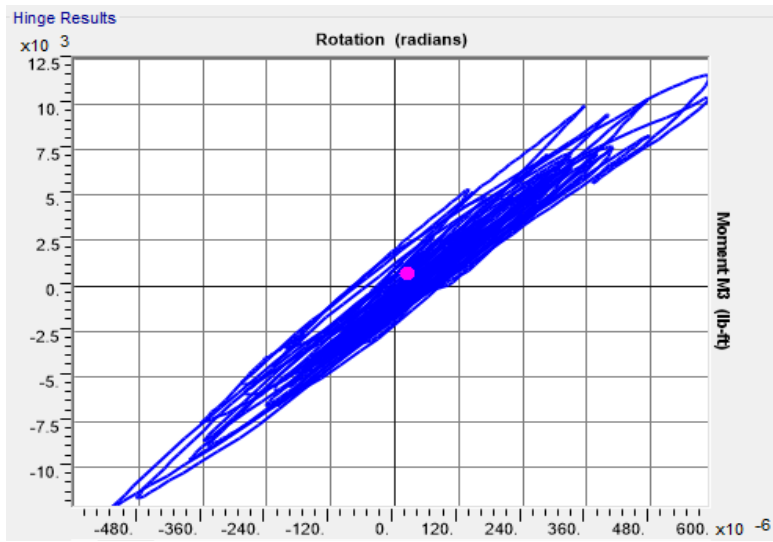
a) Biaxial 1 Motion

b) Biaxial 3 Motion

c) Biaxial 5 Motion
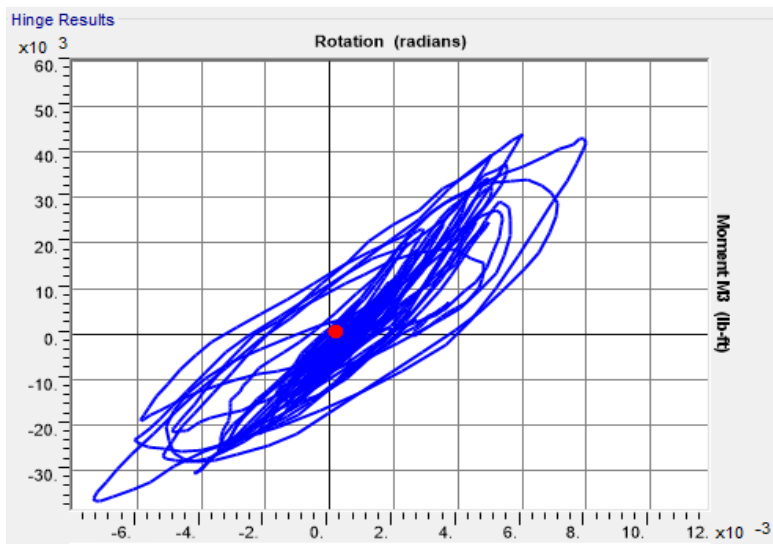
d) Biaxial 7 Motion
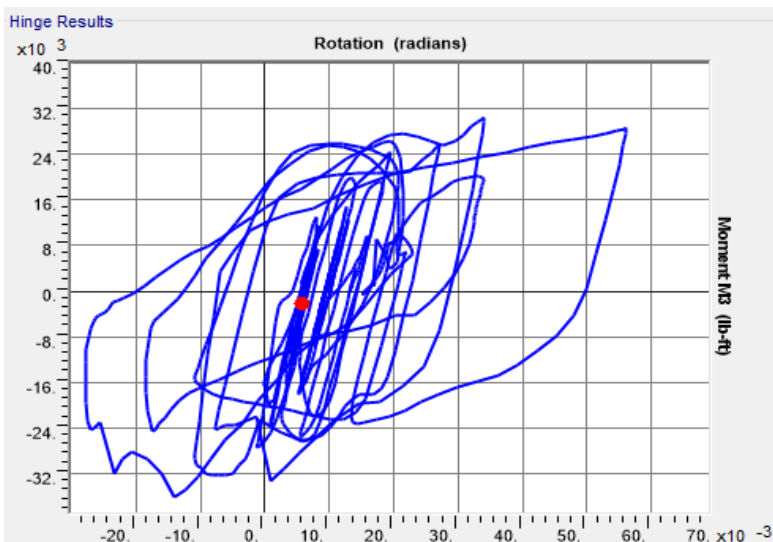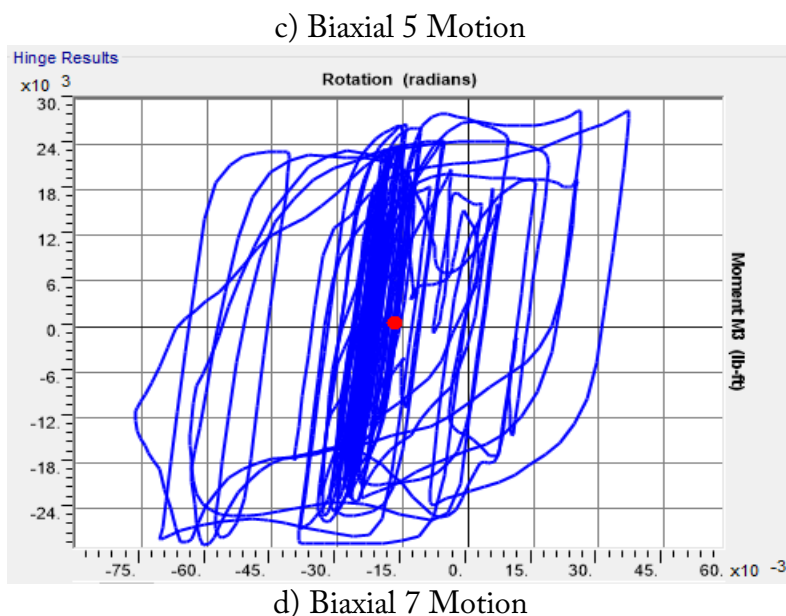
Figure 3.25. Nonlinear Fiber Hinge Result at the Bottom of Bent 1 (East Column)
During Biaxial Motions 1, 3, 5, and 7

As described in this report's methodology section, the waveform inversion algorithm involves calculating the impulse response functions (IRFs) from the response transfer functions (TFs), and then fitting them using the IRFs of a Timoshenko beam model. Therefore, the FEM could be considered a good representative of the actual bridge only if we can show reasonable agreement in the IRFs and TFs for selected pairs of sensors, and a comparison between the actual bridge and the FEM data is presented herein. The frequency band used in this comparison is 0–8 Hz. Figures 3.26 to 3.32 show the TFs for the acceleration pair AT3 and ST3 for all shakings. As the plots show, the TFs from FEM are in good agreement with those of the recorded data. The fundamental mode of vibration (in the transverse direction) from the FEM and actual bridge also matches each other reasonably well. These modal frequencies agree better for larger amplitude biaxial motions during which the bridge response becomes nonlinear.

Figures 3.33 to 3.37 present a comparison of the IRFs for AT3 with respect to ST3 (i.e., the pair of sensors at bent 3) for five larger motions. As the graphs show, the amplitude of impulse responses and their shifts in time are affected by the intensity of the excitation when biaxial motions are increasing. The IRFs for the FEM and the actual bridge show slight differences, but overall, the pulse shifts and amplitudes are in fair agreement.

In summary, we showed a comparison of the TFs and the IRFs as well as transverse displacement responses for the FEM and the actual bridge, proving that our updated FEM resembles the nonlinear response of the actual bridge reasonably well. There are small differences between IRFs of the model and the actual bridge which could be attributed to modeling approximations, such as damping ratio used in the FEM, the true response at the abutment and its effect on the overall bridge response, and the nonlinear hinge properties at the columns. In this study, we only use the

FEM as a good stand-alone case study to test the capability of our wave method, and while we expect a difference in the identification results obtained from the FEM and the tested bridge, we also anticipate very close degradation trends in both examples.
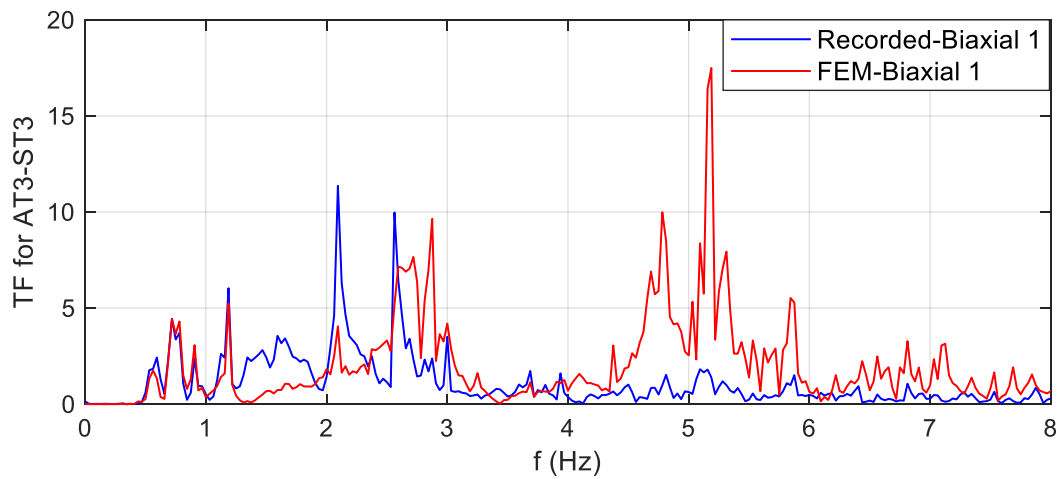
Figure 3.26. A Comparison Between Transfer Function of Recorded Acceleration Response vs. the FE Model Response for AT3-ST3 Pair (Biaxial 1 Motion)
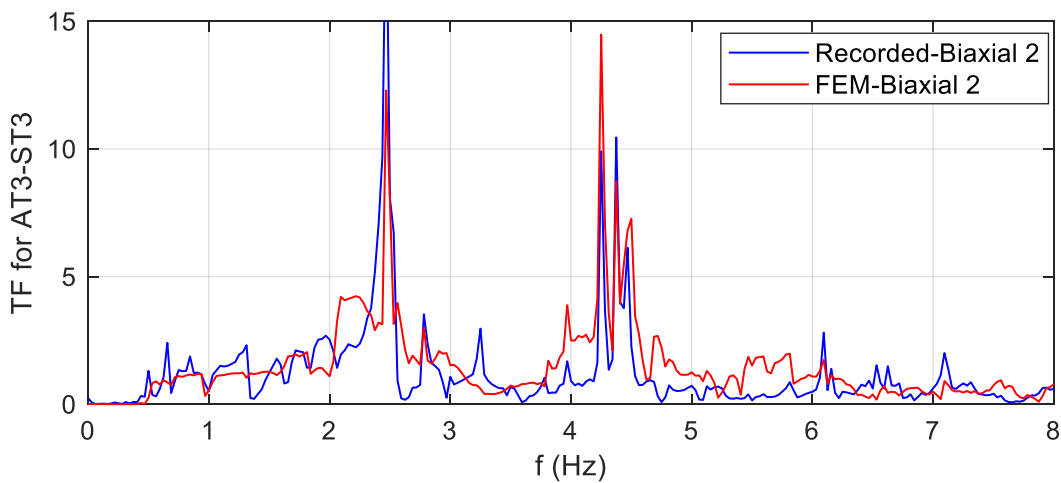
Figure 3.27. A Comparison Between Transfer Function of Recorded Acceleration Response vs. the FEM Response for AT3-ST3 Pair (Biaxial 2 Motion)
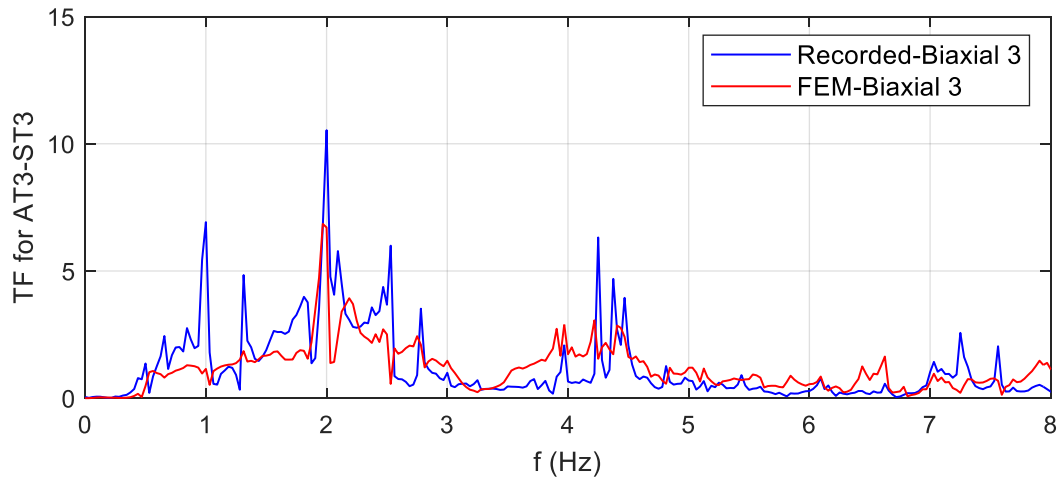
Figure 3.28. A Comparison Between Transfer Function of Recorded Acceleration Response vs. the FE Model Response for AT3-ST3 Pair (Biaxial 3 Motion)
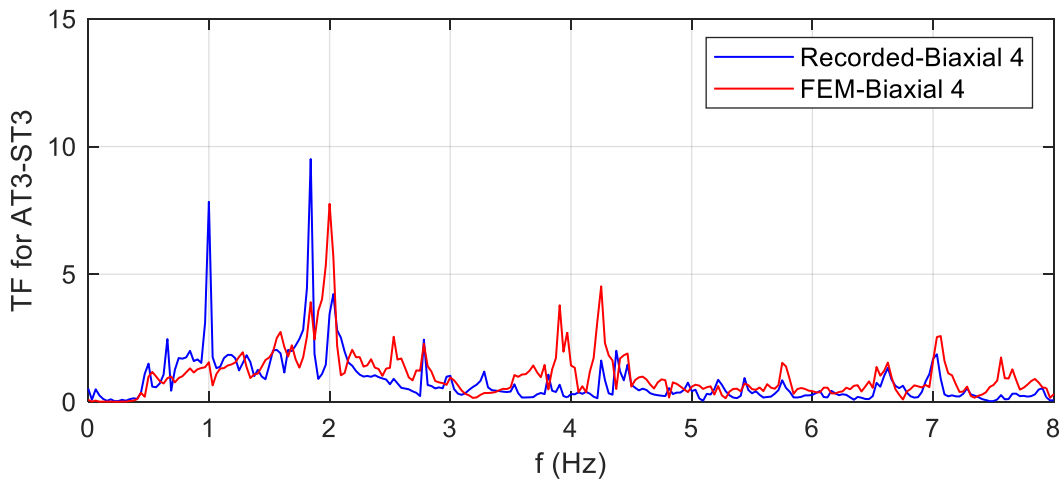
Figure 3.29. A Comparison Between Transfer Function of Recorded Acceleration Response vs. the FE Model Response for AT3-ST3 Pair (Biaxial 4 Motion)
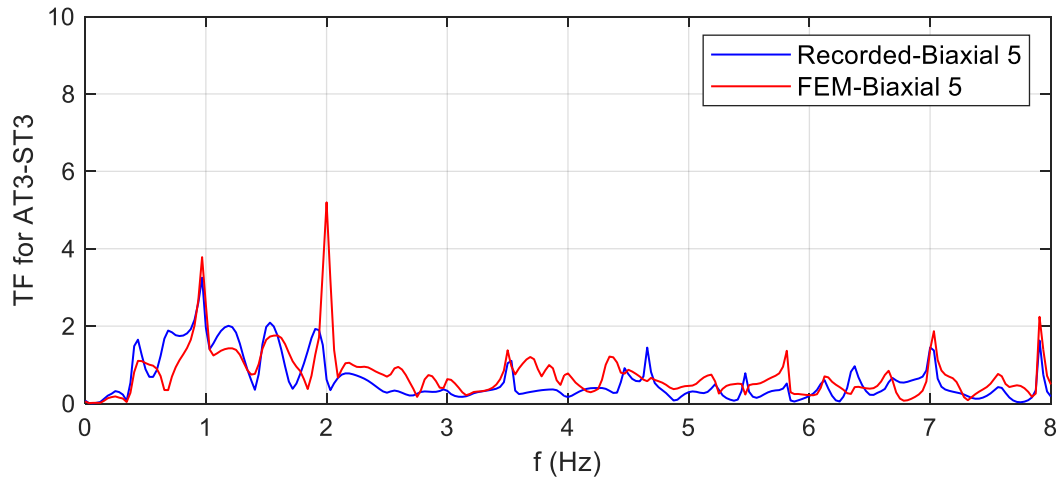
Figure 3.30. A Comparison Between Transfer Function of Recorded Acceleration Response vs. the FE Model Response for AT3-ST3 Pair (Biaxial 5 Motion)
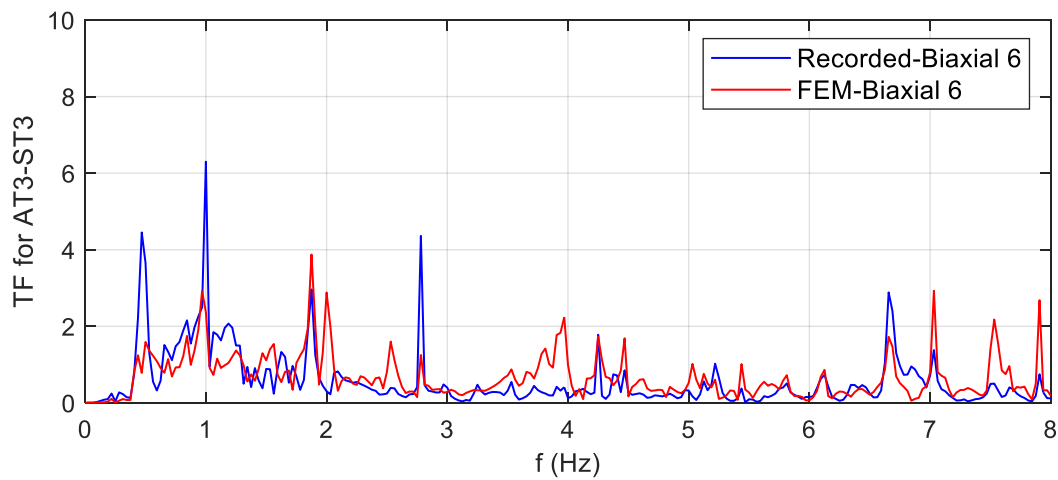
Figure 3.31. A Comparison Between Transfer Function of Recorded Acceleration Response vs. the FE Model Response for AT3-ST3 Pair (Biaxial 6 Motion)
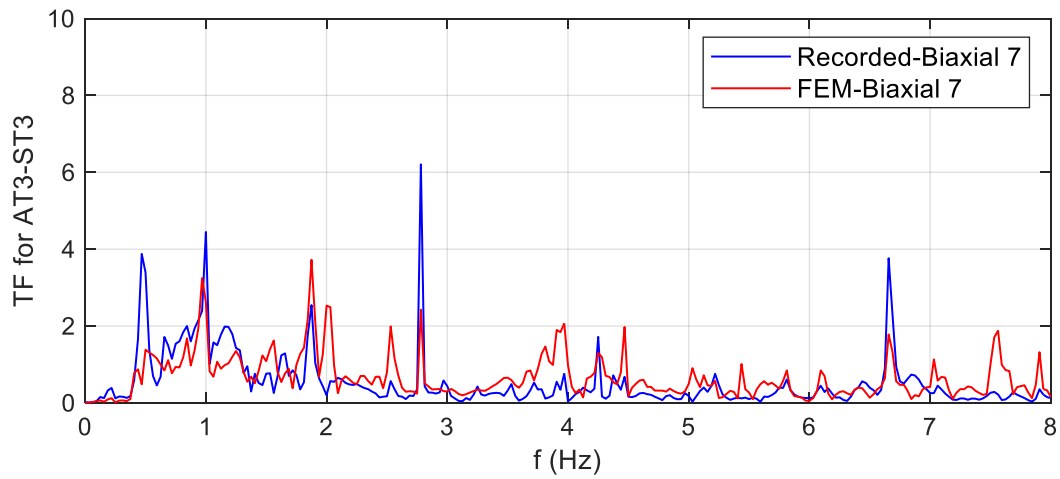
Figure 3.32. A Comparison Between Transfer Function of Recorded Acceleration Response vs. the FE Model Response for AT3-ST3 Pair (Biaxial 7 Motion)
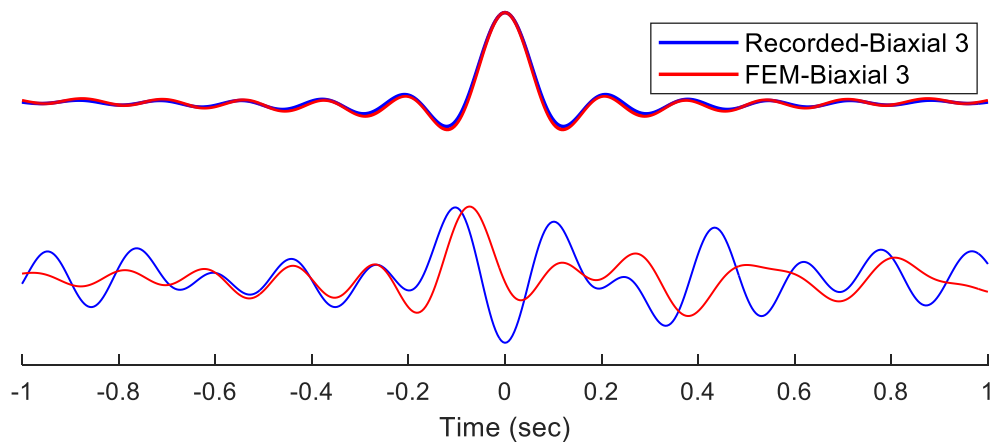
Figure 3.33. A Comparison Between Impulse Response of Recorded Acceleration Response vs. the FE Model Response for AT3-ST3 Pair (Biaxial 3 Motion)
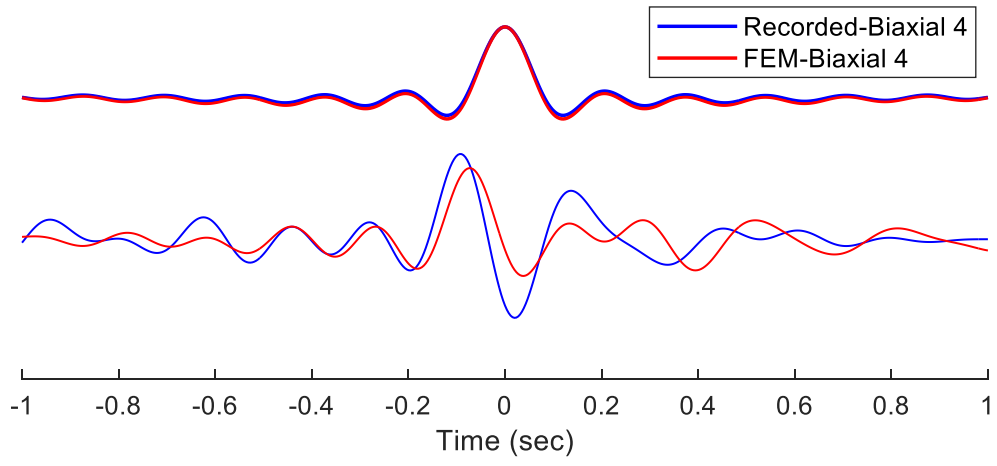
Figure 3.34. A Comparison Between Impulse Response of Recorded Acceleration Response vs. the FE Model Response for AT3-ST3 Pair (Biaxial 4 Motion)
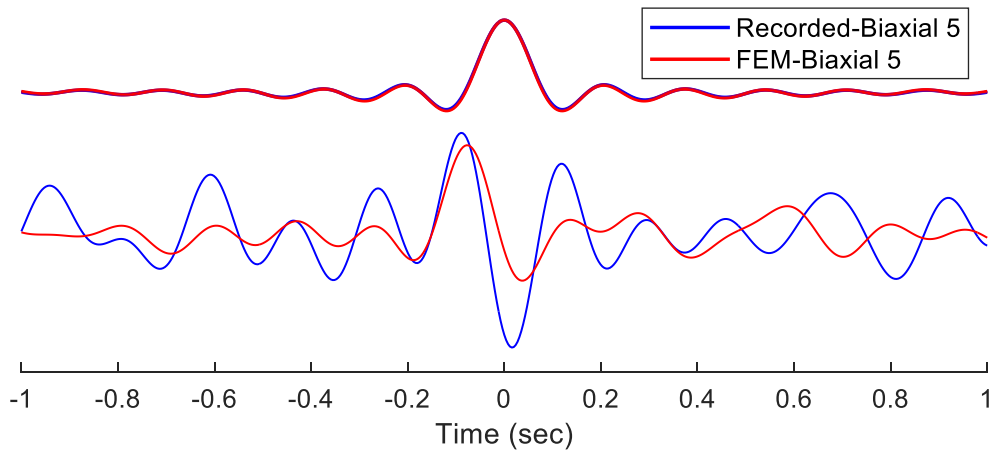
Figure 3.35. A Comparison Between Impulse Response of Recorded Acceleration Response vs. the FE Model Response for AT3-ST3 Pair (Biaxial 5 Motion)
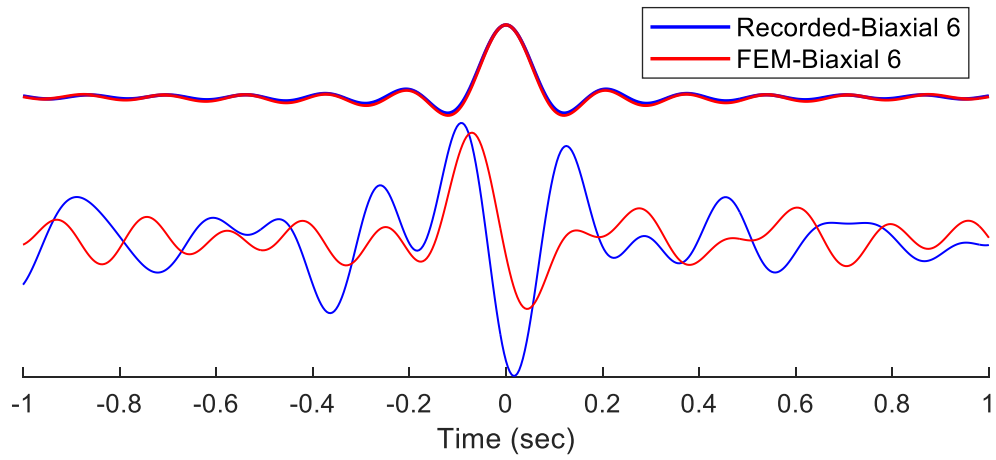
Figure 3.36. A Comparison Between Impulse Response of Recorded Acceleration Response vs. the FE Model Response for AT3-ST3 Pair (Biaxial 6 Motion)
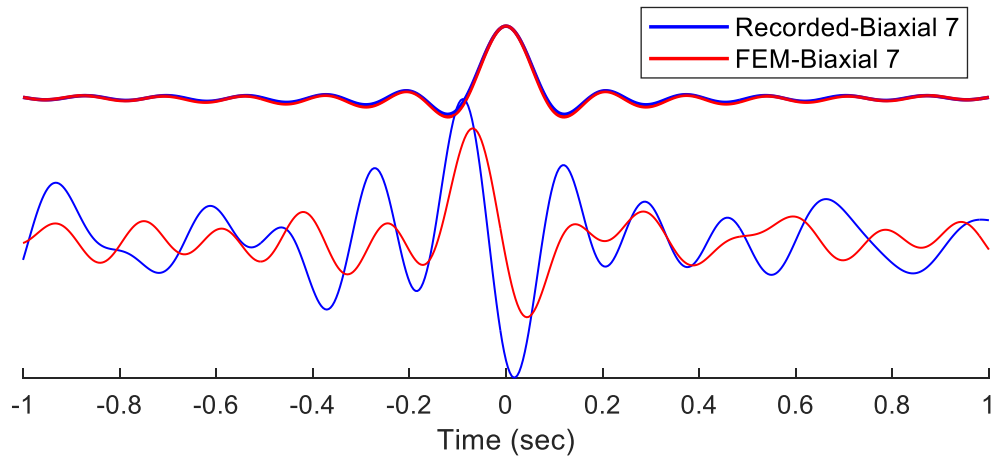
Figure 3.37. A Comparison Between Impulse Response of Recorded Acceleration Response vs. the FE Model Response for AT3-ST3 Pair (Biaxial 7 Motion)

4. Damage Detection Using the Wave Method and a Uniform Timoshenko Beam Model

In this section, we apply our waveform inversion algorithm, as discussed in Section 2, for identification, damage detection, and localization of the shake-table-tested bridge. We present wave velocities for the identified Timoshenko beam (TB) model for all damage states and compare the trends in the trends in velocities to infer damage in the columns. The results are then compared with on-site damage surveys to evaluate the method's capability. Further, we perform a similar damage detection process on our finite element model (FEM), which serves as a convenient alternative case study to further assess the capabilities and limitations of our method.

4.1 Results for the Shake-Table Tested Bridge

In this study, we introduce two wave passage scenarios to identify the bridge and possibly detect the damage location and its severity. The first wave passage scenario is the wave propagating from a shake table to the top of the columns that are seated on it. In this wave passage scenario, if the source is considered at the top, virtually, the wave will propagate from the top to the bottom of the columns. We will then model the pair of columns in each bent as a cantilever beam with inverted support (i.e., source at top). Scenario one (WP1) aims to detect damage quantity and location among the three bents. Figure 4.1 illustrates wave passages for this scenario.

The second wave passage scenario is the wave propagating starting from the middle of the span to top of the nearest columns, and then to the shake table supporting the columns. Figure 4.2 shows the second wave passage scenario (WP2). A challenge with the second scenario is that a sensor at the middle of a span results in similar velocities for two adjacent bents, given an identical base excitation at the supports. For example, given an identical base excitation at bent 1 and bent 2 (i.e., ST1 and ST2), a passage from sensor AT6 to either of these bents (see Figure 4.2) will result in identical results (i.e., AT6-ST1 and AT6-ST2 will be indistinguishable). Our analyses showed that this scenario could detect overall damage in the bridge, but cannot detect its location. Therefore, in this study, we did not find the WP2 a plausible damage localization approach.

A third wave passage scenario (WP3) could be considered such that the waves propagate through the bridge deck only, so that the scenario makes use of AT sensors at the deck only (i.e., no use of base excitation). It is noteworthy that the deck is always designed to remain elastic, and sole reliance on phase velocity of waves propagating horizontally in the deck was determined an insufficient damage indicator. Hence, here, we place emphasis on the first wave passage scenario (Figure 4.1), which includes individual pairs of columns and is unique for each bent. As discussed, the WP1 requires sensors at or near the top and bottom of each bent. For future bridge instrumentation, we recommend the deck-level channels be placed near or at the top of the columns. In addition, recorded response at the foundation level (e.g., at least one sensor at a foundation for short span bridges) is essential for detecting and possibly localizing bridge damage.
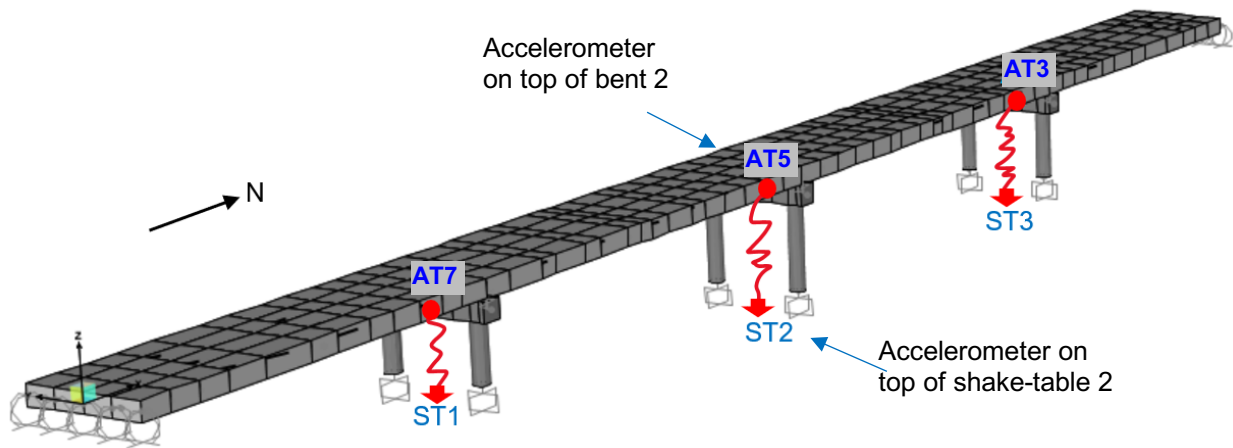
Figure 4.1. Wave Passage 1 (WP1) Through the Columns at each Bent. This was used here.
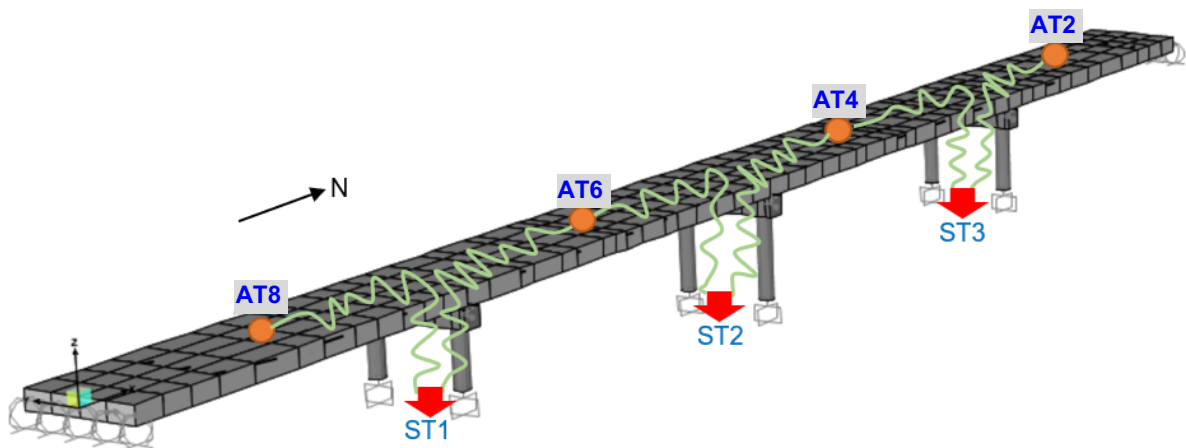
Figure 4.2. The Wave Passage 2 (WP2) Illustration

The waveform inversion algorithm was employed to identify a uniform TB model by fitting it into the case-study bridge's recorded response during the seven biaxial shakings (i.e., seven damage states). Input parameters required for the identification algorithm include a pair of acceleration time series at each bent of the bridge, e.g., AT3-ST3, which are the accelerometers located on the top and bottom of bent 3. Other inputs to the algorithm include the fitting frequency bands, dimensions of the TB model representing the columns, and mass density of the TB as well as its damping ratio.

As discussed in Section 2, a nonlinear least-square algorithm was used to minimize the objective function (i.e., IRFs fitting error). We performed the identification for a range of initial values to avoid early convergence to a local minimum which may not be the best fitted TB model. We identify the longitudinal (c_L) and shear (c_S) wave velocities as well as the normalized root-mean-square error (NRMSE) for the fit. The error represents the second norm of difference between the TB model and observed IRFs over the fitting interval, and it serves as a proxy for measuring goodness of fit and choosing the best fitted TB for a particular bent. This process is carried out for a range of damping values from 0.004 to 0.12 with 0.004 increments, which have a unit of seconds and are related to dimensionless viscous damping ratio by $\varsigma \approx \omega\mu / 2$ (Rahmani and Todorovska, 2020). The identification results including the fitting errors for all damping values are compared, and damping resulting in the minimum NRMSE is picked as the *optimal* damping for the TB model. Therefore, damping ratios were a variant across seven damage states and were identified by trials. Figure 4.3 shows the trends in values of NRMSE of the fits versus TB model's damping ratios for all seven damage states (i.e., biaxial base excitations) for bent 3 of the bridge (sensor pair AT3-ST3). Generally, the optimal damping values (indicated by arrows on Figure 4.3) increase as the amplitude of the motion increases. This is consistent with the increased energy dissipation due to additional damage by larger motions. During smaller motions (e.g., biaxials 1 through 3), the optimal damping values are smaller, as the bridge response remains predominantly elastic.

Figures 4.4 to 4.7 illustrate fitted impulse response functions (IRFs) for bent 3 during biaxial motions 2, 4, and 7 (plots on the right), respectively. Figures 4.8 through 4.12 show similar plots but for bents 1 and 2. The plots show that TB model's pulse shapes (e.g., the amplitude and shift) agree very well with the observed IRF pulses. While the waveform inversion algorithm primarily aims to achieve the best fits of the pulses in the IRFs, a comparison of transfer functions (TFs) of deck-to-base response (plots on the left) at the bents (i.e., wave passages) provides a secondary verification that the fitted TB model makes physical sense and is thus an appropriate representation of the bridge's state. The frequency band for these fits was set to 0 to 10 Hz, which includes at least two translational modes of vibration.

Table 4.1 presents results for identified TB models for the WP1 (the first wave passage scenario) and for all biaxial motions. The first column of the table indicates the bent number and the pair of accelerometers used for analysis. The second column lists damage states for the bridge starting from biaxial 1 motion (undamaged state) to biaxial 7 motion (severe damage state). The next group of three columns shows the initial values and final estimated values for c_L, c_S, and the normalized error. The last column of the table presents percentage of reduction in c_S with respect to that of the undamaged state, biaxial 1. The observed trends in these values are discussed in Section 4.7.
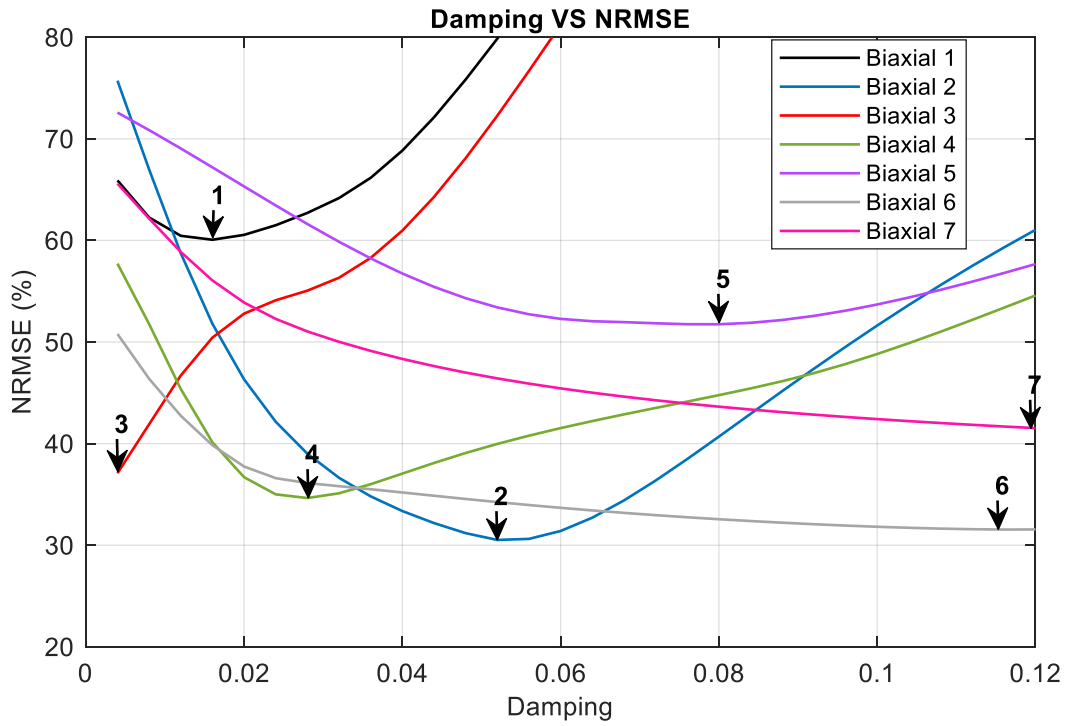
Figure 4.3. Damping vs. NRMSE for the Seven Biaxial Motions at the Bent 3 (Pair AT3-ST3) for Actual Tested Bridge
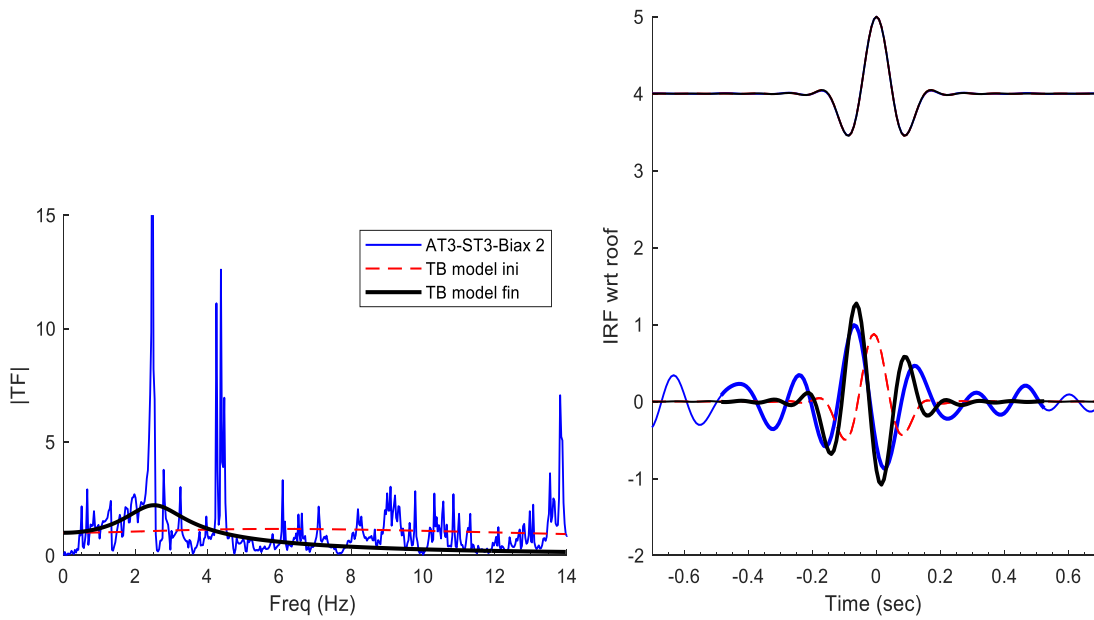
Figure 4.4. Uniform Timoshenko Beam Fitting Result for AT3-ST3 Biaxial 2, Actual Bridge Scenario 1
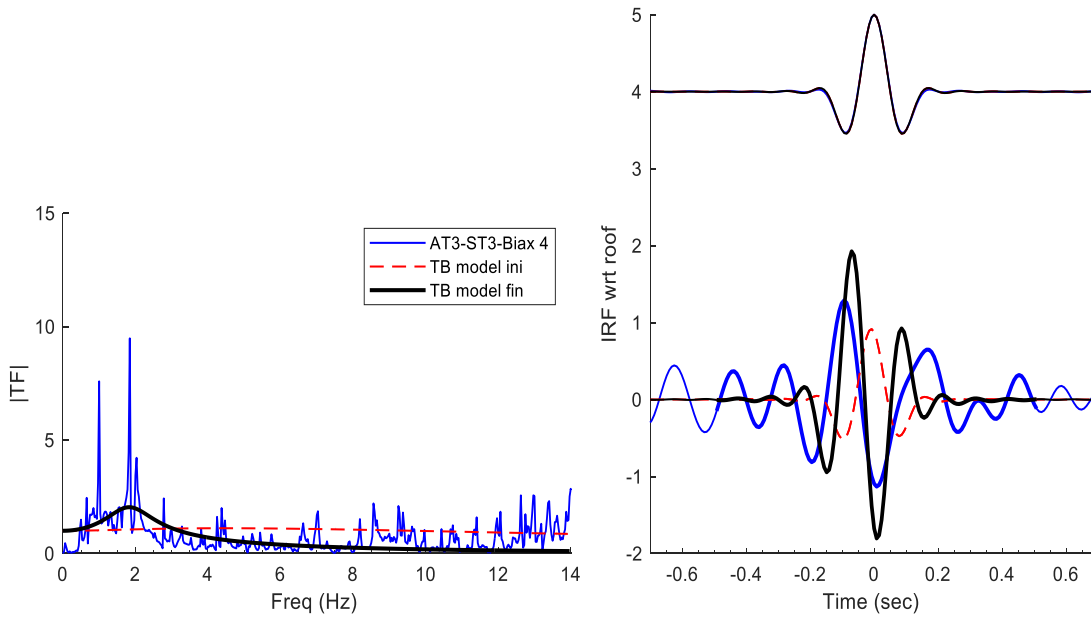
Figure 4.5. Uniform Timoshenko Beam Fitting Result for AT3-ST3 Biaxial 4, Actual
Bridge Scenario 1

Figure 4.6. Uniform Timoshenko Beam Fitting Result for AT3-ST3 Biaxial 7, Actual
Bridge Scenario 1

Figure 4.7. Uniform Timoshenko Beam Fitting Result for AT7-ST1 Biaxial 2, Actual Bridge Scenario 1

Figure 4.8. Uniform Timoshenko Beam Fitting Result for AT7-ST1 Biaxial 4, Actual Bridge Scenario 1

Figure 4.9. Uniform Timoshenko Beam Fitting Result for AT7-ST1 Biaxial 7, Actual Bridge Scenario 1

Figure 4.10. Uniform Timoshenko Beam Fitting Result for AT5-ST2 Biaxial 2, Actual Bridge Scenario 1

Figure 4.11. Uniform Timoshenko Beam Fitting Result for AT5-ST2 Biaxial 4, Actual Bridge Scenario 1
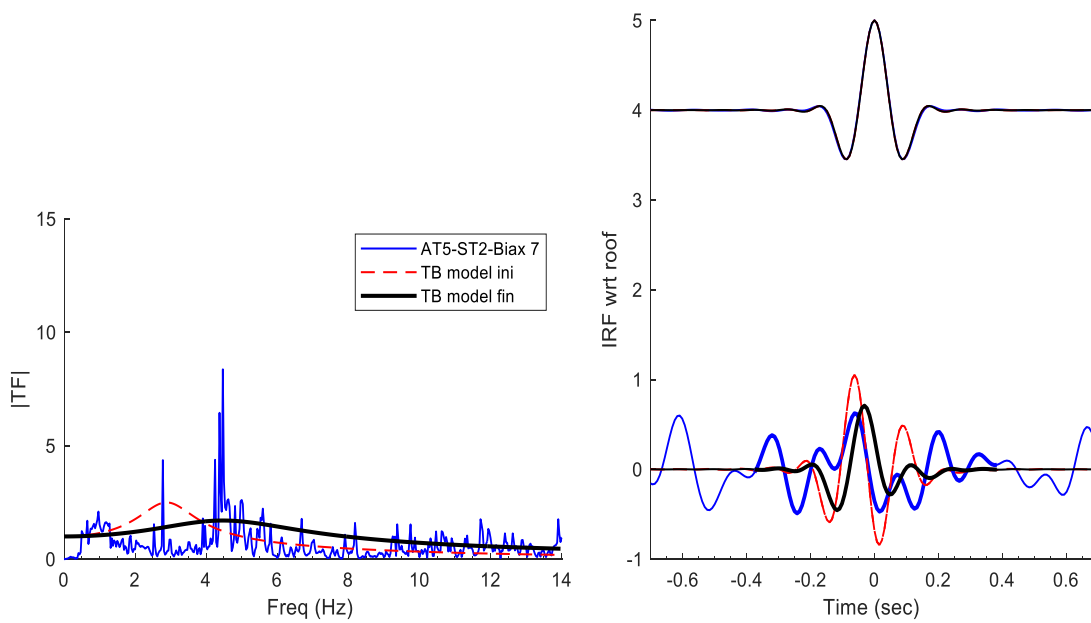
Figure 4.12. Uniform Timoshenko Beam Fitting Result for AT5-ST2 Biaxial 7, Actual Bridge Scenario 1

Table 4.1. Identified Percentage Change of Longitudinal Velocity c_L on the TB Fitting for Actual Bridge Data

	Damage State	μ	Initial Values			Estimated Final Values			c_S change w.r.t. biaxial 1 (%)
			c_S (m/s)	c_L (m/s)	RMS error (%)	c_S (m/s)	c_L (m/s)	RMS error (%)	
BENT 1 AT7-ST1	Biaxial 1	0.02	10	145	476.2	20.5	70.2	101.1	0
	Biaxial 2	0.03	70	25	579.7	22.5	56.1	116.5	-10
	Biaxial 3	0.04	70	50	123	18.3	49.7	71.3	11
	Biaxial 4	0.06	70	25	579.7	16.7	48.7	95	19
	Biaxial 5	0.16	70	50	123	15.8	38.9	112.1	23
	Biaxial 6	0.16	45	35	119.1	11.5	28.7	105.3	44
	Biaxial 7	0.16	60	135	123.1	11.3	30	121.7	45
BENT 2 AT5-ST2	Biaxial 1	0.005	140	55	86.3	45.7	55.5	84.2	0
	Biaxial 2	0.004	75	75	136.7	42.6	77.9	132.5	7
	Biaxial 3	0.01	145	70	119.6	42.9	79.4	102.4	6
	Biaxial 4	0.01	80	45	162.8	41.1	89.4	116.7	10
	Biaxial 5	0.015	40	65	91.3	58	54.6	87.1	-27
	Biaxial 6	0.03	25	135	139.9	41.1	154.3	121.8	10
	Biaxial 7	0.03	25	95	120	40	319.6	114.8	12
BENT 3 AT3-ST3	Biaxial 1	0.04	65	50	147.7	20.4	55.4	114.7	0
	Biaxial 2	0.04	115	105	137.9	23.7	53.8	63.4	-16
	Biaxial 3	0.04	95	150	144.9	21.4	54.1	90.5	-5
	Biaxial 4	0.06	115	105	137.9	16.6	51.3	101.2	19
	Biaxial 5	0.16	95	150	144.9	14.6	26.5	100.1	28
	Biaxial 6	0.16	120	80	135.8	12	25.8	79.6	41
	Biaxial 7	0.16	70	110	131.4	11.2	27	78	45

Figures 4.13 to 4.16 show trends in the identified shear c_S and longitudinal c_L wave velocities for all three bents (i.e., wave passages). The vertical axes present the value of velocities, or their percentage reduction compared to the first biaxial motion. The horizontal axes show the damage states indicated by the biaxial excitations. The identified c_S and c_L are constant properties of the fitted TB model for each of the bents and for each biaxial motion. The trends in c_S show a clear reduction in the bridge's shear wave velocity in the transverse direction as the motion intensity increases. Comparing the trends for the three bents reveals that the reduction in velocity is largest

for bent 1 (the shortest bent) and smallest for bent 2 (the longest bent). These trends are consistent with the observed degree of damage in these bents, which will be discussed in the next sections.

In addition, we found the trends in c_L to be relatively erratic, not showing a clear indication of damage in the columns. The c_L presents compressional wave velocity along the columns. Given the heavy deck and its superimposed heavy block loads, the gravity load bearing system (i.e., columns) is designed to be very stiff in compression. The pressure exerted from the superstructure on the columns increases their longitudinal stiffness (e.g., compressional stiffness in a post-tensioned column). This makes the compressional deformation (along the height of columns) very small. Moreover, a closer look at the behavior of the bridge under shake-table excitation shows that the deck oscillates primarily in lateral directions, similar to a shear deformation in the slabs of a shear building (e.g., a moment-resisting frame). Therefore, the compressional stiffness of the columns is expected to experience only a small change during the shakings, causing the trends in the c_L to remain relatively chaotic. Instead, we find the c_S to be a viable damage indicator as the nonlinear hinge formations at the top and bottom of the columns directly reduce the lateral (i.e., shear) stiffness of the columns, which is reflected in the identified c_S.

The first transverse mode of vibration during biaxial 1 and biaxial 2 excitations (i.e., the undamaged state of the bridge) was located at about 2.4 Hz. Fitting results for bent 2 (Figures 4.10 to 4.12), the least damaged columns of the bridge, show that our best fits of TB models are affected significantly by the higher-frequency mode at about 4.5 Hz. In other words, the pulse shape in the IRFs is impacted by this large high-frequency mode, and thus, our identification result for bent 2 becomes fully biased towards this second apparent mode. The TF plots in Figures 4.10 through 4.12 show a good match at the second mode between the TB model and the observed response. This is in contrast with our results for bents 1 and 3, for which the fundamental transverse mode (at ~2.4Hz) is dominant in the analysis passband (0–10 Hz) and affects the IRF pulses. Hence, the results presented in this section show noticeable difference between bent 2 and the other bents. The higher mode's effect on the identified velocities and their trends is further discussed in the following section. Moreover, in the following sections of this report, we present similar analysis results and trends for our finite element model (FEM). We also review and summarize on-site damage surveys for the bridge and provide a damage rating for each bent following each biaxial shaking. Next, we discuss agreement of trends in the c_S with the extent of actual damage in the bridge and their sequence of occurrence.
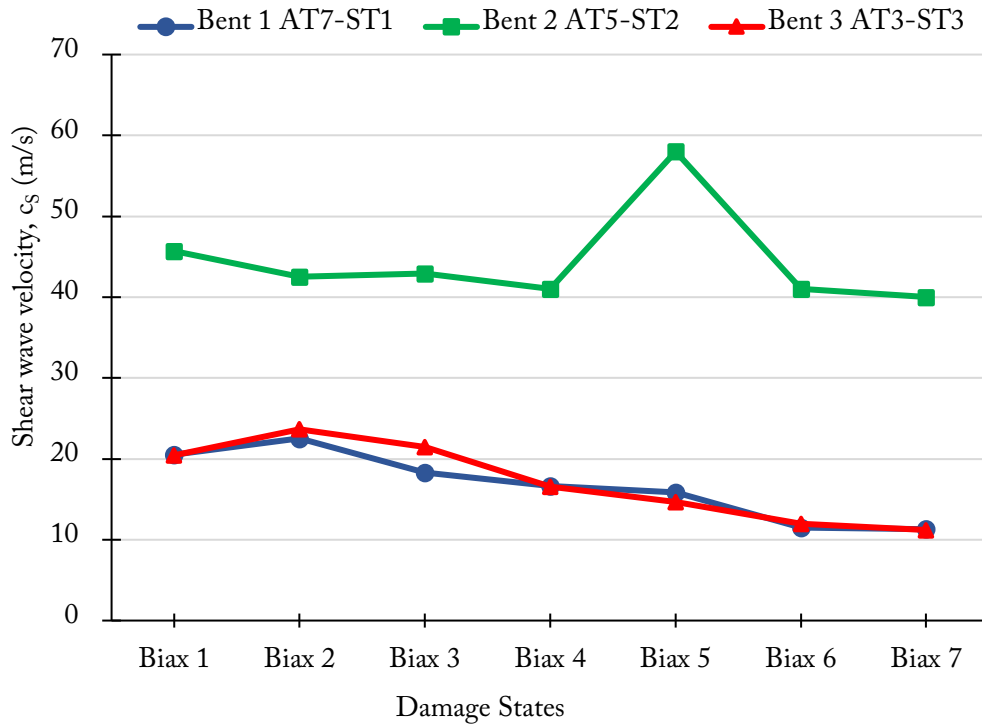
Figure 4.13. Shear Wave Velocity, c_S, for Wave Passage 1 for Actual Tested Bridge
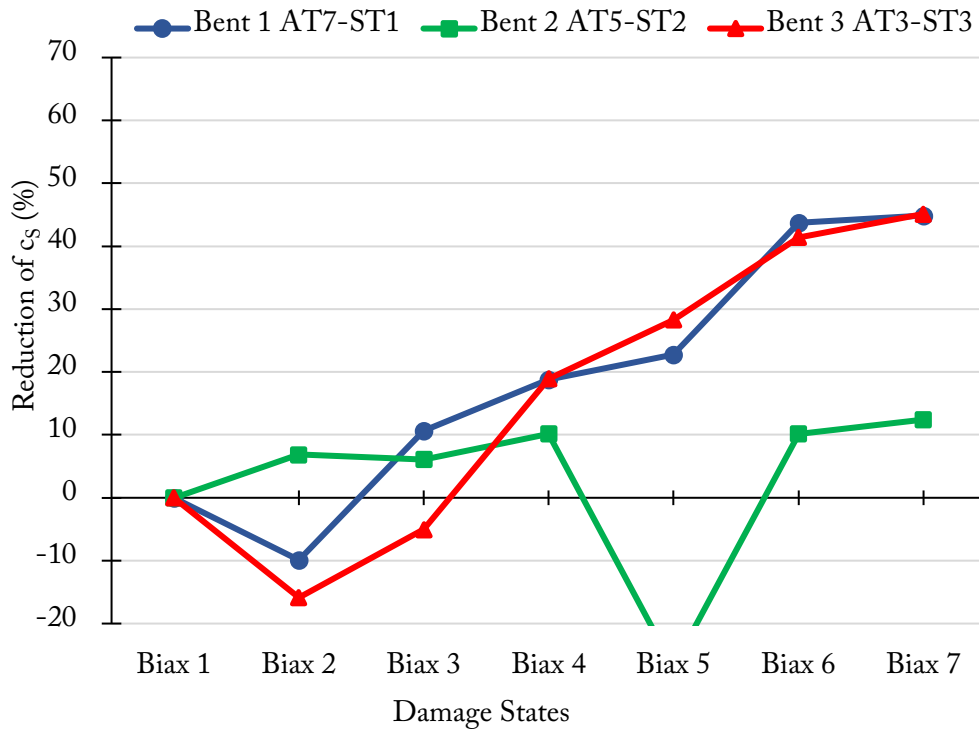
Figure 4.14. Percentage of Reduction in Shear Wave Velocity, c_S, for Actual Bridge
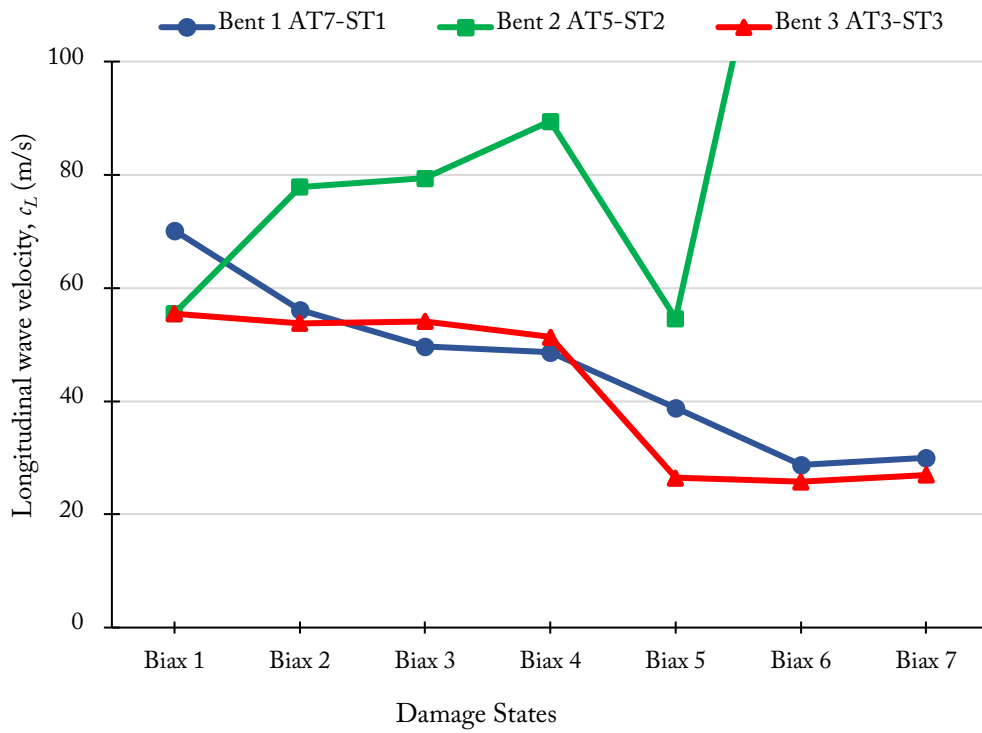
Figure 4.15. Longitudinal Wave Velocity, c_L, for Actual Tested Bridge
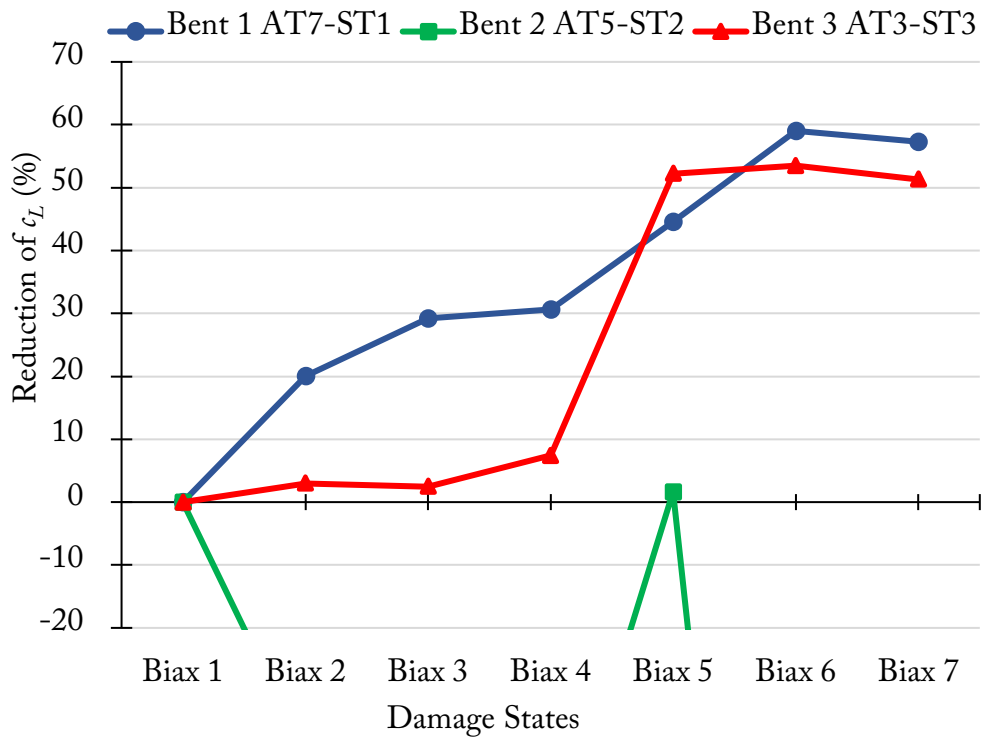
Figure 4.16. Percentage of Change in Longitudinal Wave Velocity c_L for Actual Tested Bridge

4.2 Uniform TB Model Fitted into the Nonlinear Finite Element Model (FEM) of the Bridge

We use transverse acceleration responses of our updated nonlinear finite element model (FEM) to perform damage detection and localization on this desktop model. The nonlinear response and the hinge behavior of this FEM is known to us via SAP2000 software (see Section 3). Hence, it can serve as a performance test for our wave-based damage detection method. Table 4.2 presents the results of identified velocities by fitting a TB model into the FEM. This table includes similar columns to those for the actual recorded response (Table 4.1). As discussed in the previous section, our focus remains on monitoring the trends in identified c_S for each bridge's bent (i.e., wave passage). Figures 4.17 to 4.25 show fitted IRFs and the corresponding TFs for the FEM and the TB model for biaxials 2, 4, and 7 for all bents.

The frequency band for the analysis is 0 to 10 Hz for all damage states. The fact that the bridge softens through larger biaxial motions causes the modal frequencies to shift to lower values (i.e., modal periods increase). Therefore, note that the constant frequency band used in this analysis may include one or more modes of vibration for larger biaxial motions compared to smaller amplitude motions. On the other hand, a larger frequency band will reduce the width of the propagating pulses, allowing the causal and acausal propagating pulses to split from each other. Such a split is necessary for our waveform inversion algorithm to perform. The figures show that the goodness of the fits is very good. A similar observation was made for bent 2, where the second transverse vibration mode significantly influenced the IRF shapes and hence the fitting results for this bent. This observation verifies that what was observed for the actual bridge response was a physical phenomenon, not an artifact, and that the true transverse response at the middle of the bridge contains coupled modes of vibration at 4.5 Hz, overshadowing the first mode at this location. In the following sections, we examine the affected result at bent 2 and determine whether it can be utilized for damage detection purposes.

Figures 4.26 to 4.29 show the values and trends in the identified c_S and c_L for all three of the FEM's bents. The velocities are plotted versus the biaxial motions to indicate the state of damage in the FEM. Similar to the results for the actual bridge, the trends of c_S for FEM suggest that bents 1 and 3 soften significantly as the base acceleration increases. This is in line with trends observed for the actual bridge response.

Table 4.2. Identified Longitudinal (c_L) and Shear (c_S) Velocities of the Best Fitted TB Model into FEM Response, Fitting Frequency Band of 0–10 Hz

	Damage State	μ (sec)	Initial Values			Estimated Final Values			c_S change w.r.t. biaxial 1 (%)
			c_S (m/s)	c_L (m/s)	RMS error (%)	c_S (m/s)	c_L (m/s)	RMS Error (%)	
BENT 1 AT7-ST1	Biaxial 1	0.02	105	140	85.9	78.5	48.2	66.9	0
	Biaxial 2	0.03	90	115	68.4	62.8	39.3	52.3	20
	Biaxial 3	0.04	65	95	134.5	52.8	31.4	57.8	33
	Biaxial 4	0.06	50	120	104.6	20.1	120.1	50.7	74
	Biaxial 5	0.16	10	80	94	14.3	116.1	49.4	82
	Biaxial 6	0.16	105	140	107.8	20.2	18.4	53.1	74
	Biaxial 7	0.16	75	50	99.3	21.5	17.5	45	73
BENT 2 AT5-ST2	Biaxial 1	0.005	65	90	85.9	85.6	55.2	21.3	0
	Biaxial 2	0.004	40	65	68.4	58.6	48.8	66.4	32
	Biaxial 3	0.01	130	145	134.5	133.1	7.88	30.5	-55
	Biaxial 4	0.01	115	140	133.8	84.1	45.8	51.9	2
	Biaxial 5	0.015	90	45	22.7	103.4	43.6	20.5	-21
	Biaxial 6	0.03	135	20	1810.8	68.5	40	22.6	20
	Biaxial 7	0.03	80	45	43.1	60.4	39.4	27.6	29
BENT 3 AT3-ST3	Biaxial 1	0.04	145	120	185.3	29.9	71.3	110.9	0
	Biaxial 2	0.04	115	105	137.9	23.7	53.8	63.4	21
	Biaxial 3	0.04	25	120	31	23.1	73.5	23.2	23
	Biaxial 4	0.06	20	105	29.4	20.2	64.3	29	32
	Biaxial 5	0.16	35	105	113.4	13	32.7	32.8	56
	Biaxial 6	0.16	10	95	74	12.3	166.3	27.1	59
	Biaxial 7	0.16	40	150	106.9	12.1	63.7	32.5	60
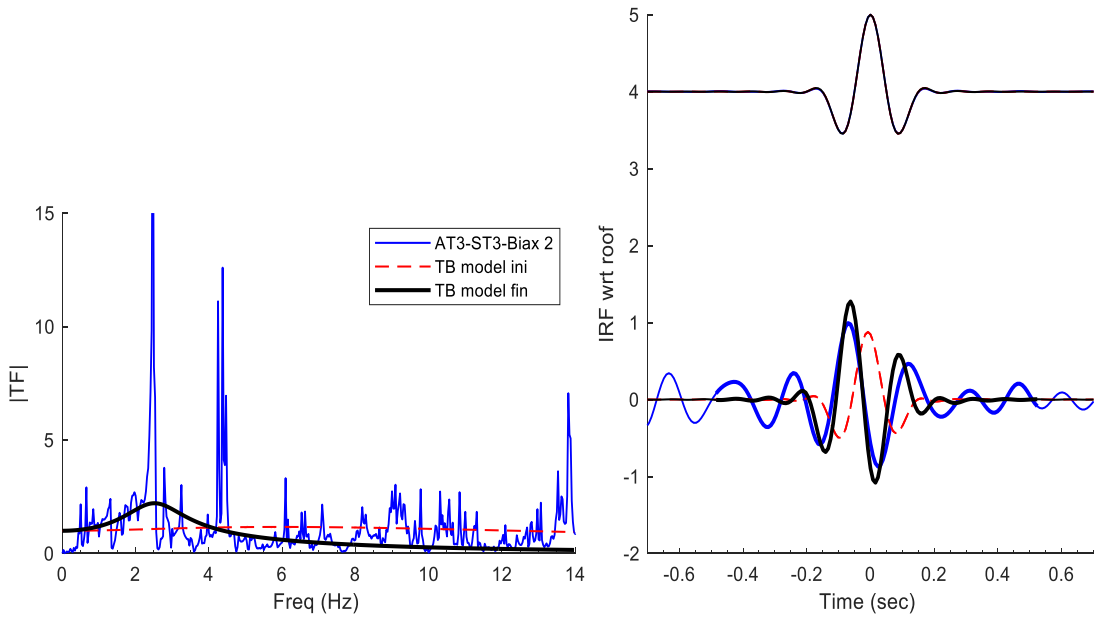
Figure 4.17. Uniform Timoshenko Beam Fitting Result for AT3-ST3 Biaxial 2, from FEM Response
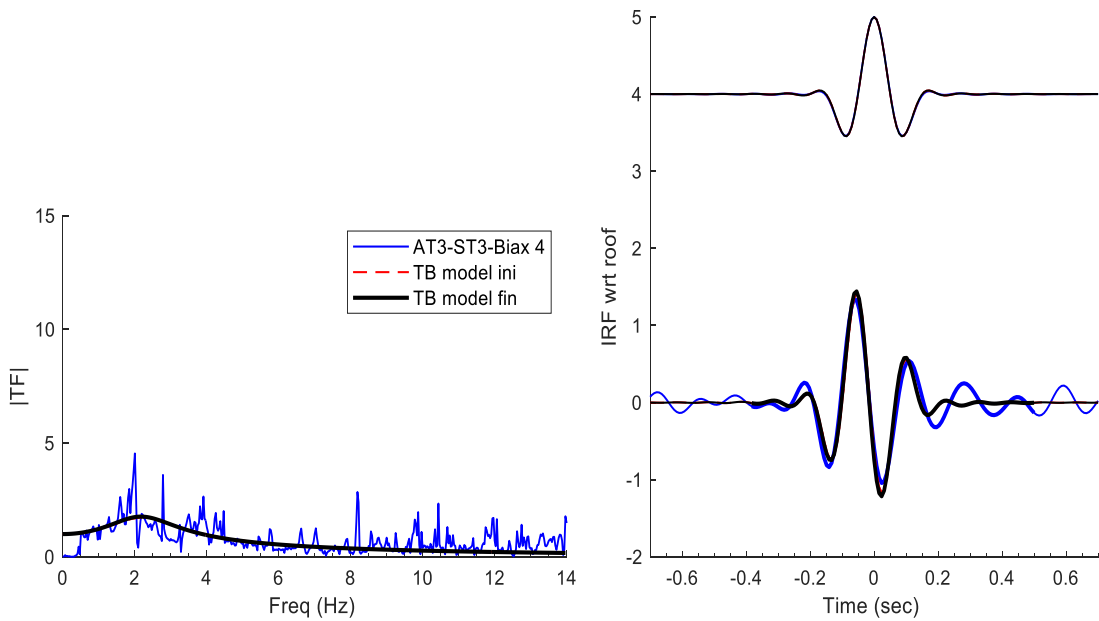
Figure 4.18. Uniform Timoshenko Beam Fitting Result for AT3-ST3 Biaxial 4, from FEM Response
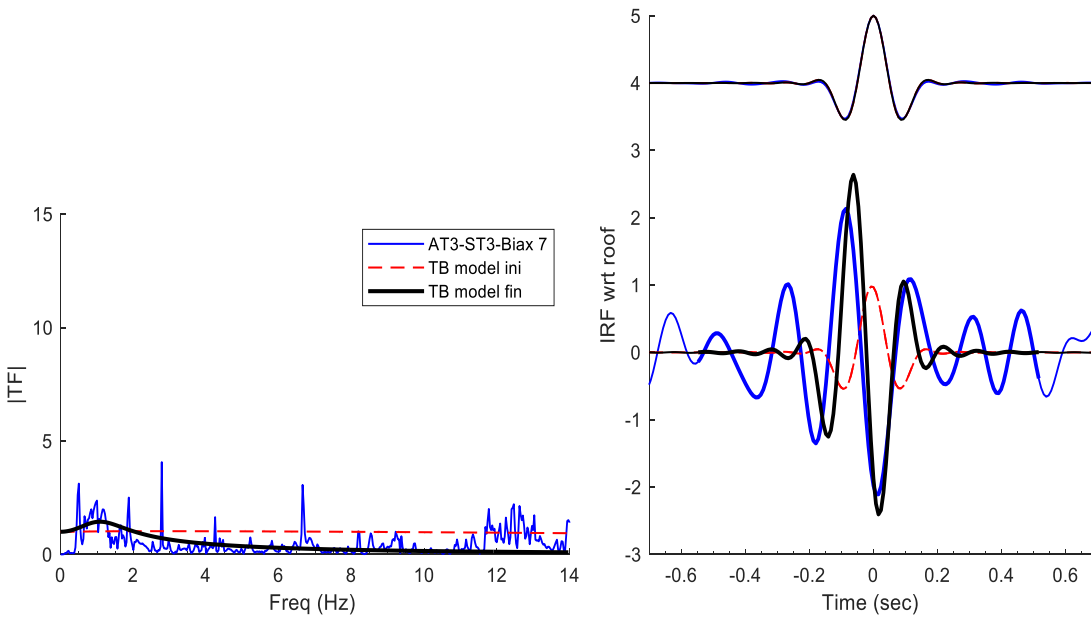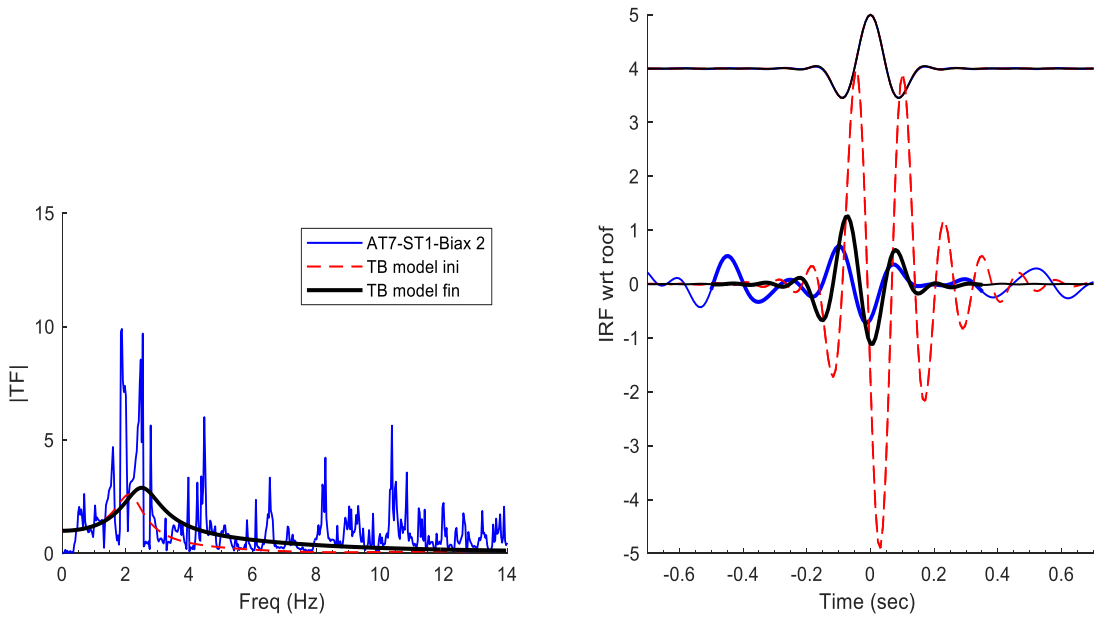
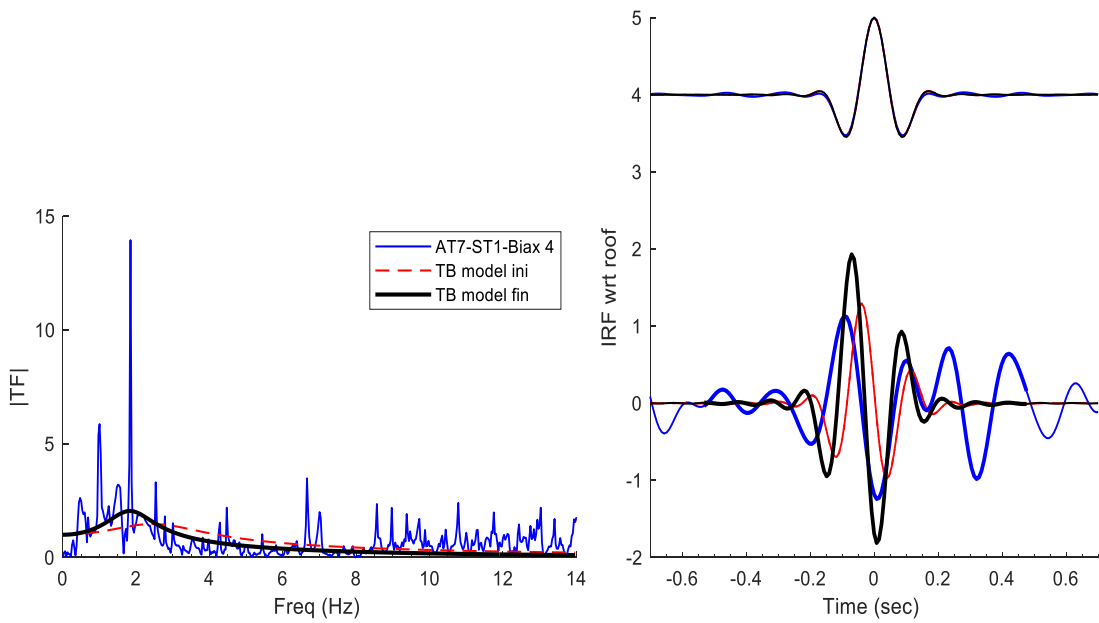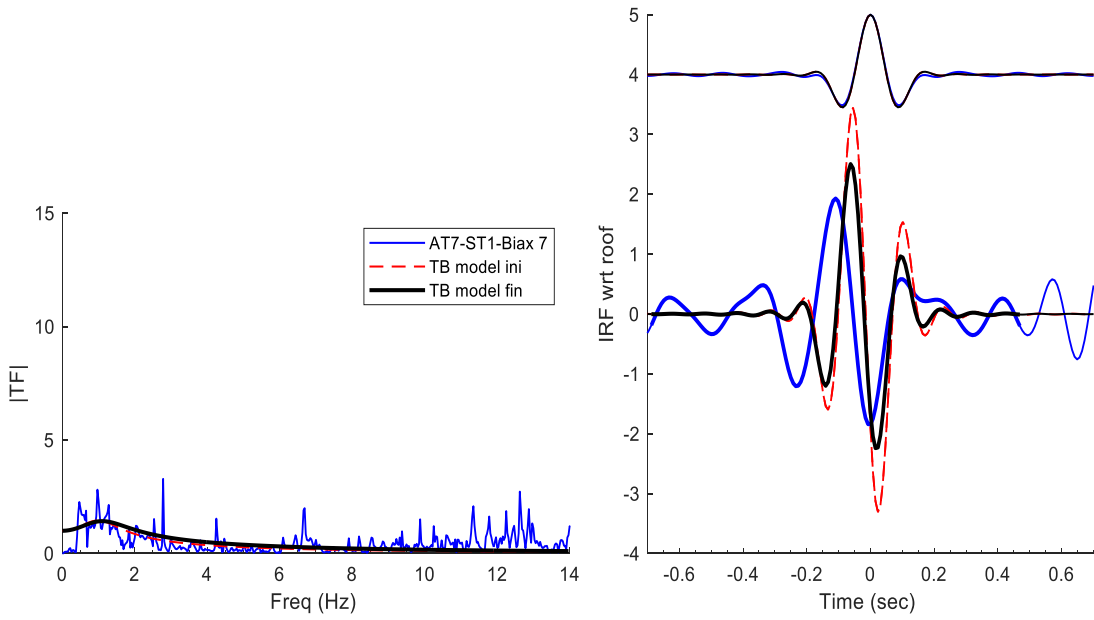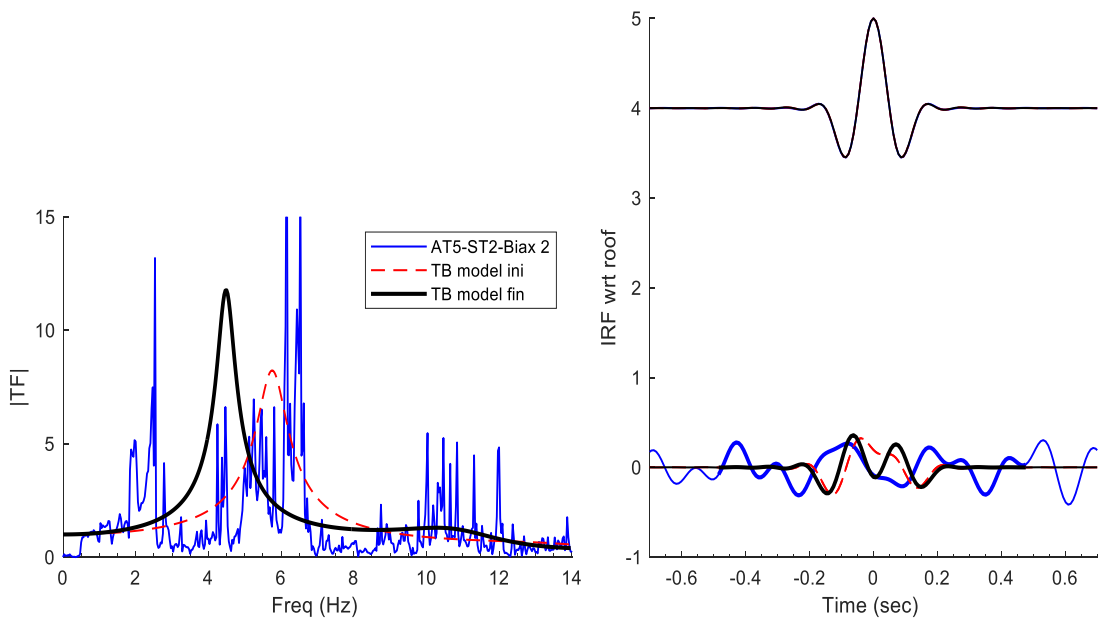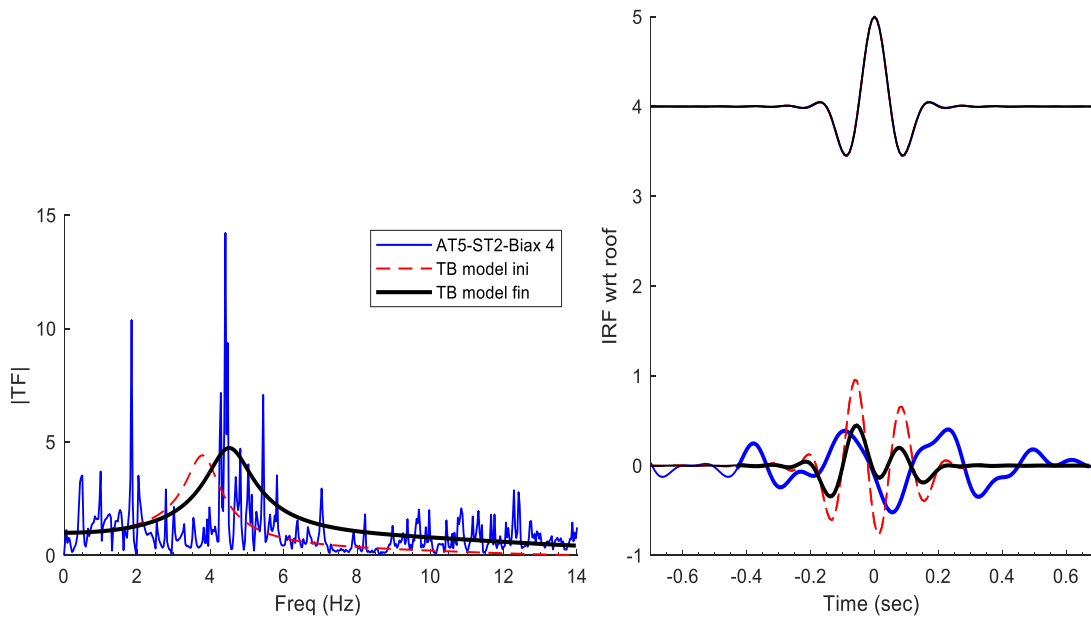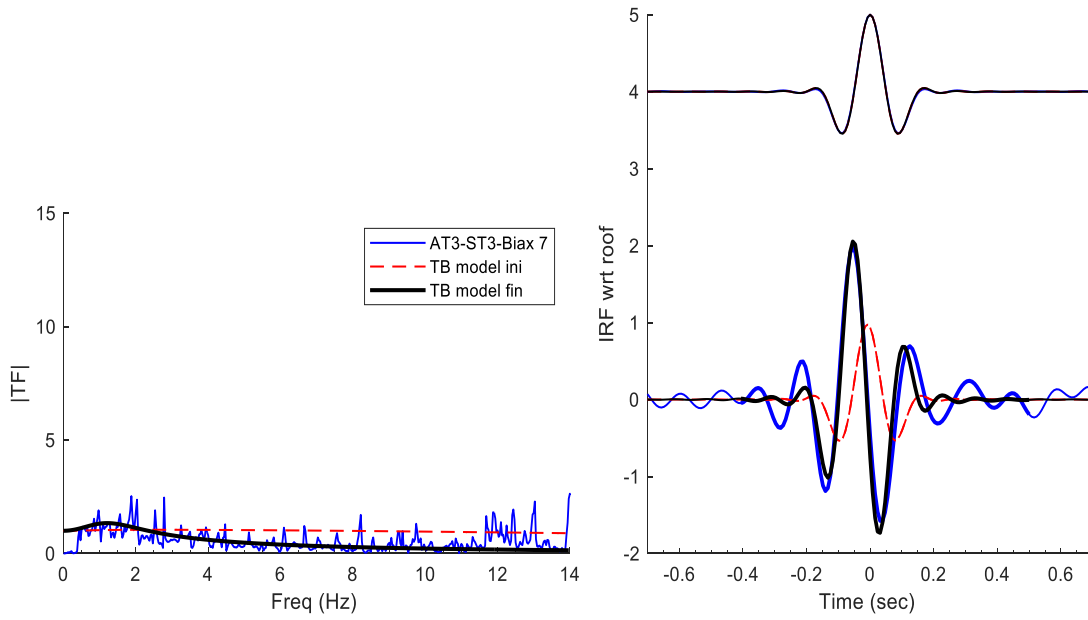Figure 4.19. Uniform Timoshenko Beam Fitting Result for AT3-ST3 biaxial 7, from FEM Response
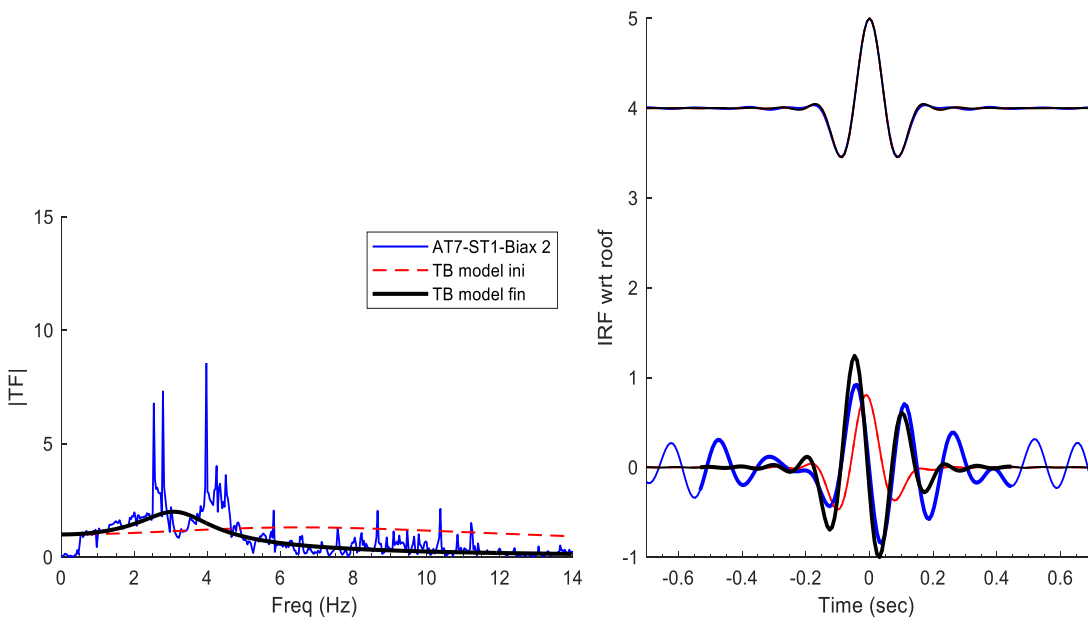
Figure 4.20. Uniform Timoshenko Beam Fitting Result for AT7-ST1 biaxial 2, from FEM Response
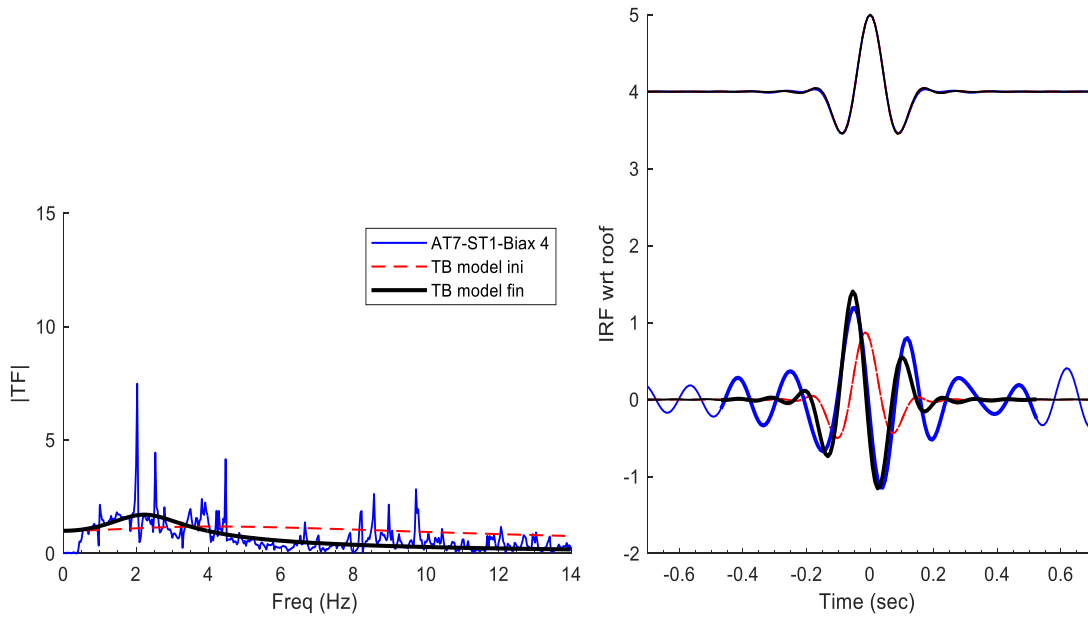
Figure 4.21. Uniform Timoshenko Beam Fitting Result for AT7-ST1 biaxial 4, from FEM Response
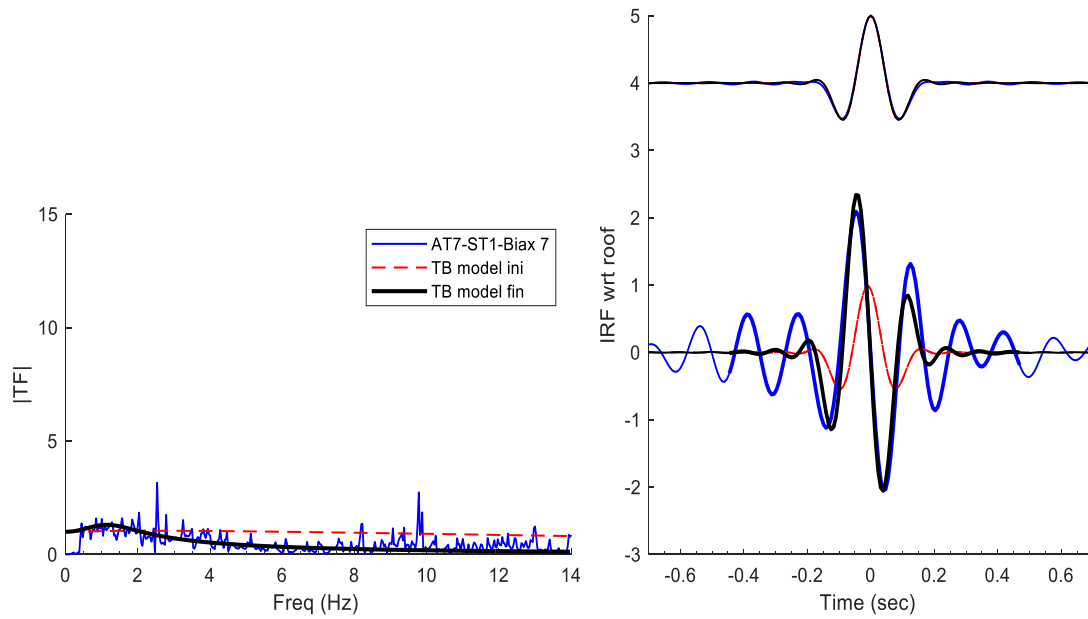
Figure 4.22. Uniform Timoshenko Beam Fitting Result for AT7-ST1 biaxial 7, from FEM Response
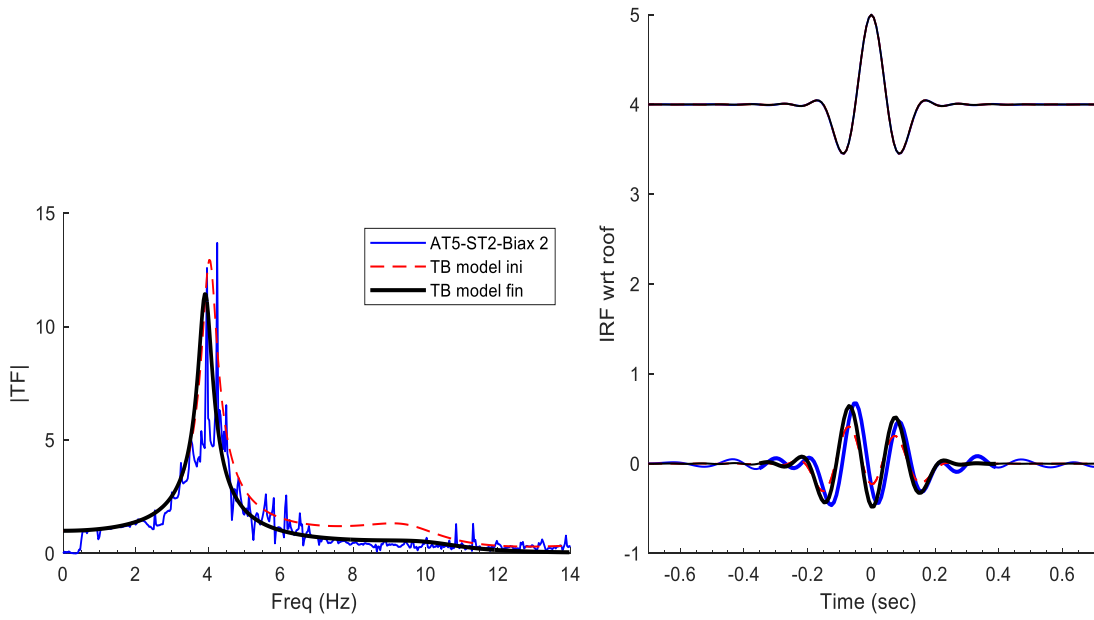
Figure 4.23. Uniform Timoshenko Beam Fitting Result for AT5-ST2 biaxial 2, from FEM Response
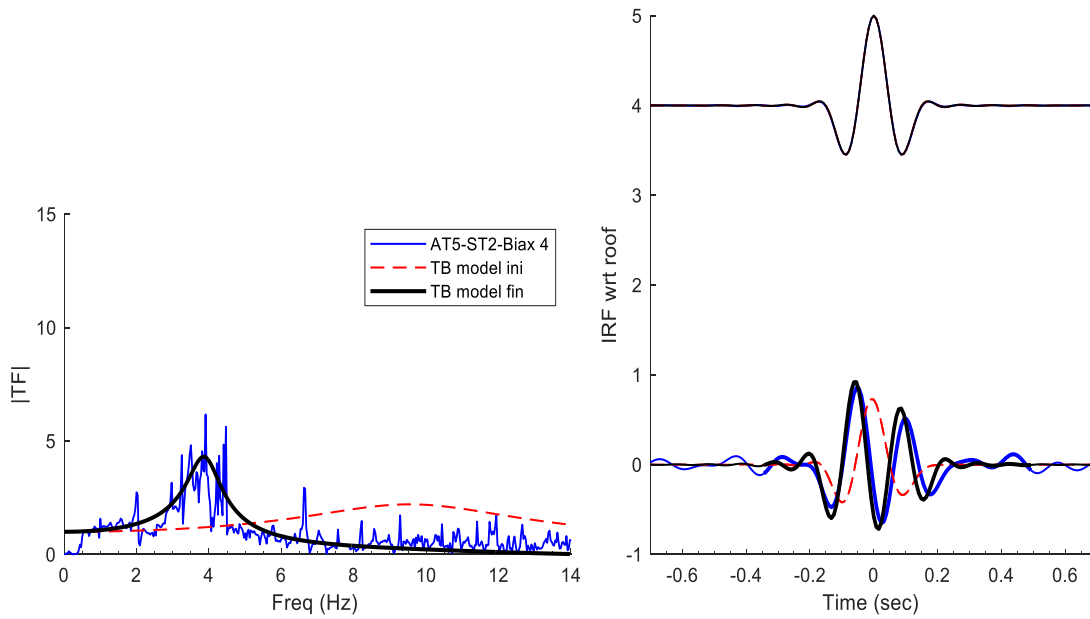
Figure 4.24. Uniform Timoshenko Beam Fitting Result for AT5-ST2 biaxial 4, from FEM Response
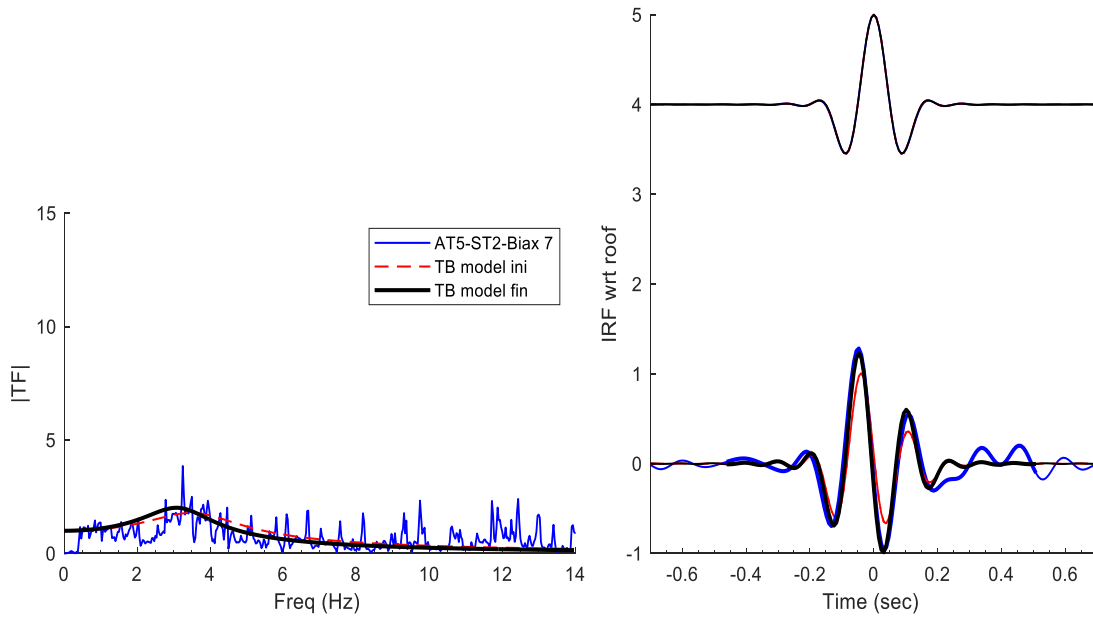
Figure 4.25. Uniform Timoshenko Beam Fitting Result for AT5-ST2 biaxial 7, from FEM Response
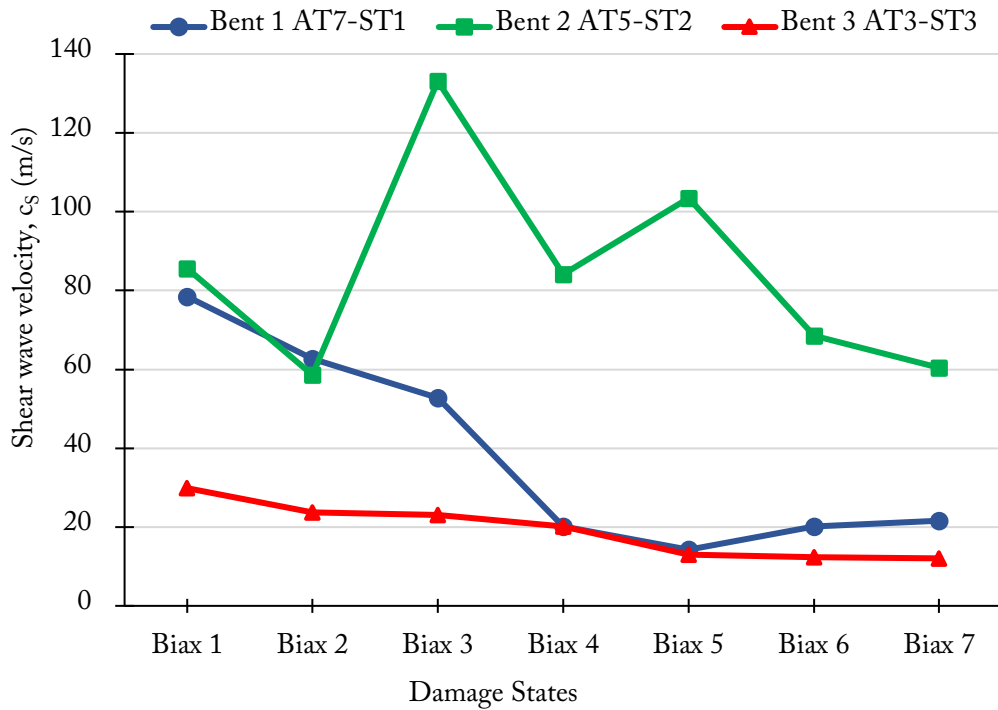
Figure 4.26. Shear Wave Velocity, c_S, from FEM Response
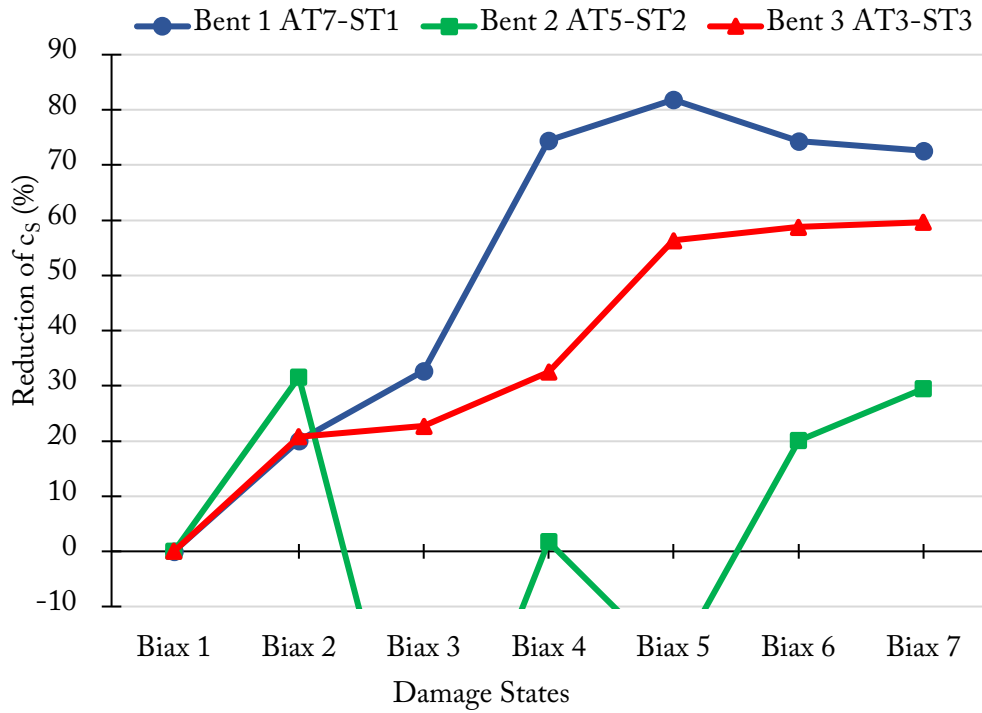
Figure 4.27. Percentage of Change in Shear Wave Velocity from FEM Response
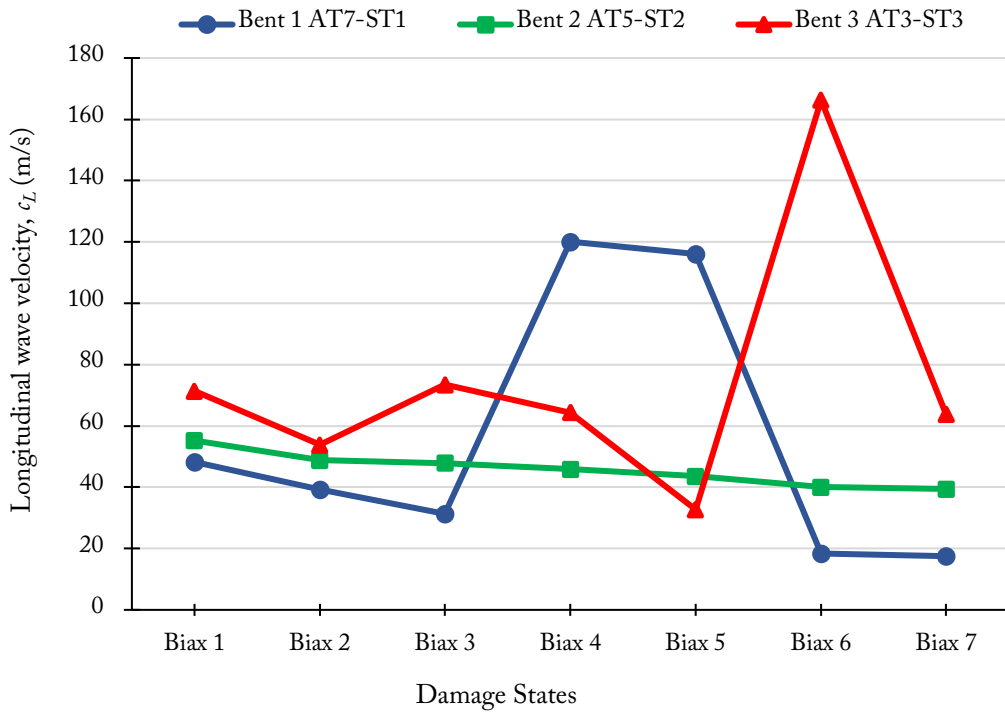
Figure 4.28. Longitudinal Wave Velocity, c_L, from FEM Response
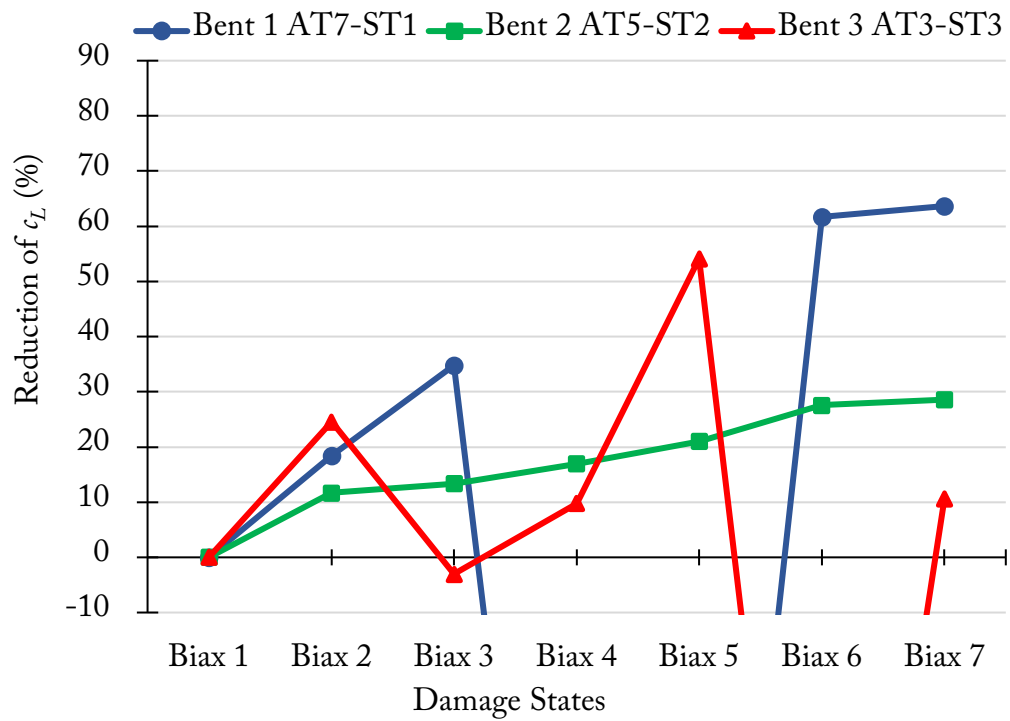
Figure 4.29. Percentage of Change in Longitudinal Wave Velocity from FEM Response

4.3 A Summary of Damage in the Bridge Columns After Each Biaxial Excitation

The bridge testing protocol included uniaxial, white noises, and biaxial excitations at the bridge base. Seven biaxial motions with increasing amplitudes, resembling two orthogonal components of realistic earthquake motions, were utilized in this study. After each shaking, the bridge columns sustained an increasing degree of damage. A detailed damage survey of the columns was performed by the original project team (Nelson et al., 2007) where they documented crack length and width, concrete spalling, vertical rebar exposure, rebar buckling, and more. The comprehensive damage survey was performed for all six columns at three bents (i.e., three wave passages in this study). The sequence and extent of damage is crucial information for evaluating our method's capability to detect the onset of damage in each pair of columns (i.e., each bent) and assessing the method's accuracy in localizing the most and least severe damage in the piers.

In this study, we collected damage information from the original report on the bridge by Nelson et al. (2007) and reorganized them in Appendix A of this report. There are three tables in Appendix A that provide detailed information about the history of damage in each of the bridge's columns during seven biaxial shakings. Table A1 presents cracked widths observed after each biaxial motion for each bent (east and west columns) and for the top and bottom zones of the columns. Table A2 presents information about concrete spalling at the columns including the size and description. Table A3 shows a survey of vertical and lateral rebars in the columns, providing information on the number of exposed rebars and whether any buckling was observed. In addition to on-site visual inspections, the bridge's maximum and residual drift could be considered an alternative damage indicator, which could be obtained from displacement response at the deck.

Visual damage inspection showed that bent 1, comprising the shortest columns of the bridge, sustained the most severe damage at the end of the testing sequence. This was expected, owing to its larger stiffness and its larger shear force apportionment relative to other bents. Both columns in bent 1 showed flexural cracks immediately after the biaxial 1 excitation at the top and bottom hinge zones. These cracks spread widely to the entire height of the columns as larger biaxial motions excited the bridge. In bent 1, the cover concrete at the top and bottom of the columns starts spalling after biaxial 3, especially on the east column. As the biaxial motions become stronger, increasing cover concretes are spalled, such that almost all of them came off at the bottom of bent 1 after biaxial 7. Moreover, after biaxial 7, all longitudinal and most lateral rebars were exposed, and all rebars on the east column buckled, the most severe damage observed among the three bents.

Bent 2, located at the center of the bridge, is the tallest bent which sustained the least amount of damage due to its smaller shear demand. Very minor flexural cracks were barely visible until the biaxial 3 motion, becoming visible after biaxial 4. The cover concretes started spalling after biaxial 5, especially on the bottom of the columns, where about half of the cover concrete spalled at the bottom of bent 2 after biaxial 7. Rebar condition at bent 2 looked healthy with only a few lateral rebars exposed, and no vertical rebar damage or buckling was visible. Therefore, bent 2 was the least damaged bent during the entire test. Bent 3, located on the north side of the bridge, had

a height in between bents 1 and 2. Its behavior during various shakings was also in between what was observed at bents 1 and 2. In fact, concrete spalling in bent 3 looked more like bent 1 and was significant. However, compared to bent 1, rebar damage was less severe, i.e., fewer exposed rebars and no rebar buckling were observed at bent 3.

A convenient approach for processing the observed damages in the bridge is to characterize them as either no damage, light damage, moderate damage, or severe damage. Caltrans Seismic Design Criteria (2010) as well as Vosooghi and Saiidi (2010) provide a set of metrics by which damage can be characterized or rated for bridge columns. Table 4.3 shows damage states and criteria following these references.

Tables 4.4 to 4.6 present a brief description of all the observed damage to concrete and rebars of the columns during all seven biaxial motions. Each table is dedicated to damage observed at the columns of a bent of the bridge. It also presents the maximum drift ratio during each motion intensity and provides a damage characterization according to the criteria noted in Table 4.3. To illustrate the actual progression of damage at the columns, we provide a color-coded rendering of the bridge for each biaxial motion shown in Figure 4.30. There are five colors for five damage states described in Table 4.3. The color-coding helps interpret the results obtained for the velocity reductions. Figure 4.31 shows pictures of damage progression in bent 1 during biaxials 1, 4, and 7 motions. The extent of damage (concrete spalling, rebar exposure, and rebar buckling) is evident in the pictures (Nelson et al., 2007).

Table 4.3. Column Damage States

Damage State Designations per Vosooghi and Saiidi (2010)	Maximum Drift Ratio (%)	Residual Drift Ratio (%)	Longitudinal Steel Strain (με)	Damage State per Caltrans (2013)	Service Level per Caltrans (2013)
DS1: Flexural cracks	1.4–2.3	0–0.1	6,582–17,899	Minimal damage	Limited service-days
DS2: First spalling and shear cracks	2.4–3.5	0.1–0.5	14,524–28,839	Minimal damage	Limited service-days
DS3: Extensive cracks and spalling	3.3–5.4	0.2–0.8	28,174–42,373	Moderate damage	Limited service-weeks
DS4: Visible lateral and longitudinal bars	4.5–6.7	0.3–1.7	28,174–42,373	Moderate damage	Limited service-weeks
DS5: Imminent failure	5.1–9.7	0.5–2.7	31,022–59,599	Major damage	No service

Source: Per Caltrans Seismic Design Criteria V1.7 (2013) and Vosooghi and Saiidi (2010)

Table 4.4. A Detailed Damage Description for Bent 1 of the Bridge and During 7 Biaxials

	Damage State	Damage Description
Bent 1 AAT7 – ST1	Biax1:	**Observed Cracking:** East column top range 0.007 to 0.013 in.; east column bottom ~ 0.002 in.; west column top ~ 0.002 in.; west column bottom ~ 0.002 in. **Observed Spalling:** No spalling concrete in both columns top and bottom. **Rebar Yielding and Exposure:** No exposure rebar in both columns top and bottom. **Transverse Drift Ratio:** 0.7%, max. displacement in transverse direction is 10.2 mm; max. displacement in longitudinal direction is 10.2 mm. **Damage Categorization/Index:** DS – 1, minimal damage with limited service-days.
	Biax2:	**Observed Cracking:** East column top range 0.016 to 0.025 in.; east column bottom ~ 0.002 in.; west column top ~ 0.002 in.; west column bottom ~ 0.002 in. **Observed Spalling:** No spalling concrete in both columns top and bottom **Rebar Yielding and Exposure:** No exposure rebar in both columns top and bottom. **Transverse Drift Ratio:** 1.2%, max. displacement in transverse direction is 17.8 mm; max. displacement in longitudinal direction is 24.1 mm. **Damage Categorization/Index:** DS – 1, minimal damage with limited service-days.
	Biax3:	**Observed Cracking:** East column top range 0.013 to 0.025 in.; east column bottom range 0.003 to 0.025 in.; west column top range 0.001 to 0.002 in.; west column bottom range 0.003 to 0.013 in. **Observed Spalling:** East column top has flake spall in north and south side with max. 1 in. spall height; east column bottom has half-circular spall with max. 1.5 in. spall height; west column top has no spalling; west column bottom has flake in west side with 0.125 in. spall height. **Rebar Yielding and Exposure:** No exposure rebar in both columns top and bottom. **Transverse Drift Ratio:** 1.5%, max. displacement in transverse direction is 22.9 mm; max. displacement in longitudinal direction is 68.6 mm. **Damage Categorization/Index:** DS – 2, minor damage with initial sign of spalling, limited service-days.
	Biax4:	**Observed Cracking:** East column top range 0.013 to 0.025 in.; east column bottom range 0.005 to 0.01 in.; west column top range 0.002 to 0.005 in.; west column bottom range 0.02 to 0.03 in. **Observed Spalling:** East column top has min. flake spall with max. 1 in. spall height; east column bottom has min. flake spall with max. 1.5 in. spall height; west column top has no spall; west column bottom has min. flake spall with 0.125 in. spall height. **Rebar Yielding and Exposure:** East column top has 1 lateral rebar exposed on west side; east column bottom has 2 lateral rebars exposed on north side; west column top has no exposed rebar; west column bottom has 2 lateral rebars exposed on north side. No yielding or buckling. **Transverse Drift Ratio:** 2.7%, max. displacement in transverse direction is 40.6 mm; max. displacement in longitudinal direction is 68.6 mm. **Damage Categorization/Index:** DS – 3, moderate damage with limited service-weeks.

	Damage State	Damage Description
	Biax5:	**Observed Cracking:** East column top range 0.013 to 0.025 in.; east column bottom range 0.02 to 0.03 in.; west column top range 0.007 to 0.05 in.; west column bottom range 0.02 to 0.03 in. **Observed Spalling:** East column top has flake spall with max. 3 in. spall height; east column bottom has half-circular spall with max. 4 in. spall height; west column top has flake spall with max. 4 in. spall height; west column bottom has ¾ circular spall with 3 in. spall height. **Rebar Yielding and Exposure:** East column top has 3 lateral rebars exposed; east column bottom has 2 lateral rebars exposed; west column top has no exposed rebar; west column bottom has 6 lateral rebars exposed. No yielding or buckling. **Transverse Drift Ratio:** 3.9%, max. displacement in transverse direction is 59.9 mm; max. displacement in longitudinal direction is 91.2 mm. **Damage Categorization/Index:** DS – 4, moderate damage with limited service weeks.
	Biax6:	**Observed Cracking:** East column top range 0.02 to 0.03 in.; east column bottom range 0.03 to 0.035 in.; west column top range 0.01 to 0.03 in.; west column bottom range 0.03 to 0.035 in. **Observed Spalling:** East column top has one-quarter-circular spall with max. 3 in. spall height; east column bottom has three-quarters-circular spall with max. 4 in. spall height; west column top has flake spall with max. 3.5 in. spall height; west column bottom has ¾ to full circle spall with 3.5 in. spall height. **Rebar Yielding and Exposure:** East column top has 4 lateral rebars and 3 longitudinal rebars exposed on west side; east column bottom has 11 lateral rebars and 10 longitudinal rebars exposed on all sides except north side; west column top has 1 lateral rebar exposed on east side; west column bottom has 9 lateral rebars and 9 longitudinal exposure on all sides except east side. Minor yielding was expected. **Transverse Drift Ratio:** 7.6%, max. displacement in transverse direction is 115.8 mm; max. displacement in longitudinal direction is 101.1 mm. **Damage Categorization/Index:** DS – 5, major damage with no service.
	Biax7:	**Observed Cracking:** severe cracking. **Observed Spalling:** East column top has ½ circular spall with max. 6 in. spall height; east column bottom has full circular spall with max. 8 in. spall height; west column top has flake to ¼ circular spall with max. 5 in. spall height; west column bottom has full circular spall with 9 in. spall height. **Rebar Yielding and Exposure:** East column top has 9 lateral rebars and 3 longitudinal rebars exposed, no buckling. East column bottom has 18 lateral rebars and 28 longitudinal rebars exposed, 2 longitudinal & 1 latitudinal bar fracture and 5 longitudinal buckled in north side, 3 longitudinal & 1 latitudinal bar fracture and 4 longitudinal buckled in east side, all bars buckled in south and west side. West column top has 5 lateral rebars and 3 longitudinal rebars exposed; west column bottom has 22 lateral rebars and 27 longitudinal rebars exposed, and 3 longitudinal rebar buckled in. **Transverse Drift Ratio:** maximum 8.8%. **Damage Categorization/Index:** DS – 5, major damage with no service.

Source: Information presented in this table is extracted and organized from Nelson et al. (2007). *Note:* Damage categorizations come from Vosooghi and Saiidi (2010) and the Caltrans Design Criteria (2013).

Table 4.5. A Detailed Damage Description for Bent 2 of the Bridge and During 7 Biaxials

	Damage State	Damage Description
Bent 2 **AT5 – ST2**	Biax1:	**Observed Cracking:** East column top has 0.002 in.; east column bottom has 0.002 in.; west column top has 0.002 in.; west column bottom has 0.002 in. crack width. **Observed Spalling:** No spalling concrete in both columns top and bottom. **Rebar Yielding and Exposure:** No exposure rebar in both columns top and bottom. **Transverse Drift Ratio:** 0.4%, max. displacement in transverse direction is 7.6 mm; max. displacement in longitudinal direction is 10.2 mm. **Damage Categorization/Index:** DS – 1, minimal damage with limited service-days per [2, 3].
	Biax2:	**Observed Cracking:** East column top has 0.002 in.; east column bottom has 0.002 in.; west column top has 0.002 in.; west column bottom has 0.002 in. **Observed Spalling:** No spalling concrete in both columns top and bottom **Rebar Yielding and Exposure:** No exposure rebar in both columns top and bottom. **Transverse Drift Ratio:** 0.7%, max. displacement in transverse direction is 15.2 mm; max. displacement in longitudinal direction is 24.1 mm. **Damage Categorization/Index:** DS – 1, minimal damage with limited service-days per [2, 3.]
	Biax3:	**Observed Cracking:** East column top range 0.002 to 0.003 in.; east column bottom range 0.003 to 0.005 in.; west column top has 0.002 in.; west column bottom range 0.002 to 0.003 in. **Observed Spalling:** No spalling concrete in both columns top and bottom. **Rebar Yielding and Exposure:** No exposure rebar in both columns top and bottom. **Transverse Drift Ratio:** 0.9%, max. displacement in transverse direction is 19.1 mm; max. displacement in longitudinal direction is 40.6 mm. **Damage Categorization/Index:** DS – 1, minimal damage with limited service-days per [2, 3.]
	Biax4:	**Observed Cracking:** East column top range 0.002 to 0.005 in.; east column bottom range 0.003 to 0.007 in.; west column top range 0.002 to 0.003 in.; west column bottom range 0.003 to 0.01 in. **Observed Spalling:** East column top has no spalling; east column bottom has flake spall; west column top has no spall; west column bottom has flake spall. **Rebar Yielding and Exposure:** No exposure rebar in both bottoms top and bottom. **Transverse Drift Ratio:** 1.5%, max. displacement in transverse direction is 31 mm; max. displacement in longitudinal direction is 68.6 mm. **Damage Categorization/Index:** DS – 2, minor damage with first onset of flake spalling. Limited service-days per [2, 3].

	Damage State	Damage Description
	Biax5:	**Observed Cracking:** East column top range 0.005 to 0.013 in.; east column bottom range 0.005 to 0.009 in.; west column top range 0.003 to 0.01 in.; west column bottom range 0.005 to 0.01 in. **Observed Spalling:** East column top has no spall; east column bottom has spall with max. 3 in. spall height on north and west side; west column top has no spall; west column bottom has spall with 2.5 in. spall height. **Rebar Yielding and Exposure:** No rebar exposure in both columns top and bottom. **Transverse Drift Ratio:** 1.8%, max. displacement in transverse direction is 39.4 mm; max. displacement in longitudinal direction is 91.2 mm. **Damage Categorization/Index:** DS – 2, minimal damage with limited service-days per [2, 3].
	Biax6:	**Observed Cracking:** East column top range 0.005 to 0.02 in.; East column bottom range 0.007 to 0.016 in.; West column top range 0.003 to 0.007 in.; West column bottom range 0.007 to 0.016 in. **Observed Spalling:** East column top has ¼ circular spall with max. 2 in. spall height in west side; east column bottom has flake to ½ circular spall with max. 5 in. spall height; west column top has flake spall; west column bottom has ¼ circular spall with max. 5 in. spall height. **Rebar Yielding and Exposure:** East column top has no rebars exposure; east column bottom has 4 lateral rebars and no longitudinal rebars exposure; west column top has no rebar exposure; west column bottom has 2 lateral rebars. No yielding or buckling. **Transverse Drift Ratio:** 2.8%, max. displacement in transverse direction is 60.2 mm; max. displacement in longitudinal direction is 101.1 mm. **Damage Categorization/Index:** DS – 3, minimal damage with limited service-weeks per [2, 3].
Bent 2 AT7 – ST1	Biax7:	**Observed Cracking:** East column top range 0.007 to 0.02 in.; east column bottom range 0.007 to 0.013 in.; west column top range 0.005 to 0.02 in.; west column bottom range 0.01 to 0.025 in. **Observed Spalling:** East column top has ¼ circular spall with max. 3 in. spall height; east column bottom has ½ circular spall with max. 5 in. spall height; west column top has flake spall; west column bottom has ½ circular spall with 6 in. spall height. **Rebar Yielding and Exposure:** East column top has no rebar exposure, no buckling; East column bottom has 7 lateral rebars are exposure; west column top has no rebars exposure; west column bottom has 6 lateral rebars exposure, no buckling. **Transverse Drift Ratio:** 3.2%, max. **Damage Categorization/Index:** DS – 3, minimal damage with limited service-weeks per [2, 3].

Table 4.6. A Detailed Damage Description for Bent 3 of the Bridge and During 7 Biaxials

	Damage State	Damage Description
Bent 3 AT3 – ST3	Biax1:	**Observed Cracking:** East column top has 0.002 in.; east column bottom has 0.002 in.; west column top has 0.002 in.; west column bottom has 0.002 in. **Observed Spalling:** No spalling concrete in both columns top and bottom. **Rebar Yielding and Exposure:** No exposure rebar in both columns top and bottom. **Transverse Drift Ratio:** 0.4%, max. displacement in transverse direction is 7 mm; max. displacement in longitudinal direction is 10.2 mm. **Damage Categorization/Index:** DS – 1, minimal damage with limited service-days per [2, 3].
	Biax2:	**Observed Cracking:** East column top range 0.002 to 0.005 in.; east column bottom has 0.002 in.; west column top has 0.002 in.; west column bottom has 0.002 in. **Observed Spalling:** No spalling concrete in both columns top and bottom **Rebar Yielding and Exposure:** No exposure rebar in both columns top and bottom. **Transverse Drift Ratio:** 0.9%, max. displacement in transverse direction is 16 mm; max. displacement in longitudinal direction is 24.1 mm. **Damage Categorization/Index:** DS – 1, minimal damage with limited service-days per [2, 3].
	Biax3:	**Observed Cracking:** East column top range 0.002 to 0.007 in.; east column bottom range 0.003 to 0.01 in.; west column top has 0.002 in.; west column bottom range 0.003 to 0.005 in. **Observed Spalling:** No spalling concrete in both columns top and bottom. **Rebar Yielding and Exposure:** No exposure rebar in both columns top and bottom. **Transverse Drift Ratio:** 1.3%, max. displacement in transverse direction is 22.9 mm; max. displacement in longitudinal direction is 40.6 mm. **Damage Categorization/Index:** DS – 1, minimal damage with limited service-days per [2, 3].
	Biax4:	**Observed Cracking:** East column top range 0.007 to 0.01 in.; east column bottom range 0.002 to 0.04 in.; west column top range 0.002 to 0.01 in.; west column bottom range 0.007 to 0.06 in. **Observed Spalling:** East column top has flake spall with max. 0.5 in. spall height; east column bottom has flake spall with max. 4 in. spall height; west column top has spall with max. 2.75 in. spall height; west column bottom has ½ in spall with max. 5 in. spall height. **Rebar Yielding and Exposure:** West column bottom has 3 lateral rebars exposed on north side. **Transverse Drift Ratio:** 2.1%, max. displacement in transverse direction is 38.1 mm; max. displacement in longitudinal direction is 68.6 mm. **Damage Categorization/Index:** DS – 2, minimal damage with limited service-days per [2, 3].

	Damage State	Damage Description
	Biax5:	**Observed Cracking:** East column top range 0.01 to 0.02 in.; east column bottom range 0.02 to 0.05 in.; west column top range 0.013 to 0.02 in.; west column bottom range 0.016 to 0.05 in. **Observed Spalling:** East column top has flake spall with max. 0.5 in. spall height; east column bottom has flake spall with max. 4 in. spall height on north; west column top has flake spall with max. 4 in. spall height; west column bottom has ½ circular spall with max. 11 in. spall height. **Rebar Yielding and Exposure:** East column top has no rebar exposure; east column bottom has 2 lateral rebars exposure; west column top has 2 lateral rebars exposure; west column bottom has 16 lateral rebars and 1 longitudinal rebar exposure. **Transverse Drift Ratio:** 4.4%, max. displacement in transverse direction is 80.5 mm; max. displacement in longitudinal direction is 91.2 mm. **Damage Categorization/Index:** DS – 4, moderate damage with limited service-weeks per [2, 3].
Bent 3 AT3 – ST3	Biax6:	**Observed Cracking:** East column top range 0.016 to 0.025 in.; east column bottom range 0.025 to 0.04 in.; west column top range 0.007 to 0.025 in.; west column bottom range 0.007 to 0.04 in. **Observed Spalling:** East column top has spall with max. 3.5 in. spall height in east side; east column bottom has ¼ to ½ circular spall with max. 4.5 in. spall height; west column top has ½ circular spall with max. 7.5 in. spall height; west column bottom has ½ circular spall with max. 11 in spall height. **Rebar Yielding and Exposure:** East column top has 2 lateral rebars exposure; east column bottom has 6 lateral rebars and 1 longitudinal rebar are exposure in east side; west column top 5 lateral rebars and 2 longitudinal rebars are exposure; west column bottom has 21 lateral rebars and 7 longitudinal rebars are exposure. No yielding or buckling. **Transverse Drift Ratio:** 6.9%, max. displacement in transverse direction is 127.5 mm; max. displacement in longitudinal direction is 101.1 mm. **Damage Categorization/Index:** DS – 5, major damage with no service per [2, 3].
	Biax7:	**Observed Cracking:** East column top range 0.007 to 0.02 in.; east column bottom range 0.007 to 0.013 in.; west column top range 0.005 to 0.02 in.; west column bottom range 0.01 to 0.025 in. **Observed Spalling:** East column top has ¼ circular spall with max. 3 in. spall height; east column bottom has ½ circular spall with max. 5 in. spall height; west column top has flake spall; west column bottom has ½ circular spall with 6 in. spall height. **Rebar Yielding and Exposure:** East column top has 2 longitudinal rebars exposure; east column bottom has 13 lateral rebars and 11 longitudinal rebars are exposure; west column top has 5 lateral rebars and 2 longitudinal rebars are exposure; west column bottom has 22 lateral rebars and 11 longitudinal rebars are exposure, 1 incipient in north side **Transverse Drift Ratio:** 7.4% **Damage Categorization/Index:** DS – 5, major damage with no service per [2, 3].

Note: [1]: Nelson and Saiidi, 2007; [2]: Vosooghi and Saiidi, 2010; [3]: Caltrans Design Criteria, 2013

Damage States Per On-Site Damage Survey for Each Bent of the Bridge

- 🟢 **DS-1**: Minor flexural cracks
- 🟡 **DS-2**: First spalling and shear cracks
- 🟠 **DS-3**: Extensive cracks and spalling
- 🟡 **DS-4**: Visible lateral and longitudinal bars
- 🔴 **DS-5**: Imminent failure

After **Biaxial 1** motion

After **Biaxial 2** motion

After **Biaxial 3** motion

After **Biaxial 4** motion

After **Biaxial 5** motion

After **Biaxial 6** motion

North

DS-5

DS-3

DS-5

After **Biaxial 7** motion

North

DS-5

DS-3

DS-5
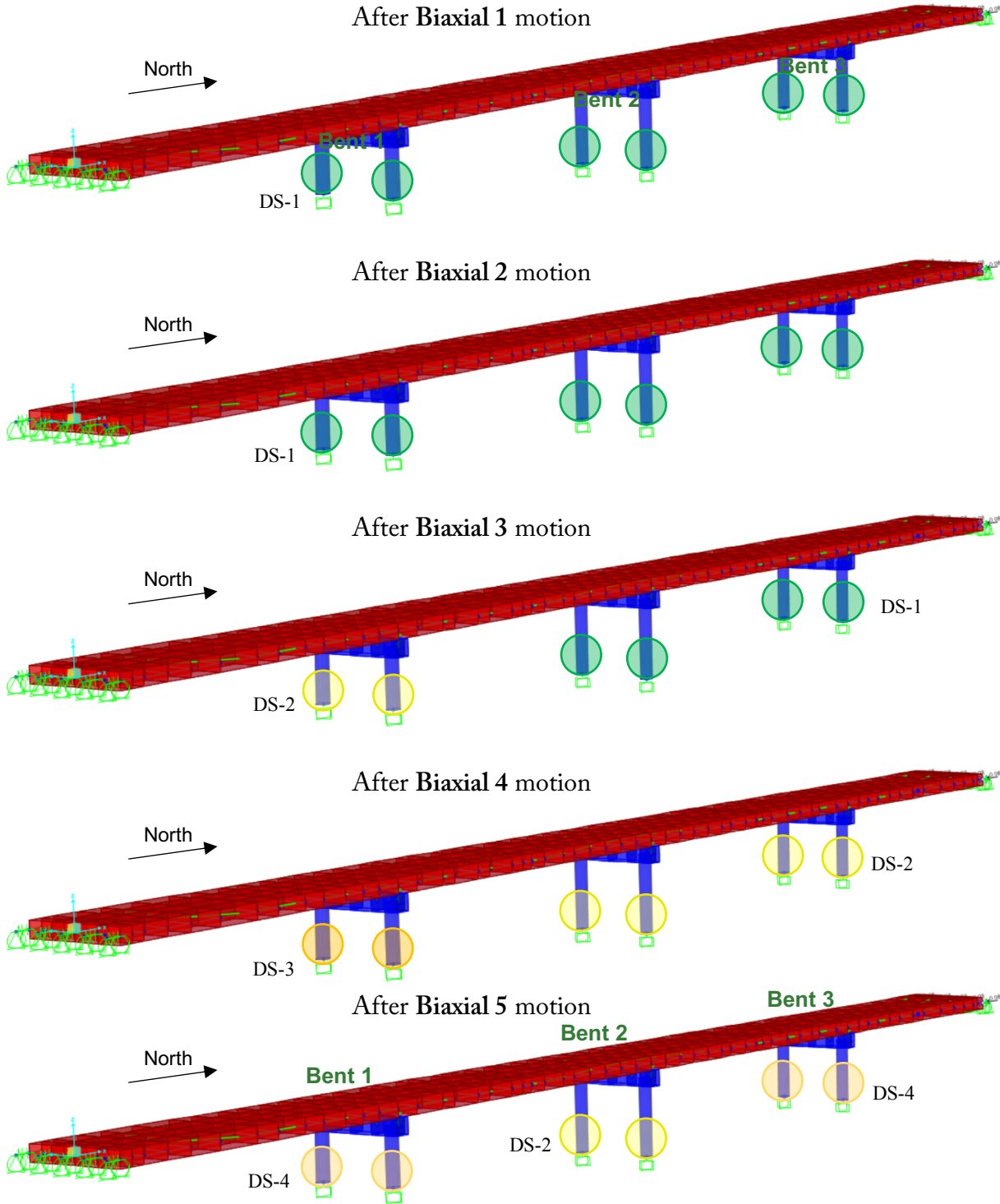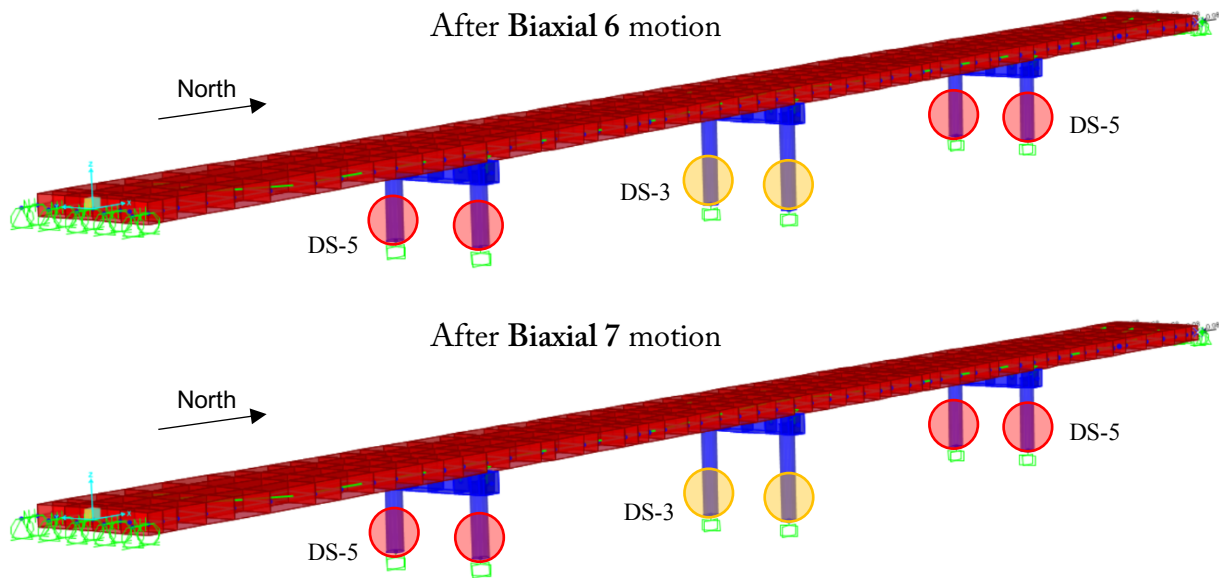
Figure 4.30. Damage States Observed at the Three Bents of the Bridge After Each Biaxial Motions According to On-Site Damage Inspection Report by Nelson et al. (2007). The 3D Rendering ss Schematic

(a)   (b)   (c)
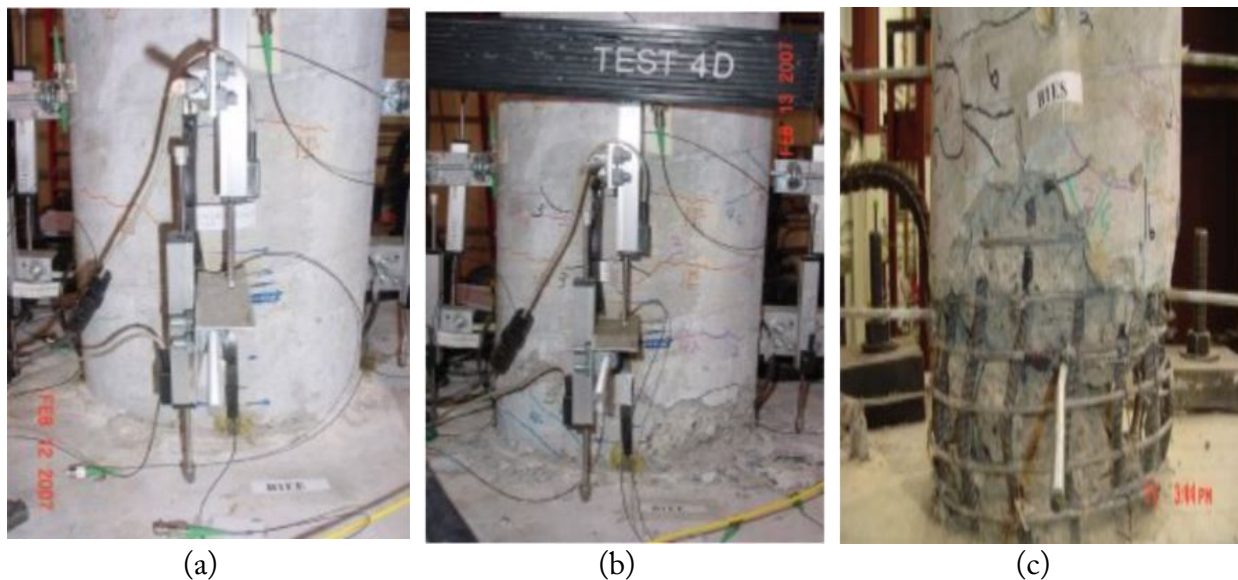
Figure 4.31. Damage Progression in Bent 1 During Biaxials 1, 4, and 7 Respectively.

4.4 A Comparison of Detected Reductions in the c_S with the Surveyed Damage in the Bridge

This section provides a detailed discussion on the obtained damage detection results and their comparison with actual damage in the bridge. Further, we assess the capability of the method in detecting and localizing damage and provide guidance on utilizing the method for monitoring the health of existing bridges in California.

Monitoring changes in the apparent fundamental mode of vibration ($f_{1, app}$) is a popular vibration-based approach among researchers for monitoring a civil structure's health. In this study, we have read these frequencies from the transfer functions (TFs) of the recorded response and have included them in our final results comparison. Note that the $f_{1, app}$ is a damage indicator of the global damage state of the bridge and does not provide explicit information about local damages. Table 4.7 presents the apparent frequencies for the first transverse mode of vibration obtained from recorded response in the bridge. To illustrate the decreasing trend in the $f_{1, app}$, we plotted the points in Figure 4.32, which shows a consistent decreasing trend in the modal frequency, with the exception of motions from biaxial 1 to biaxial 2, where the frequency has slightly increased (~11%). This indicates a slight gain of stiffness between these two events. We note that the sampling rate of recording of biaxial 1 motion is twice the rest of biaxial motions. Hence, we assume minor changes to the test specimen and its monitoring channels after biaxial 1 motion, which are not known to authors. We consider this slight increase in the frequency as no change or damage in the bridge. Damage surveys presented in a previous section also verify that the bridge remained elastic with very minor damage during biaxials 1 and 2. As a result, either of these motions can be considered our baseline undamaged state of the bridge. In this study, we continue using biaxial 1 motion as our baseline state, however, we try to cautiously interpret changes between biaxial 1 to biaxial 2 or 3 motions.

The shear wave velocity c_S is used as a realistic damage-sensitive parameter in this study. For completeness, we present results for identified c_L (compressional velocities) as well, but we do not regard them as a damage indicator for the case-study bridge. Figures 4.33 and 4.34 illustrate reduction in the c_S and c_L for each bent of the bridge (colored bars) and for all damage states. The bars' heights indicate the percentage of the reduction relative to the identified c_S for the undamaged state (biaxial 1, herein). A negative percentage reduction in c_S at a bent indicates increase in the stiffness in that bent relative to biaxial 1. Such increases are artifacts and deemed as no damage in a bent. Most of these increases occurred during the biaxial 2 motion when the bridge behaved stiffer as confirmed by the $f_{1, app}$. These negative bars are not shown in Figure 4.33.

We included a set of hatched bars for the observed reduction in the $f_{1, app}$ for easier comparison. Comparing trends in Figure 4.33 with damage indices shown in Figure 4.30, it is revealed that:

1. The bridge remained elastic from biaxial 1 to biaxial 2 states. In fact, the increase observed in the c_S in bents 1 and 3 suggests that the specimen was stiffened slightly after biaxial 1

motion. This is consistent with observed increase in $f_{1, app}$ as shown in Figure 4.32. The source of this slight increase in stiffness is unknown, but the change is consistently captured by both parameters. Here, we consider this increase as no additional damage to the bents.

2. An exception to our observation above is the reduction in c_S for bent 2 (middle bent). This bent sustained the least overall damage during the testing sequence as illustrated in Figure 4.30. It is noteworthy that the pair AT5-ST2, which represents wave passage through bent 2 of the bridge, has shown a large vibrational energy around 4.5 Hz. As discussed earlier, this second mode of vibration is likely to be a coupled mode of vibration from translation, torsion, and vertical movement of the deck. Its significant energy has impacted the shape of our IRFs, and thus, our identification result for the bent 2 becomes fully biased towards this second apparent mode of vibration. Damage in the bridge can affect both modes, and, therefore, velocities that rely on the second mode can still serve our damage detection goal. However, changes to the bridge's lateral stiffness can cause slight decoupling of the modes at 4.5 Hz, causing additional variability in our identification results for this bent. Moreover, change in the bridge or its over-strengthening effects in other vibrations (e.g., longitudinal, vertical, or torsional) can exacerbate the modes' decoupling and can affect the second mode. These changes are reflected in the results for bent 2. The slight reduction (7%) observed during biaxial 2, when bent 2 did not incur damage, is attributed to these variabilities induced by causes other than damage to piers.

3. For bent 2 (the tallest bent), the percent reduction in c_S remains bounded around 10% during all biaxial motions. This indicates that this bent did not experience a moderate or major damage, consistent with damage survey narratives (Fig. 4.30).

4. Bent 1 (the shortest bent), marks the onset of damage during biaxial 3 motion. During this motion, bent 1 shows an 11% reduction in c_S. Meanwhile, bent 3 (the second most damaged) does not present any reduction in its velocity during biaxial 3. This is very consistent with surveyed damage shown in Figure 4.30.

5. During biaxial 4 motion, both bents 1 and 3 show a reduction in their c_S. The detected reduction in c_S at bent 3 is abrupt and large. This is due to a softening of bent 1 during previous motion that caused a redistribution of shear demand among the bents during the biaxial 4 motion. The bent 3, being the second-shortest, was apportioned a larger shear demand, which induced damage during biaxial 4.

6. During biaxial 5, both bents 1 and 3 presented a larger reduction in their c_S, consistent with observed damage indices.

7. The largest reduction in c_S for bents 1 and 3 occurred during biaxials 6 and 7 motions when both bents showed over 40% reduction in their shear wave velocities. The detected reduction was doubled compared to biaxial 5 motion. Reviewing the damage surveys and

indices, both bents have sustained major damage during biaxials 6 and 7. This is consistent with the large reductions in c_S.

8. The reduction of c_S is generally consistent with the observed location and severity of damage during each shaking, as presented in Figure 4.33. This reveals that the wave method, utilizing a Timoshenko beam model, was capable of detecting the progression of damage in the bents and identifying the location of the most severe damage. It was also capable of identifying the onset of damage in bent 1 during biaxial 3 and the onset of damage in bent 3 during biaxial 4 motion.

9. The proposed wave method for bridge damage detection is a fast and inexpensive tool for real-time or near-real-time damage detection and localization in similar bridge systems. It owes its speed to its simple underlying Timoshenko beam model, avoiding the need for detailed structural drawings or finite element modeling of the bridge.

10. Figure 4.33 also shows reducing trends in the first apparent transverse mode of vibration of the bridge ($f_{1,\,app}$). The trends reveal significant reduction in the modal frequencies after the fourth shaking (biaxial 4). This is consistent with the detected reduction in c_S at both bents 1 and 3. The overall degrees of reductions in frequencies and c_S are comparable. However, the wave method is superior in its ability to localize the damage at bents 1 and 3.

11. As discussed in the results section of this study, due to the predominantly shear-like movement of the deck and the large gravity loads on the piers, the longitudinal (i.e., compression) wave velocity in the piers, c_L, has relatively large and volatile values and is not a reliable damage-sensitive parameter for this type of bridge structure. Figure 4.34 shows the percent reduction in the c_L. The changes are somewhat inconsistent with the actual damage in bents 1 and 3 during smaller motions. For example, the c_L reductions overestimated damage in bent 1 during biaxials 1 through 3, while it underestimated damage in bent 3 during the biaxial 4 motion. Nevertheless, the overall reduction in c_L remains consistent with overall damage in the piers and reductions in the modal frequency. Figure 4.34 shows that even c_L could show the location of the most severe damages at bents 1 and 3 during larger biaxial motions.

Table 4.7. Observed Change in the Fundamental Mode, Transverse Direction

Event	Apparent Frequency	
	f_{1app} (Hz)	Change w.r.t. Biaxial 1 (%)
Biaxial 1	2.25	0.0
Biaxial 2	2.50	-11.1
Biaxial 3	2.15	4.4
Biaxial 4	1.80	20.0
Biaxial 5	1.40	37.8
Biaxial 6	1.15	48.9
Biaxial 7	1.10	51.1
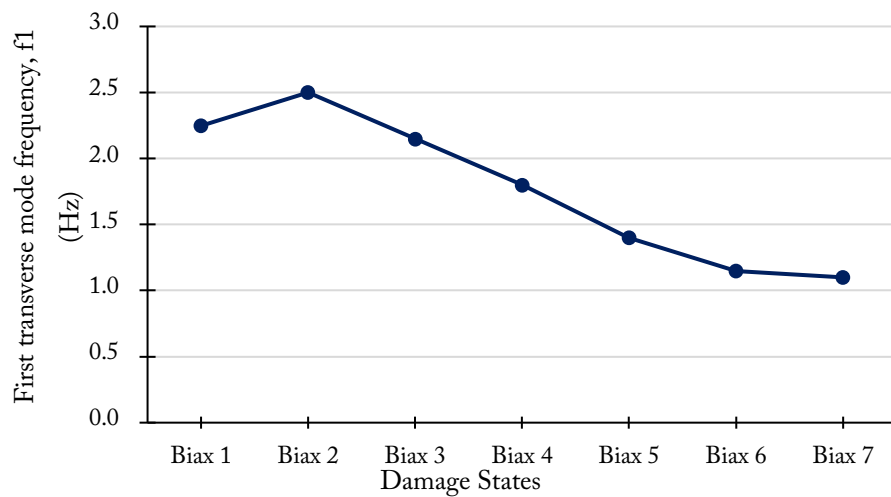
Figure 4.32. First Transverse Mode Frequency f1 from Actual Tested Bridge
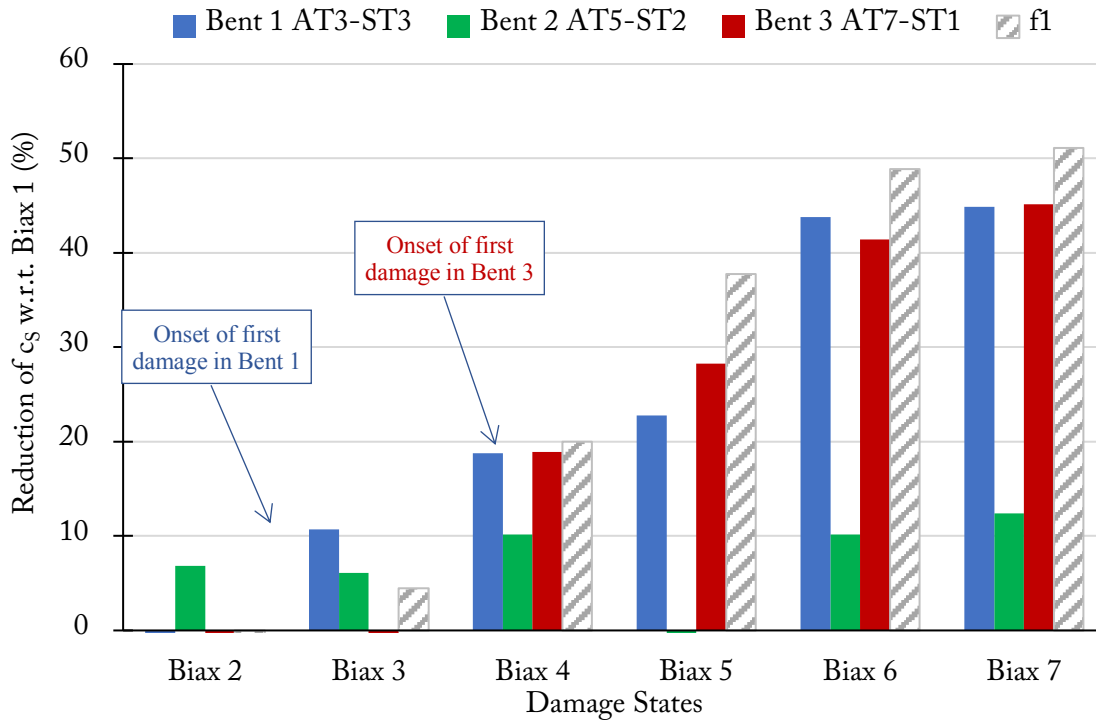
Note: First Transverse Mode's Apparent Frequency is Shown for Comparison

Figure 4.33. Reduction of c_S Three Bents of Actual Bridge
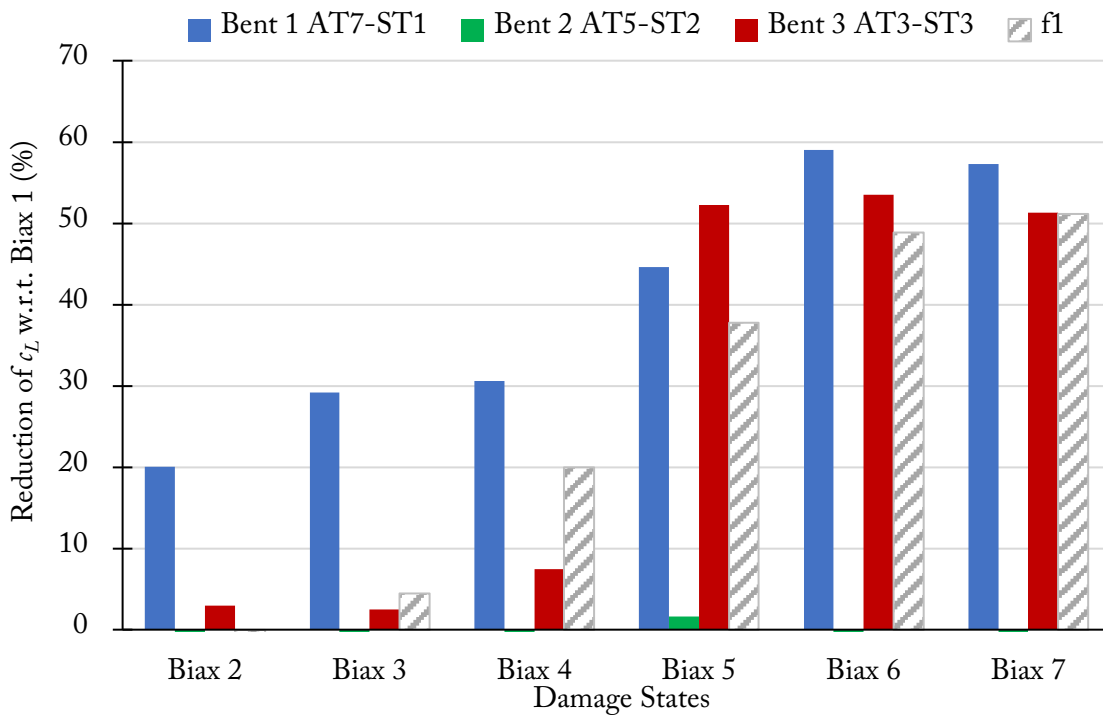
Note: The change is volatile and not considered as a reliable damage indicator for smaller shakings.

Figure 4.34. Reduction of c_L for Three Bents of Actual Bridge. The Change is Volatile and Not Considered a Reliable Damage Indicator for Smaller Shakings

4.5. Detecting Damage in the Nonlinear FEM Using the Wave Method

We attempt to detect damage in our finite element model (FEM) using the proposed wave method. The FEM's nonlinear hinge results suggest that the column hinges form as early as biaxial 3 motion. The SAP2000 output shows that bent 1 suffers the most significant hinge nonlinearity followed by the bent 3. Figure 3.11 illustrates the onset of nonlinear behavior at bent 1. The sequence of damage in the FEM's three bents was slightly different from the actual bridge due to modeling approximations. However, similar to the actual bridge, the largest damage was observed at bent 1 and the least damage was observed at bent 3. Figures 4.35 and 4.36 illustrate reduction in the identified c_S and c_L for the FEM. The plots reveal that:

1. Unlike the results for the actual bridge, a small reduction in c_S was detected during biaxial 2 motion. This result confirm that the actual test specimen must have experienced a slight modification which resulted in its increased stiffness during biaxial 2 motion.

For bent 2 (pair AT5-ST2), similar to the actual bridge, the fitting results show a coupled mode of vibration at 4.5 Hz which affects the fits and the identified c_S for this bent. In fact, all fits for

this bent were biased towards the higher mode. This resulted in a spike in c_S reduction during biaxial 2, similar to the result obtained for the actual bridge. Therefore, these changes may not be solely due to damage and could be caused by changes to other modes of vibration coupled at higher frequencies. Note that the estimated c_S for bent 2 does not experience any further reduction during larger biaxial motions, indicating that this bent likely remained very lightly damaged.

2. Results for bents 1 and 3 are consistent with the hinge formation sequence in the FEM. Bent 1 was damaged first, followed by bent 3 from biaxials 3 to 7. At biaxial 4, the reduction in c_S for bent 1 is very large relative to bent 3. Investigating the hinge hysteresis results shows a reasonable correlation between the nonlinearity in the columns and the observed reduction in c_S.
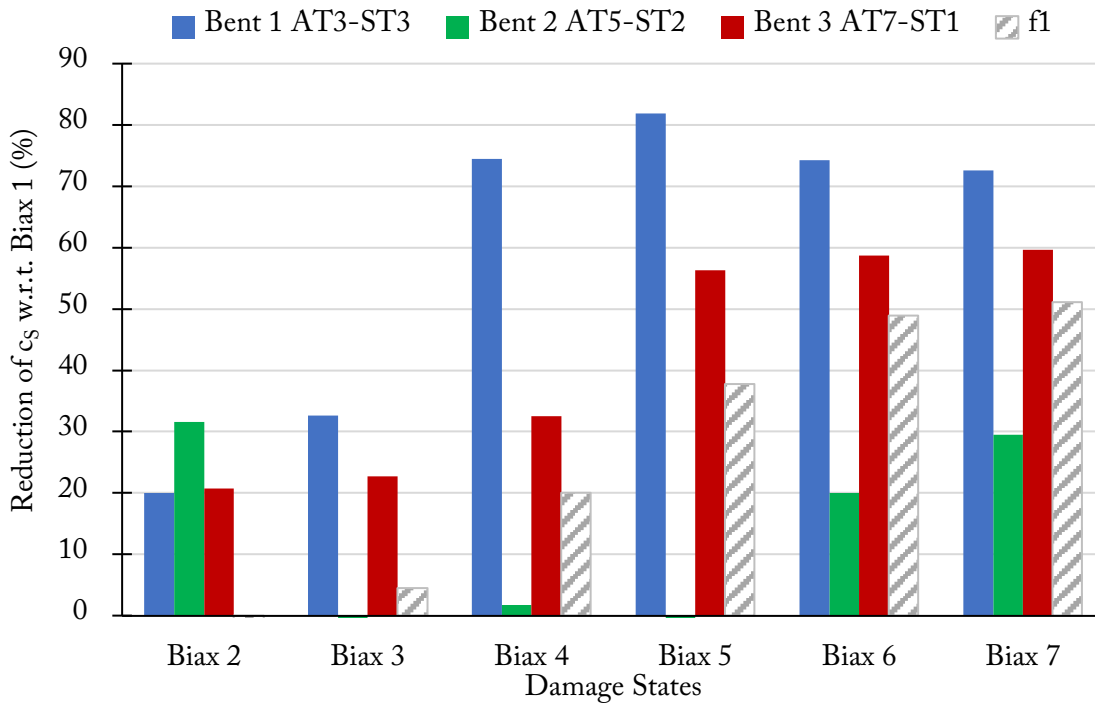
Figure 4.35. Reduction of c_S for Three Bents for FEM Response
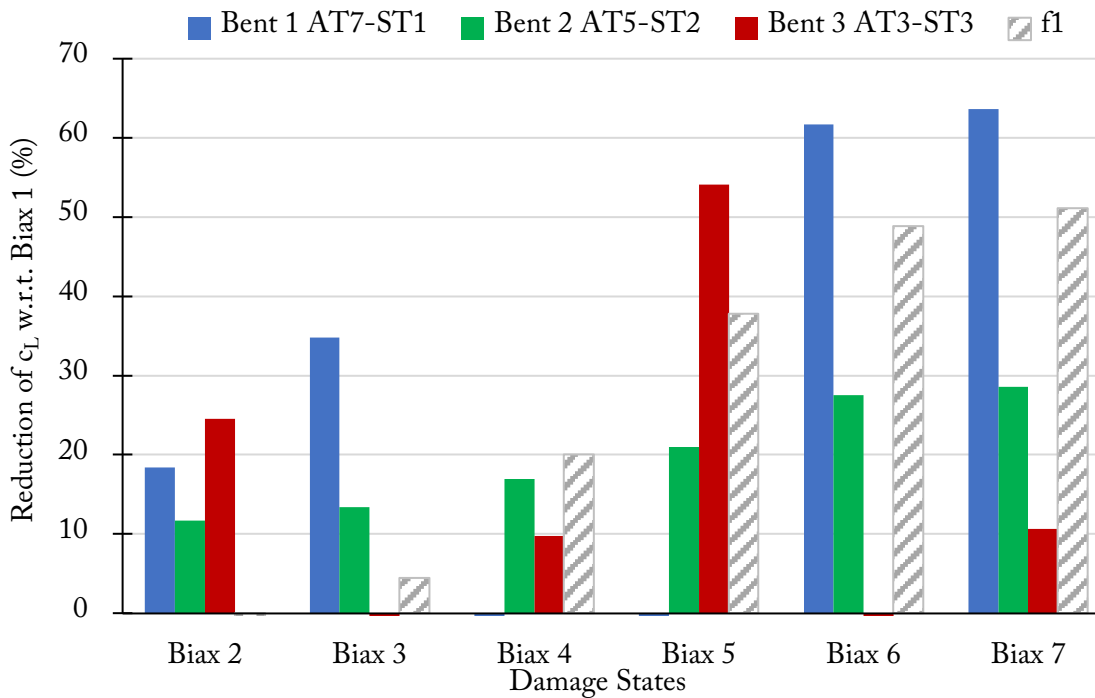
Figure 4.36 Reduction of c_L for Three Bents for FEM Response

5. Summary & Conclusions

In this study, we aimed to find the location and severity of damage in a quarter-scaled shake-table-tested bridge progressively damaged by seven biaxial base excitations. The bridge was a 4-span reinforced concrete structure comprising two columns at each bent (six columns total) and a post-tensioned flat slab deck. We used the waveform inversion algorithm and enhanced it to fit, in the Least-square sense, a uniform Timoshenko beam (TB) model in the recorded deck and base response to estimate the longitudinal and shear wave velocities, c_L and c_S, for the best fitted TB model. The shear wave velocity, c_S was our damage-sensitive parameter, and its reduction is interpreted as a reduction of stiffness in a bent, corresponding to damage in a pair of columns.

In this study, enhancements made to our damage detection algorithm include the following:

(1) We applied a nonlinear least-square regression to identify both the longitudinal and shear (c_L and c_S) wave velocities in the TB model. This is the first time both parameters are identified and reported for a damaged bridge using the wave method;

(2) We found the best (i.e., optimal) value for the damping, resulting in minimum fitting error, by iterating over a range of damping values;

(3) Moreover, we ran our analyses rigorously for a wide range of initial values to determine the sensitivity of our results to the initial values and to avoid being trapped in local minima of the objective function; and

(4) We included a final tier to our analysis to eliminate nonphysical solutions by comparing the distance between the actual (i.e., recorded) and model-predicted first mode of transverse vibration, $f_{1,\,app}$.

In addition, the complexity of the bridge response led us to create a detailed nonlinear finite element model (FEM) of the bridge to further investigate its response. The auxiliary FEM was subjected to the same biaxial base accelerations, and the modal frequencies, mode shapes, and its deck response were processed.

Our results show that the reduction of c_S is generally consistent with the observed spatial distribution and severity of damage during each biaxial motion. At bent 1 and bent 3, c_S is consistently reduced with the progression of damage. The reduction correctly detects the onset of damage at bent 1 during biaxial 3, while it shows the onset of damage in bent 3 during biaxial 4, both consistent with surveyed damage in the bridge. The most significant reduction was caused by the last two biaxial motions in bents 1 and 3, consistent with the surveyed damage. In bent 2 (middle bent), the reduction trend in c_S was relatively minor, indicating minor damage in this bent, which was also consistent with actual damage.

We conclude that the method was capable of detecting damage progression in the bridge and identifying the location of the most severe damage. The proposed methodology is a fast and inexpensive tool for real- or near-real-time damage detection and localization in similar bridge structures. It owes its speed to the simplicity of the Timoshenko beam model and the ability to analytically solve its response in the frequency domain. Hence, the analysis time required is much shorter compared to the FEM updating approaches or methods that work with large amounts of data collected from the bridge.

The proposed method requires acceleration data from only a few channels on the bridge. For example, for the 4-span case-study bridge, we require an accelerometer on top of each bent or at its proximity as a receiving station as well as an accelerometer at the base (i.e., top of foundation or pile cap). If the bridge has a short span, then one accelerometer at the foundation/base will suffice. Therefore, for the 4-span example, only four accelerometers will be enough to detect and localize damage, as presented in this study. This is a very important advantage to the method, since many of the bridges currently instrumented in California comprise low-density sensor arrays. As discussed in Section 4.4, this study reveals that the method is viable for use in identification and damage detection in similar bridge systems. We recommend using this proposed method to identify instrumented bridges in California in order to create a baseline shear wave velocity for their undamaged state. In the event of a large motion, the method can be applied to detect changes in structural stiffness and provide clues on the location of a potential damage, rapidly.

The parametric Timoshenko beam (TB) model used here is one-dimensional. Hence, it does not account for coupled torsional-translational responses. This is one of the limitations of the relatively simple TB model. Moreover, the model is linear and aims to find estimated properties of an equivalent softened beam. Thus, significant plastic hinge formation at a column, which can be followed by a rigid-body rotation around the hinge or cause geometric nonlinearity in the system, could represent behavior not fully captured by our model. Such large loss of stiffness and rotation concentrated at the base of a column cannot be fully captured by the elastic TB model. Therefore, we believe the model can be improved by generalizing it to include coupling with torsion and the ability to model hinges at its base. Moreover, the TB model used here includes a uniform density equivalent to overall bridge density. We believe the model can be further improved by layering it such that it includes a large mass at the upper layer, representing the deck and blocks, and a smaller density for the unbraced length of the columns. We recommend these improvements to enhance the method and its estimation accuracy for similar bridge structures.

Appendix A

A summary of damage visually observed after each biaxial motion at the column, including concrete cracking and spalling and steel rebar condition. All tables in this appendix are reproduced and/or reorganized from Nelson et al. (2007).

Table A-1. A Summary of Observed Maximum Crack Width (inches)

BENT 1								
Hinge Location	Inspected face	Biaxial 1	Biaxial 2	Biaxial 3	Biaxial 4	Biaxial 5	Biaxial 6	Biaxial 7
East Column Top	North	0.009	0.025	0.025	0.025	0.025	0.03	-
	South	0.013	0.016	0.013	0.013	0.013	0.02	-
	East	0.009	0.016	0.013	0.013	0.013	0.02	-
	West	0.007	0.025	0.016	0.016	0.016	0.02	-
East Column Bottom	North	0.002	0.002	0.007	0.01	0.03	0.035	-
	South	0.002	0.002	0.009	0.01	0.03	0.035	-
	East	0.002	0.002	0.003	0.005	0.03	0.035	-
	West	-	0.002	0.025	0.005	0.02	0.03	-
West Column Top	North	0.002	0.002	0.002	0.005	0.05	0.01	-
	South	0.002	0.002	0.001	0.005	0.007	0.01	-
	East	0.002	0.002	0.002	0.005	0.025	0.03	-
	West	0.002	0.002	0.001	0.002	0.025	0.03	-
West Column Bottom	North	0.002	0.002	0.003	0.02	0.02	0.03	-
	South	0.002	0.002	0.013	0.03	0.03	0.035	-
	East	0.002	0.002	0.013	0.02	0.02	0.03	-
	West	0.002	0.002	0.003	0.03	0.03	0.035	-

BENT 2								
Hinge Location	Inspected face	Biaxial 1	Biaxial 2	Biaxial 3	Biaxial 4	Biaxial 5	Biaxial 6	Biaxial 7
East Column Top	North	0.002	0.002	0.003	0.002	0.005	0.005	0.007
	South	0.002	0.002	0.002	0.005	0.01	0.007	0.013
	East	0.002	-	0.002	0.002	0.013	0.007	0.02
	West	0.002	0.002	0.003	0.002	0.0.05	0.02	0.007
East Column Bottom	North	0.002	0.002	0.003	0.007	0.009	0.013	0.009
	South	0.002	0.002	0.005	0.005	0.007	0.01	0.013
	East	-	0.002	0.003	0.003	0.007	0.016	0.007
	West	-	0.002	0.003	0.005	0.005	0.007	0.013
West Column Top	North	0.002	0.002	0.002	0.002	0.007	0.003	0.007
	South	0.002	0.002	0.002	0.002	0.003	0.007	0.005
	East	0.002	0.002	0.002	0.003	0.007	0.007	0.009
	West	0.002	0.002	0.002	0.003	0.01	0.005	0.02
West Column Bottom	North	0.002	0.002	0.002	0.005	0.016	0.013	0.02
	South	0.002	0.002	0.003	0.01	0.013	0.01	0.013
	East	-	0.002	0.003	0.003	0.005	0.007	0.01
	West	0.002	0.002	0.003	0.005	0.013	0.016	0.025

BENT 3								
Hinge Location	Inspected face	Biaxial 1	Biaxial 2	Biaxial 3	Biaxial 4	Biaxial 5	Biaxial 6	Biaxial 7
East Column Top	North	0.002	0.002	0.005	0.01	0.02	0.025	0.025
	South	0.002	-	0.002	0.01	0.01	0.016	0.025
	East	0.002	0.005	0.007	0.007	0.01	0.025	0.016
	West	0.002	0.002	0.002	0.01	0.02	0.02	0.025
East Column Bottom	North	0.002	0.002	0.007	0.04	0.03	0.04	0.025
	South	-	0.002	0.005	0.007	0.02	0.03	0.02
	East	0.002	0.002	0.01	0.04	0.05	0.04	0.05
	West	-	0.002	0.003	0.002	0.03	0.025	0.025
West Column Top	North	0.002	0.002	0.002	0.005	0.013	0.025	0.03
	South	0.002	-	0.002	0.01	0.016	0.1	0.013
	East	0.002	0.002	0.002	0.002	0.02	0.007	0.016
	West	0.002	0.002	0.002	0.005	0.02	0.025	0.04
West Column Bottom	North	-	0.002	0.005	0.06	0.05	0.025	0.016
	South	0.003	0.002	0.005	0.01	0.03	0.03	0.016
	East	0.002	0.002	0.005	0.013	0.02	0.04	0.04
	West	-	0.002	0.003	0.007	0.016	0.007	0.002

Table A-2. A Summary of Observed Concrete Spalling

BENT 1															
Hinge Location	Inspected face	Biaxial 1		Biaxial 2		Biaxial 3		Biaxial 4		Biaxial 5		Biaxial 6		Biaxial 7	
		Max. Spall Height	Spall Description	Max. Spall Height	Spall Description	Max. Spall Height	Spall Description	Max. Spall Height	Spall Description	Max. Spall Height	Spall Description	Max. Spall Height	Spall Description	Max. Spall Height	Spall Description
East Column Top	North	-	-	-	-	0.75	min. flake	-	-	1.5	flake	1.5	-	5.5	½ circ.
	South	-	-	-	-	-	-	-	-	3	spall	3	-	3	½ circ.
	East	-	-	-	-	1	flake	-	-	1	spall	1	¼ circ.	2.5	½ circ.
	West	-	-	-	-	-	-	1	spall	2	spall	2.5	-	6	½ circ.
East Column Bottom	North	-	-	-	-	1.5	flake	3	¼ circ	4	½ circ.	4	¾ circ.	6.5	circle
	South	-	-	-	-	0.25	min. flake	-	-	4	½ circ.	-	-	8	circle
	East	-	-	-	-	0.75	flake	4.5	spall	4	½ circ.	-	-	6	circle
	West	-	-	-	-	0.25	min. flake	-	-	-	-	-	-	6	circle
West Column Top	North	-	-	-	-	-	-	-	-	4	spall	-	-	4	spall
	South	-	-	-	-	-	-	-	-	-	-	-	-	-	-
	East	-	-	-	-	-	-	4	spall	2.5	spall	3.5	spall	-	¼ circ.
	West	-	-	-	-	-	-	-	-	1	flake	-	-	5	¼ circ.
West Column Bottom	North	-	-	-	-	-	-	3	¼ circ.	3	¾ circ.	3.5	¾ circ.	6	circle
	South	-	-	-	-	-	-	-	-	3	¾ circ.	3	circle	9	circle
	East	-	-	-	-	-	-	-	-	3	spall	3	-	5	circle

BENT 1															
Hinge Location	Inspected face	Biaxial 1		Biaxial 2		Biaxial 3		Biaxial 4		Biaxial 5		Biaxial 6		Biaxial 7	
		Max. Spall Height	Spall Descr-iption	Max. Spall Height	Spall Descr-iption	Max. Spall Height	Spall Descr-iption	Max. Spall Height	Spall Descr-iption	Max. Spall Height	Spall Descr-iption	Max. Spall Height	Spall Descr-iption	Max. Spall Height	Spall Descr-iption
	West	-	-	-	-	0.125	min. flake	-	-	3	¾ circ.	3	-	8	circle

BENT 2															
Hinge Location	Inspected face	Biaxial 1		Biaxial 2		Biaxial 3		Biaxial 4		Biaxial 5		Biaxial 6		Biaxial 7	
		Max. Spall Height	Spall Description	Max. Spall Height	Spall Description	Max. Spall Height	Spall Description	Max. Spall Height	Spall Description	Max. Spall Height	Spall Description	Max. Spall Height	Spall Description	Max. Spall Height	Spall Description
East Column Top	North	-	-	-	-	-	-	-	-	-	-	-	-	-	-
	South	-	-	-	-	-	-	-	-	-	-	-	-	-	-
	East	-	-	-	-	-	-	-	-	-	-	-	-	-	-
	West	-	-	-	-	-	-	-	-	-	-	2	¼ circ	3	¼ circ
East Column Bottom	North	-	-	-	-	-	-	-	Flake	3	Spall	4	½ circ	5	½ circ
	South	-	-	-	-	-	-	-	-	-	-	-	Flake	5	½ circ
	East	-	-	-	-	-	-	-	-	-	-	5	½ circ	4	½ circ
	West	-	-	-	-	-	-	-	-	3	Spall	1	Flake	-	Flake
West Column Top	North	-	-	-	-	-	-	-	-	-	-	-	-	-	-
	South	-	-	-	-	-	-	-	-	-	-	-	-	-	-
	East	-	-	-	-	-	-	-	-	-	-	-	Flake	-	Flake
	West	-	-	-	-	-	-	-	-	-	-	-	-	-	Flake
West Column Bottom	North	-	-	-	-	-	-	-	Flake	-	-	2	¼ circ	2	½ circ
	South	-	-	-	-	-	-	-	-	2.5	Spall	5	¼ circ	6	½ circ
	East	-	-	-	-	-	-	-	-	-	-	2	¼ circ	4	½ circ
	West	-	-	-	-	-	-	-	-	1.5	Flake	4	¼ circ	5	½ circ

BENT 3															
Hinge Location	Inspected face	Biaxial 1		Biaxial 2		Biaxial 3		Biaxial 4		Biaxial 5		Biaxial 6		Biaxial 7	
		Max. Spall Height	Spall Descr-iption	Max. Spall Height	Spall Descr-iption	Max. Spall Height	Spall Descr-iption	Max. Spall Height	Spall Descr-iption	Max. Spall Height	Spall Descr-iption	Max. Spall Height	Spall Descr-iption	Max. Spall Height	Spall Descr-iption
East Column Top	North	-	-	-	-	-	-	-	-	-	-	-	-	0.25	Min. flake
	South	-	-	-	-	-	-	-	-	0.75	Min. flake	-	-	-	-
	East	-	-	-	-	-	-	0.5	Min. flake	2	Flake	3.5	Spall	3.25	Spall
	West	-	-	-	-	-	-	-	-	-	-	-	-	0.375	Flake
East Column Bottom	North	-	-	-	-	-	-	4	Flake	4	¼ circ	4.5	Spall	6.5	1.2 circ
	South	-	-	-	-	-	-	-	-	0.75	Min. flake	4.5	¼ circ	4.5	½ circ
	East	-	-	-	-	-	-	-	-	0.5	Min. flake	4	Spall	4	½ circ
	West	-	-	-	-	-	-	-	-	1	Min. flake	4	½ circ	5	½ circ
West Column Top	North	-	-	-	-	-	-	-	-	-	-	-	-	3	½ circ
	South	-	-	-	-	-	-	-	-	0.5	Min. flake	0.5	Min. flake	1	Flake
	East	-	-	-	-	-	-	2.75	Spall	4	¼ circ	7.5	½ circ	7	½ circ
	West	-	-	-	-	-	-	-	-	-	-	-	-	-	-
	North	-	-	-	-	-	-	5	½ circ	8	½ circ	10.5	½ circ	11.5	¾ circ
	South	-	-	-	-	-	-	4		6.5	½ circ	9	½ circ	9	¾ circ

BENT 3															
Hinge Location	Inspected face	Biaxial 1		Biaxial 2		Biaxial 3		Biaxial 4		Biaxial 5		Biaxial 6		Biaxial 7	
		Max. Spall Height	Spall Descr-iption	Max. Spall Height	Spall Descr-iption	Max. Spall Height	Spall Descr-iption	Max. Spall Height	Spall Descr-iption	Max. Spall Height	Spall Descr-iption	Max. Spall Height	Spall Descr-iption	Max. Spall Height	Spall Descr-iption
West Column Bottom	East	-	-	-	-	-	-	-		0.75	Flake	0.75	Flake	0.75	Flake
	West	-	-	-	-	-	-	5	½ circ	11	½ circ	11	½ circ	11.25	¾ circ

Table A-3. A summary of observed damage of rebars

BENT 1									
Hinge Location	Inspected face	Biaxial 1	Biaxial 2	Biaxial 3	Biaxial 4	Biaxial 5	Biaxial 6	Biaxial 7	
		No. Exp Long./Lat. Bars	No. Exp Long./Lat. Bars	No. Exp Long./Lat. Bars	No. Exp Long./Lat. Bars	No. Exp Long./Lat. Bars	No. Exp Long./Lat. Bars	No. Exp Long./Lat. Bars	Extent of Bar Buckling or Fracture
East Column Top	North	-	-	-	-	0/1	-	0/3	-
	South	-	-	-	-	0/1	-	0/2	-
	East	-	-	-	-	-	-	-	-
	West	-	-	-	0/1	0/1	3/4	3/4	-
East Column Bottom	North	-	-	-	0/2	0/2	-	7/4	2 long. bar & 1 lat. fractured; 5 long. buckled
	South	-	-	-	-	-	5/5	7/6	all bars buckled
	East	-	-	-	-	-	4/4	7/4	3 long. & 1 lat. fractured; 4 long. buckled
	West	-	-	-	-	-	1/2	7/4	all bars buckled
West Column Top	North	-	-	-	-	-	-	0/1	-
	South	-	-	-	-	-	-	-	-
	East	-	-	-	-	-	0/1	0/1	-
	West	-	-	-	-	-	-	3/3	-
West Column Bottom	North	-	-	-	0/2	-	3/2	7/4	-
	South	-	-	-	-	0/3	5/5	7/8	3 long. buckled
	East	-	-	-	-	-	-	6/4	-
	West	-	-	-	-	0/3	1/2	7/6	3 long. buckled

BENT 2									
Hinge Location	Inspected face	Biaxial 1	Biaxial 2	Biaxial 3	Biaxial 4	Biaxial 5	Biaxial 6	Biaxial 7	
		No. Exp Long./Lat. Bars	No. Exp Long./Lat. Bars	No. Exp Long./Lat. Bars	No. Exp Long./Lat. Bars	No. Exp Long./Lat. Bars	No. Exp Long./Lat. Bars	No. Exp Long./Lat. Bars	Extent of Bar Buckling or Fracture
East Column Top	North	-	-	-	-	-	-	-	-
	South	-	-	-	-	-	-	-	-
	East	-	-	-	-	-	-	-	-
	West	-	-	-	-	-	-	-	-
East Column Bottom	North	-	-	-	-	-	0/3	0/4	-
	South	-	-	-	-	-	-	-	-
	East	-	-	-	-	-	0/1	0/3	-
	West	-	-	-	-	-	-	-	-
West Column Top	North	-	-	-	-	-	-	-	-
	South	-	-	-	-	-	-	-	-
	East	-	-	-	-	-	-	-	-
	West	-	-	-	-	-	-	-	-
West Column Bottom	North	-	-	-	-	-	0/1	-	-
	South	-	-	-	-	-	0/1	0/3	-
	East	-	-	-	-	-	-	-	-
	West	-	-	-	-	-	-	0/3	-

BENT 3									
Hinge Location	Inspected face	Biaxial 1	Biaxial 2	Biaxial 3	Biaxial 4	Biaxial 5	Biaxial 6	Biaxial 7	
		No. Exp Long./Lat. Bars	No. Exp Long./Lat. Bars	No. Exp Long./Lat. Bars	No. Exp Long./Lat. Bars	No. Exp Long./Lat. Bars	No. Exp Long./Lat. Bars	No. Exp Long./Lat. Bars	Extent of Bar Buckling or Fracture
East Column Top	North	-	-	-	-	-	-	-	-
	South	-	-	-	-	-	-	-	-
	East	-	-	-	-	-	0/2	0/2	-
	West	-	-	-	-	-	-	-	-
East Column Bottom	North	-	-	-	-	0/2	-	2/5	-
	South	-	-	-	-	-	1/3	4/3	-
	East	-	-	-	-	-	-	2/2	-
	West	-	-	-	-	-	0/3	3/3	-
West Column Top	North	-	-	-	-	-	-	-	-
	South	-	-	-	-	-	-	-	-
	East	-	-	-	-	0/2	2/5	2/5	-
	West	-	-	-	-	-	-	-	-
West Column Bottom	North	-	-	-	0/3	0/6	2/8	3/9	1 incipient
	South	-	-	-	-	0/4	2/6	4/6	-
	East	-	-	-	-	0/1	0/1	0/1	-
	West	-	-	-	-	1/5	3/6	4/6	-

Bibliography

California Department of Transportation. *Seismic Design Criteria Version 1.7*. April 2013.

Catbas, F. N., & Aktan, A. E. (2000). "Modal analysis as a bridge health monitoring tool." Advanced Technology in Structural Engineering: Structures Congress, ASCE, Reston, VA, 1–10.

Celebi, M. (2006). "Real-time seismic monitoring of the integrated Cape Girardeau Bridge array and recorded earthquake response." Structures Congress, ASCE, Reston, VA, 1–10.

Costa, B. J. A., Magalhaes, F., Cunha, A., & Figueiras, J. (2014). Modal analysis for the rehabilitation assessment of the Luiz I bridge. *J. Bridge Eng.*, 19(12).

Ebrahimian, M., & Todorovska, M. I. (2014). Wave propagation in a Timoshenko beam building model. *Journal of Engineering Mechanics*, 140(5), 04014018.

Ebrahimian, M., & Todorovska, M. I. (2015). Structural system identification of buildings by a wave method based on a nonuniform Timoshenko beam model. *Journal of Engineering Mechanics*, 141(8), 04015022.

Hsieh, K. H., Halling, M. W., Barr, P. J., & Robinson, M. J. (2008). Structural damage detection using dynamic properties determined from laboratory and field testing. *J. Perform. Constr. Facil.*, 22(4), 238–244.

Huang, Q., Gardoni, P., & Hurlebaus, S. (2011). Adaptive reliability analysis of reinforced concrete bridges using nondestructive testing. *J. of Risk and Uncertainty in Eng. Systems, Part A: Civil Eng.*

Iranmanesh, A., & Ansari, F. (2014). Energy-based damage assessment methodology for structural health monitoring of modern reinforced concrete bridge columns. *J. Bridge Eng.*, 19(8), A4014004.

Nelson, R. B., Saiidi, M., & Zadeh, S. (2007). "Experimental evaluation of performance of conventional bridge systems." No. CCEER-07-04, University of Nevada, Reno.

Noman, A. S., Deeba, F., & Bagchi, A. (2013). Health monitoring of structures using statistical pattern recognition techniques. *J. Perform. Constr. Facil.*, 27(5), 575–584.

Ntotsios, E., Papadimitriou, C., Panetsos, P., Karaiskos, G., Perros, K., & Perdikaris, P. C. (2008). Bridge health monitoring system based on vibration measurements. *Bull Earthquake Eng.* 7, 469–483.

Rahmani, M., & Todorovska, M. I. (2013). 1D system identification of buildings from earthquake response by seismic interferometry with waveform inversion of impulse responses – method and application to Millikan Library. *Soil Dyn. Earthq. Eng.*, 47, 157–174. DOI: 10.1016/j.soildyn.2012.09.014.

Rahmani, M., & Todorovska, M. I. (2014). 1D system identification of a 54-story steel frame building by seismic interferometry. *Earthquake Engng Struct. Dyn.*, 43(4), 627–640.

Rahmani, M., & Todorovska, M. I. (2015). Structural health monitoring of a 54-story steel frame building using a wave method and earthquake records. *Earthquake Spectra*, 31(1), 501–525.

Rahmani, M., Ebrahimian M., & Todorovska, M. I. (2015). Time-wave velocity analysis for early earthquake damage detection in buildings: Application to a damaged full-scale RC building. *Earthq. Eng. Struct. Dyn.*, 44, 619–636. DOI: 10.1002/eqe.2539.

Rahmani, M., Grabinski, J. R., Todorovska, M. I., & Ebrahimian M. (2021). "Earthquake damage detection and localization in a full-scale slice of a 7-story RC shear wall building." Proceeding of the 17th World Conf. on Earthquake Engineering (17WCEE), Sendai, Japan, p. 6b0016.

Rahmani, M., & Todorovska M. I. (2021). Structural health monitoring of a 32-storey steel-frame building using 50 years of seismic monitoring data. *Journal of Earthquake Engineering and Structural Dynamics*, 50(6), 1777–1800.

Seo, J., Hu, J. W., & Lee, J. (2015). Summary review of structural health monitoring applications for highway bridges. *J. Perform. Constr. Facil.*, 30(4), 04015072.

Snieder, R., & Safak, E. (2006). Extracting the building response using interferometry: theory and applications to the Millikan Library in Pasadena, California. *Bull. Seism. Soc. Am.*, 96(2), 586–598.

Soyoz, S., Feng, M. Q., & Shinozuka, M. (2009). "Utilization of seismic response measurement for damage detection and capacity estimation of bridge." Technical Conf. on Lifeline Earthquake Engineering Conf., ASCE, Reston, VA, 1–8.

Timoshenko, S. (1921). On the correction for shear of the differential equation for transverse vibrations of prismatic bars. *Philosophical Magazine*, 41, 744–746.

Todorovska M. I. (2009a). Seismic interferometry of a soil-structure interaction model with coupled horizontal and rocking response. *Bull. Seism. Soc. Am.*, 99(2A), 611–625.

Todorovska, M. I., & Rahmani, M. (2013). System identification of buildings by wave travel time analysis and layered shear beam models - spatial resolution and accuracy. Struct. Control Health Monit., 20(5), 686–702. DOI: 10.1002/stc.1484.

Todorovska, M. I., & Trifunac, M. D. (2008). Earthquake damage detection in the Imperial County Services Building III: Analysis of wave travel times via impulse response functions. *Soil Dynamics and Earthquake Engrg*, 28(5), 387–404. doi:10.1016/j.soildyn. 2007.07.001.

Todorovska, M. I., & Trifunac, M. D. (2008). Impulse response analysis of the Van Nuys 7-story hotel during 11 earthquakes and earthquake damage detection. *Structural Control and Health Monitoring*, 15(1), 90–116. DOI: 10.1002/stc.208.

Vossoghi, A., & Saiidi, M. S. (2010). Seismic damage states and response parameters for bridge columns. *International Concrete Abstracts Portal*, 29–46.

Zhou, Z., Wegner, L. D., & Sparling, B. F. (2007). Vibration-based detection of small-scale damage on a bridge deck. *J. Struct. Eng.*, 133(9), 1257–1126.

About the Authors

Mehran Rahmani, Ph.D., P.E.

Dr. Rahmani is an Assistant Professor in the Civil Engineering and Construction Management Department of California State University Long Beach (CSULB). He earned a Ph.D. in Structural and Earthquake Engineering from the University of Southern California (USC) in 2014, an MS in Electrical Engineering (with an emphasis in Signal Processing) from USC in 2013, and an MS in Structural Engineering from Sharif University of Technology (Iran) in 2009. Prior to joining CSULB, Dr. Rahmani, a registered Professional Engineer (P.E.) in California, worked as a Senior Engineer and Project Engineer for the structural engineering industry from 2014 to 2017. Dr. Rahmani's research focuses on structural system identification, structural health monitoring, and earthquake damage detection of buildings and bridges using sensory data. His Ph.D. research focused on developing a wave-based methodology for remote post-earthquake structural damage detection that is robust when applied to actual structures and is calibrated using data from full-scale buildings and was funded by NSF (CMMI-0800399). He has been instrumental in the advances in wave-based structural identification and monitoring in the past 15 years, receiving more than 450 citations for his technical papers.

Xintong Ji, M.S. CE

Xintong received her BS in civil engineering from California State University, Long Beach and graduated in summer 2020 with her Master's in structural engineering.

Sovann Reach Kiet, M.S. CE

Sovann graduated in spring 2021 with his Master's in structural engineering from California State University, Long Beach.